

FABRICATION AND CHARACTERIZATION OF  
THREE DIMENSIONAL PHOTONIC CRYSTALS  
GENERATED BY MULTIBEAM INTERFERENCE LITHOGRAPHY

BY

YING-CHIEH CHEN

B.S., National Tsing Hua University, 2002

DISSERTATION

Submitted in partial fulfillment of the requirements  
for the degree of Doctor of Philosophy in Materials Science and Engineering  
in the Graduate College of the  
University of Illinois at Urbana-Champaign, 2009

Urbana, Illinois

Doctoral Committee:

Associate Professor Paul V. Braun, Chair  
Professor Pierre Wiltzius, Director of Research  
Professor John A. Rogers  
Professor Paul J. A. Kenis  
Associate Professor Harley T. Johnson

## ABSTRACT

Multibeam interference lithography is investigated as a manufacturing technique for three-dimensional photonic crystal templates. In this research, optimization of the optical setup and the photoresist initiation system leads to a significant improvement of the optical quality of the crystal, as characterized by normal incidence optical spectroscopy. Theoretical spectra are calculated and demonstrate close agreement with experimental values, indicating that this fabrication process achieves excellent optical quality. X-ray microscopy provides non-destructive inspection of the fabricated crystals at nano-scale resolution. A reconstructed crystal model is generated by computed tomography which allows for comparison to a predicted structure's geometry and optical spectra. Using the polymer crystal as a template, electrodeposition is performed to completely infiltrate the crystal with  $\text{Cu}_2\text{O}$ . After polymer removal the inverted  $\text{Cu}_2\text{O}$  crystal exhibits a high peak reflectance at the predicted wavelength, indicating the structure is an exact inverse of the template. A conformal growth algorithm is developed for the commonly used chemical vapor deposition infiltration technique to explain growth results and verified experimentally with atomic layer deposition of oxide materials. Finally, a customized chemically amplified positive photoresist system and its processing steps are developed as a route to zero-shrinkage template material for high fidelity patterning of the designed interference patterns.

## ACKNOWLEDGEMENTS

First of all I would like to thank my advisors, Professor Pierre Wiltzius and Professor Paul Braun for their guidance, support and patience throughout my graduate education. I am grateful for the wonderful opportunity they have given me to initiate this exciting project. I have greatly benefited from their insight, intelligence and resourcefulness and I truly appreciate having them as my advisors.

I am thankful to Professor John Rogers for his support in the collaboration of phase mask lithography and Professor Harley Johnson for his expertise on modeling polymer deformation. I would also like to thank Professor Paul Kenis for useful comments on my project.

This dissertation would not have been possible without significant contributions and effort from many outstanding researchers from whom I learned a great deal. In particular, I would like to thank Dr. Joe Geddes and Andrew Brzezinski for their knowledge of optical simulation that allowed a thorough optical characterization. I am grateful to Dr. Jyh-Tsung Lee for his organic chemistry expertise that helped solve numerous photoresist issues. I am indebted to Dr. Leilei Yin for patiently teaching me about and performing x-ray microscopy.

I am grateful for the collaborations with Dr. Masao Miyake, Dr. Steph Rinne, Dr. Yoonho Jun, Abby Juhl, Dan Shir and Dwarak Krishnan. I also appreciate the valuable help from Dr. Florencio García-Santamaría, Dr. James Rinne, Dr. Robert Barry, Dr. Matt George, Xindi Yu, Sid Gupta, Matt Mai, Arianne Collopy as well as other Braun and Wiltzius group members.

I would like to express my gratitude to the staff at both the Center for Microanalysis of Materials in Frederick Seitz Materials Research Laboratory and the Imaging Technology Group at the Beckman Institute for their kind assistance. I would also like to acknowledge the U. S. Army Research Office, the National Science Foundation and the U. S. Department of Energy for providing the funding for this dissertation.

Lastly, I would like to thank my family for their constant love and support. I especially thank my husband, Dr. Robert Barry, for his friendship and encouragement throughout my graduate school years.



## TABLE OF CONTENTS

CHAPTER 1 INTRODUCTION .....	1
1.1 Photonic Crystals and Multibeam Interference Lithography .....	1
1.1.1 Photonic Crystals .....	1
1.1.2 Multibeam Interference .....	2
1.1.3 3D Photonic Crystals Fabricated by Multibeam Interference Lithography .....	4
1.1.4 Optical Properties .....	7
1.2 Photoresist Systems .....	9
1.2.1 Introduction to Photoresists .....	9
1.2.2 SU-8 Photoresist .....	10
1.2.3 Initiator Systems .....	13
1.2.4 Positive Photoresists .....	16
1.3 X-ray Transmission Microscopy .....	20
1.3.1 Introduction to X-ray .....	20
1.3.2 X-ray Microscopy .....	21
1.3.3 Computed Tomography .....	25
1.3.4 Xradia nanoXCT System .....	28
1.4 References .....	36
 CHAPTER 2 FABRICATION OF PHOTONIC CRYSTAL TEMPLATES WITH MULTIBEAM INTERFERENCE LITHOGRAPHY .....	 43
2.1 Introduction .....	43
2.2 Optical Setup .....	45
2.2.1 Laser .....	45
2.2.2 Optical Table and Vibration Control .....	45
2.2.3 Spatial Filter .....	46
2.2.4 Waveplates and Beamsplitters .....	46
2.2.5 Alignment Process .....	47
2.3 Photoresist Systems .....	49
2.3.1 SU-8 Photoresist .....	49
2.3.2 Photoinitiators .....	51
2.4 Fabrication Process .....	54
2.4.1 Photoresist and Substrate Preparation .....	55
2.4.2 Spin Coat .....	56
2.4.3 Soft Bake .....	57
2.4.4 Exposure .....	57
2.4.5 Post Bake .....	57
2.4.6 Development .....	58
2.4.7 Critical Point Drying .....	59
2.5 Patterning Result .....	60
2.5.1 Geometry Variation .....	60

2.5.2 Polarization and Intensity Variation .....	64
2.5.3 Polymerization Threshold Control .....	67
2.5.4 Shrinkage .....	68
2.6 Conclusions and Future Directions .....	69
2.7 References .....	70
 CHAPTER 3 OPTICAL CHARACTERIZATION .....	 71
3.1 Introduction .....	71
3.2 Optical Spectra Measurement .....	71
3.3 Model Structure Construction .....	72
3.4 Spectra Simulation .....	74
3.4.1 Finite Difference Time Domain .....	75
3.4.2 Transfer Matrix Method .....	75
3.5 Calculation Compare to Measurement .....	77
3.6 Experimental .....	78
3.7 Conclusions and Future Directions .....	79
3.8 References .....	79
 CHAPTER 4 X-RAY COMPUTED TOMOGRAPHY FOR 3D IMAGING .....	 81
4.1 Introduction .....	81
4.2 Sample Preparation .....	83
4.2.1 SU-8 Photonic Crystal Fabrication .....	83
4.2.2 Atomic Layer Deposition of Hafnium Dioxide .....	83
4.2.3 Etching Substrate .....	84
4.2.4 Pre-alignment .....	85
4.3 Phase Contrast Imaging .....	86
4.4 Absorption Contrast Imaging .....	88
4.4.1 Contrast Enhancement through Staining .....	88
4.4.2 Infiltration of $\text{HfO}_2$ by ALD .....	91
4.4.3 X-ray NanoCT Imaging .....	92
4.5 Spectra Analysis .....	96
4.5.1 Spectra Calculation with Reconstructed Crystal .....	96
4.5.2 Comparison with Uniform Shrinkage Model.....	97
4.6 Conclusions and Future Directions .....	100
4.7 References .....	101
 CHAPTER 5 INFILTRATION OF 3D HOLOGRAPHIC PHOTONIC CRYSTAL TEMPLATES .....	 103
5.1 Introduction .....	103
5.2 Conformal Surfaces Formed by Atomic Layer Deposition .....	103
5.2.1 Introduction .....	104
5.2.2 Conformal Growth Calculation .....	105

5.2.3	<i>Experimental Comparison</i>	108
5.2.4	<i>Conclusions</i>	113
5.2.5	<i>Experimental</i>	113
5.3	Complete Infiltration with Electrodeposition	115
5.3.1	<i>Introduction</i>	115
5.3.2	<i>Template Fabrication</i>	115
5.3.3	<i>Electrodeposition</i>	116
5.3.4	<i>Template Removal</i>	117
5.3.5	<i>X-ray Diffraction Characterization</i>	119
5.3.6	<i>Optical Spectroscopy</i>	120
5.3.7	<i>Conclusions</i>	121
5.3.8	<i>Experimental</i>	121
5.4	References	123
CHAPTER 6 FABRICATION WITH CHEMICALLY AMPLIFIED POSITIVE		
	PHOTORESIST	127
6.1	Introduction	127
6.2	Positive Photoresist Design	128
6.3	3D Patterning	131
6.3.1	<i>Multibeam Interference Lithography</i>	131
6.3.2	<i>Phase Mask Lithography</i>	134
6.4	Conclusions and Future Directions	138
6.5	Experimental	139
6.5.1	<i>Synthesis of tetrahydropyranyl methacrylate (THPMA)</i>	139
6.5.2	<i>Synthesis of copolymer poly(tetrahydropyranyl methacrylate)</i>	140
6.5.3	<i>Positive Photoresist Formulation</i>	140
6.5.4	<i>Two-photon Phase Mask Lithography</i>	141
6.6	References	141
CHAPTER 7 CONCLUSIONS		143
AUTHOR'S BIOGRAPHY		145

# CHAPTER 1

## INTRODUCTION

### 1.1 Photonic Crystals and Multibeam Interference Lithography

#### 1.1.1 Photonic Crystals

Photonic crystals are materials with periodic spatial variation of dielectric constants that allows the control of light within a designed frequency range. The light is modulated strongly along the periodic direction due to the reflection and refraction at the boundaries of the alternating materials. The optical properties of the crystal depend on the periodicity, geometry, dielectric constant contrast and filling fraction of the structure [1-7].

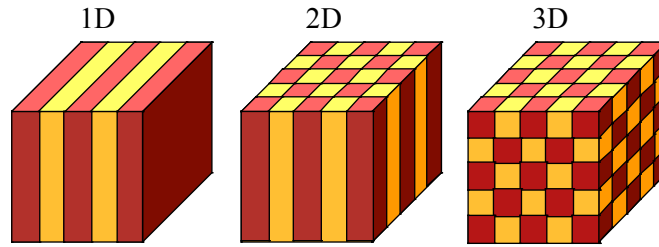


**Figure 1.1** Schematics of photonic crystals. Different colors represent different dielectric materials [1].

One dimensional thin film stacks have been used as optical gratings that selectively reflect based on frequency. Two dimensional photonic crystals have been applied commercially for improving photonic device efficiency with high confinement and low loss, examples include photonic crystal fibers and photonic crystal vertical cavity surface emitting lasers. Three dimensional photonic crystals attract considerable research interest because light can be modulated in all directions. With proper geometry and large enough refractive index contrast, a complete photonic band gap may be present where light cannot propagate in any direction. This property facilitates various applications in devices such as optical switches, sensors, filters and waveguides [2-5].

The main challenge to application of 3D photonic crystal is fabrication. The most interesting applications are in the visible wavelength range or around 1.5  $\mu\text{m}$  (current optical communication wavelength) which would require the 3D crystals to be fabricated at nanometer scales. Several fabrication routes including colloidal self-assembly [6], two-photon patterning [7], direct-write assembly [8], and interference lithography [9, 10] have been developed to replace the costly conventional layer-by-layer lithography route [11]. Among them, multi-beam interference lithography has the distinct advantage of generating large volume structures in a parallel manner as well as the ability to create different geometries with variable motifs [12-14].

### 1.1.2 Multibeam Interference

In multibeam interference lithography, crystalline periodic patterns are generated from the interference of coherent laser beams. The electric field of the laser beam can be represented as:

$$\vec{E}(\vec{r}, t) = \vec{E}^0 e^{i(\vec{k} \cdot \vec{r} - \omega t + \varphi)}$$

where  $\vec{E}^0$  is the amplitude and polarization direction,  $\vec{k}$  the wavevector,  $\omega$  the angular frequency, and  $\varphi$  the initial phase of the plane wave. The intensity distribution of  $n$  interfering beams is:

$$I(\vec{r}) = \left| \sum_{m=1}^n \vec{E}_m(\vec{r}, t) \right|^2 = \sum_{m=1}^n |\vec{E}_m^0|^2 + \sum_{m \neq l} \vec{E}_m^{0*} \cdot \vec{E}_l^0 e^{i((\vec{k}_l - \vec{k}_m) \cdot \vec{r} + \varphi_l - \varphi_m)}$$

The first term is the background intensity and the second term contains the periodic variations.

$\vec{E}_m^{0*} \cdot \vec{E}_l^0$  determines the motif of the structure, while the wave vectors establish the periodicity.

Each pair of beams generates a grating with reciprocal lattice vector  $\vec{k}_g = \vec{k}_l - \vec{k}_m$ . The periodicities generated can be calculated with illustration in Figure 1.2. The wave vectors have magnitude  $|\vec{k}_m| = |\vec{k}_l| = 2\pi/\lambda$  and  $|\vec{k}_g| = 2\pi/\delta$ . From the geometry of the vector diagram,  $|\vec{k}_g| = 2 \cdot |\vec{k}_m| \cdot \sin(\theta/2)$ , we can calculate the spacing [15]:

$$\delta = \frac{\lambda}{2\sin(\theta/2)}$$

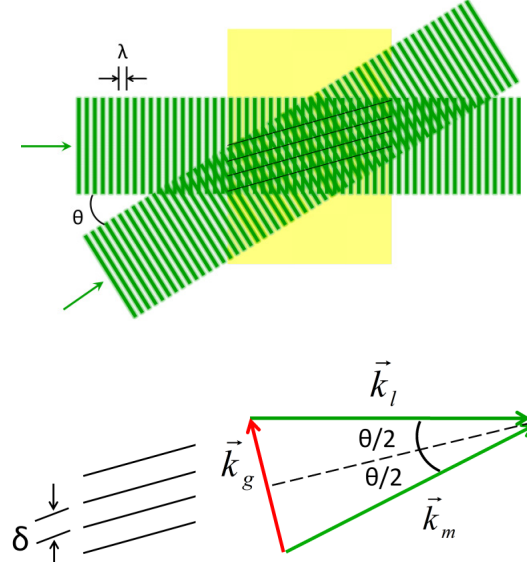


**Figure 1.2** Illustration for periodicity calculation generated from two-beam interference (schematics based on [15]).

Since each generated grating is independent, intensity distribution would result in a (n-1)-dimensional periodic structure if all the wave-vector pairs are not on a common plane. One, two, three dimensional periodicity can be generated with two, three, four beam interference respectively (Figure 1.3). Variables including wave vector, phase and amplitude can be individually controlled for each beam, giving the versatility to generate wide variety of patterns.

When more than four beams are present, the structure may not be periodic unless the phase is carefully registered between the beams at the origin. With four beams or less, the phase changes will only result in shifting the pattern position). Registering relative phase across multiple beams reproducibly at the recording media while maintaining polarization states is a challenging task [12]. As a result, most applications with multi-beam interference have been done with four or fewer beams. Phase mask lithography could be a solution for the phase problem by compensating for freedom in beam angle and polarization [10].

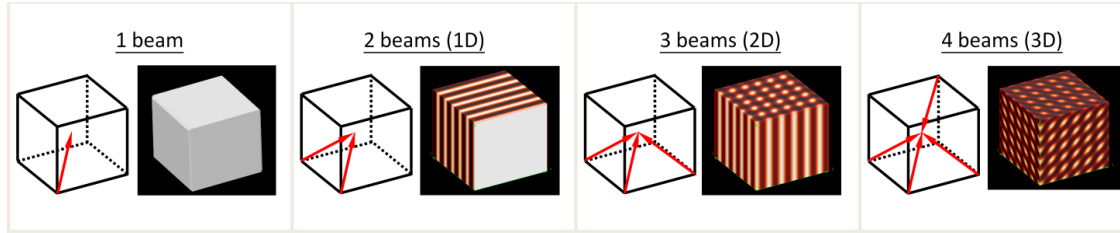


**Figure 1.3** Periodic patterns generated from multi-beam interference (Image courtesy of James Rinne).

### 1.1.3 3D Photonic Crystals Fabricated by Multibeam Interference Lithography

Generation of 3D periodic patterns with four-beam interference was first reported in 1995 by Mei et al. [16]. Three dimensional optical lattices were imaged using an optical microscope and application for photonic crystal fabrication was suggested. Berger et al. used photoresist to record 2D triangular patterns generated from three 1D diffraction gratings. Two dimensional GaAs photonic crystals were created and using photoresist for 3D photonic crystal templates was proposed [17]. The first 3D crystal created with four-beam interference was reported by Cambell et al. in 2000 with an umbrella beam geometry [9]. Sub-micron intensity distribution of a face-centered-cubic-like pattern was generated with pulses of 355 nm light and successfully recorded into SU-8 photoresist. Around the same time Shoji and Kawata reported fabrication of 3D photonic crystal using an urethane acrylate system at 442 nm by a two-step (2-beam + 3-beam) exposure process [18]. Since then research activity has taken off both in theoretical prediction and experimental demonstration.

The multi-beam interference lithography process for photonic crystal applications involves beam parameter design, optical setup, crystal template fabrication from the interference patterns, and possible inversion to functional materials (Figure 1.4). The following paragraphs briefly describe each aspect.

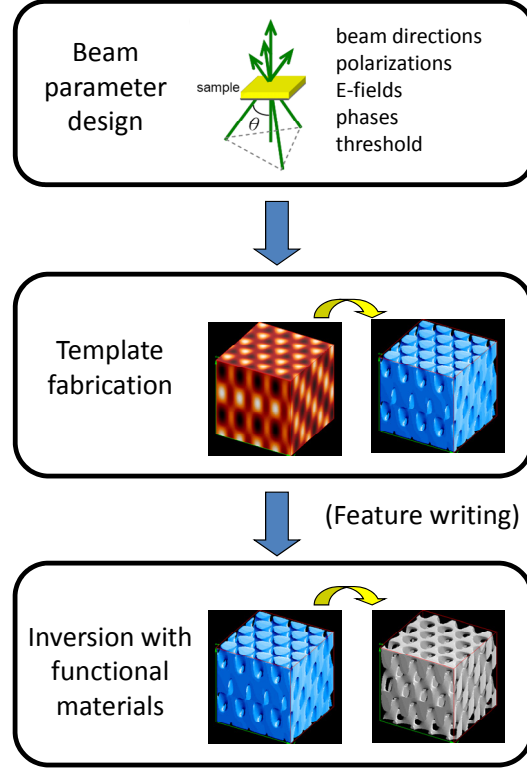


**Figure 1.4** Primary steps of 3D photonic crystal templated by multi-beam interference lithography.

#### 1.1.3.1 Beam Parameter Design

Typical strategies for designing beam parameters start with matching the difference of wave vectors to the basis vector of the reciprocal lattice for a pre-determined crystal structure based on their translational symmetries [19-21]. There may be different sets of wave vectors that can generate the same lattice, but the lattice parameters will vary with their beam angles. It was reported that all fourteen Bravais lattices can potentially be formed by interference of four non-coplanar beams [22]. The motifs, determined by the relative polarizations, can be further considered with a level-set approach in order to match the designated space group [23]. Various groups have used the symmetry approach to design beam parameters for optically interesting geometries such as of diamond, simple cubic and bcc-gyroid [24-27]. The symmetry constraint can be lifted by using a genetic algorithm technique which has potential to finding better beam



parameters for target optical properties [28]. Recently a wave guiding design has also been reported for holographically generated diamond-like structures [29].

#### *1.1.3.2 Template Fabrication*

After the first report of 3D holographic photonic crystal in 2000 [9], fabrication systems have been demonstrated with a variety of laser wavelengths, geometries and recording materials. While the original four-beam system used pulses from a Q-switched laser at 355 nm, patterning with a continuous wave laser at 514 nm was also reported using a customized SU-8 photoresist system [30, 31]. This greatly simplifies alignment steps in the system as the beam paths are visible. Additionally, base can be added to the photoresist system in order to neutralize the background intensity for better resist contrast [15]. Other successfully patterned wavelengths include 351nm, 488nm, and 532nm [32-34].

Although many structures are designed for holographic lithography, complications in fabrication have only allowed a handful of symmetries to be experimentally demonstrated [35-38]. These structures include various rhombohedra (FCC, BCC, simple cubic as special cases), woodpile and spiral. The most commonly used beam geometry has been the first proposed four-beam umbrella geometry because the beams come from the same half space, providing relatively easy set up and the potential of using non-transparent substrate (anti-reflection coating may be needed). This beam geometry has also been used to investigate and improve the fabrication process as well as testing new photoresist materials.

The most common recording material in this work is SU-8 negative tone photoresist. Its high sensitivity, resolution, and mechanical stability allow it to resolve patterns in 3D [39]. Organic-inorganic hybrid photoresists have been developed and demonstrated for multi-beam interference patterning for better thermal properties [40-42]. The purpose is to withstand high temperature processing for infiltration, particularly for deposition of high refractive index materials. Other hybrid photosensitive systems that have been used with two photon patterning

may also be applicable for the same purpose [42, 43]. Positive DNQ photoresist was used to generate a template for low shrinkage and easy removal [44]. Negative photoresists which have much lower shrinkage compared to SU-8 have been reported as well [45]. Most photosensitive materials are patterned as a template for functional material inversion, but in some cases the material itself may have the desired functionality. These include a thermally responsive hydrogel photoresist system [46], and an electrically tunable holographic dispersed liquid crystal systems [47]. For photonic band gap applications, chalcogenide glass is both photosensitive and high index so may be patterned directly in 3D [48].

#### *1.1.3.3 Template Inversion*

Holographically defined polymer photonic crystals can serve as templates for subsequent deposition of high refractive index materials for applications requiring a pseudo- or a complete photonic band gap. Chemical vapor deposition (CVD) and atomic layer deposition (ALD) have been used for infiltration of Si [32, 49] and  $\text{TiO}_2$  [50] respectively. Electrodeposition has also been used to deposit  $\text{TiO}_2$  [51] and  $\text{Cu}_2\text{O}$  [52]. Double inversion of templates for GaAs photonic crystal generation is an ongoing project in the Braun group. To incorporate functionality using the band gap, controlled defects can be placed into the crystals via multiphoton polymerization, either by patterning the same photoresist before hologram development, or by infiltrating the developed structure with other recordable media [32, 53].

#### *1.1.4 Optical Properties*

Light entering a photonic crystal either refracts through or reflects back at each interfaces and the waves are constructive or destructive according to the wavelength, refractive index and dimension and geometry of the two mediums [54]. The quality of fabricated 3D photonic crystals is usually characterized with normal incidence optical spectroscopy. A peak in reflectance and a

dip in transmittance can usually be observed at the appropriate frequency range, as Figure 1.5 shows.

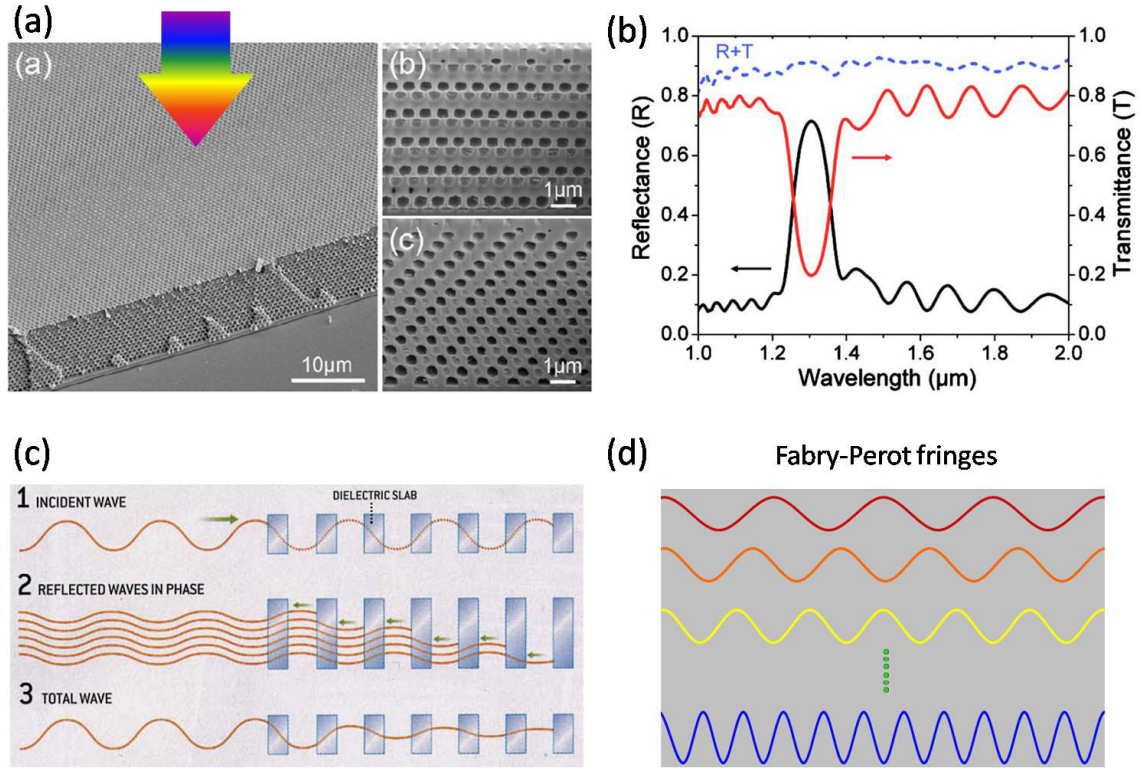


**Figure 1.5** (a) SEM picture of a holographic SU-8 photonic crystal been characterized using normal incidence optical spectroscopy [34] (b) Reflectance and transmittance spectra of the 3D photonic crystal [34] (c) Main reflectance peak comes from reflective waves being in phase due to the sub-micron structures [54] (d) Background oscillation of the spectra comes from reflections across the thickness of the entire film. The thick film can accommodate several different constructive reflections at the interested wavelength range causing the fringes.

Despite the supposedly large-area, defect-free nature of previously reported holographically defined crystals, many reported reflectivity peaks are only about 30%. Self-assembled colloidal crystals of comparable thickness typically have much higher reflectivity. The exact reasons for this are still to be determined. The limited optical response of these polymer templates would carry on through subsequent processing steps and ultimately limit the performance of the optical components derived from them. Recently high quality photonic

crystal templates generated from interference lithography have been reported using the SU-8 photoresist system [34, 55]. The high refractive index materials inverted from these high quality templates exhibit excellent optical properties [52, 55].

## **1.2 Photoresist Systems**

### *1.2.1 Introduction to Photoresists*

Photoresists are materials which can be patterned by selective exposure to light. The light initiates a reaction which changes the solubility of the photoresist allowing either the exposed or unexposed regions to be dissolved by a developer. When used in semiconductor lithography process, they are patterned and used to block access of an etchant to its substrate, hence the name “resist”. Photoresist can be separated into positive and negative tone, as shown in Figure 1.6. Negative photoresists are typically composed of crosslinkable monomer or polymer. The region that is exposed to light is designed to crosslink and resist the solvent, while the uncrosslinked area dissolves during development. Positive photoresist patterning is based on solubility changes due to light irradiation. The exposed area changes from insoluble to soluble to the developer and can be washed away, while the unexposed regions remain.

For negative photoresist, the polymerization can be based on free radical or cationic reactions. In multi-beam interference lithography, cationic polymerization is favored over free radical polymerization because there is minimal polymerization before introducing heat. This means that exposure and crosslinking are de-coupled, so the interference pattern will not be distorted from changes in the refractive index during exposure. In the case of free radical initiation, the polymerization reaction occurs during exposure and the interference pattern may be distorted by the resulting refractive index shifts.

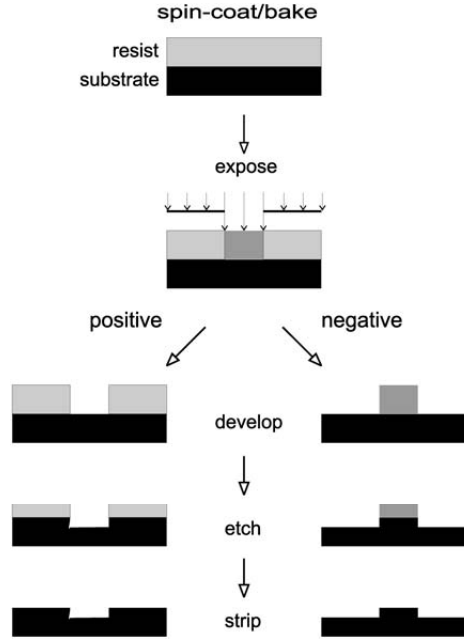


**Figure 1.6** Positive and negative photoresist lithography patterning process [56].

### 1.2.2 SU-8 Photoresist

The most commonly-used template material for holographic photonic crystals is SU-8 epoxy based negative photoresist. Because of its unique properties, it is widely employed in micro-electrical mechanical systems (MEMS) [39, 57]. The SU-8 monomer (Figure 1.6) has low molecular weight so it dissolves easily in solvents, which is helpful for creating highly concentrated and viscous solutions. This enables the formation of thick films by spin coating and improved resolution at the development step. It also has high functionality (8 epoxy groups per monomer), rendering a high degree of crosslink density when polymerized and providing resilient thermal, mechanical and chemical properties. The physical properties of the photoresist are listed in Table 1.1. When adding a proper photoacid generator to SU-8, during light exposure, a low concentration of acid is generated and with subsequent heating, a crosslinking reaction is activated. Thermal initiation can occur in the system when baking temperature is high ( $T > 137^\circ$ ). SU-8 has also been used with e-beam lithography and x-ray lithography [39].

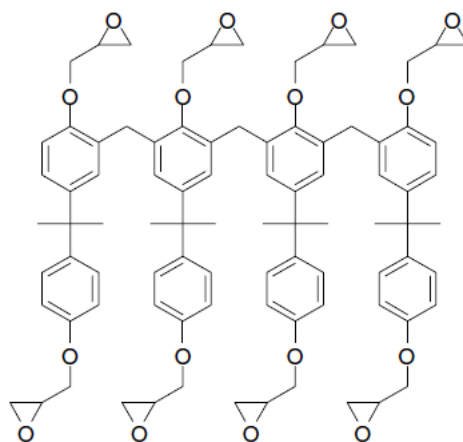


**Figure 1.6** Chemical structure of the Bisphenol A Novolak epoxy oligomer containing in SU-8 formulations. Eight epoxy functionalities allow a high degree of cross-linking after photoactivation [39].

Property	Value
Young's modulus, $E$ (post-bake at 95 °C)	4.02 GPa
Young's modulus, $E$ (hard bake at 200 °C)	$4.95 \pm 0.42$ GPa
Biaxial modulus of elasticity, $E/(1 - \nu)$	$5.18 \pm 0.89$ GPa
Film stress (post-bake at 95 °C)	16–19 MPa
Maximum stress (hard bake at 200 °C)	34 MPa
Friction coefficient (post bake at 95 °C)	0.19
Glass temperature, $T_g$ (unexposed)	$\sim 50$ °C
Glass temperature, $T_g$ (fully cross-linked)	$> 200$ °C
Degradation temperature (fully cross-linked)	$\sim 380$ °C
Thermal expansion coefficient (post-bake at 95 °C)	$52 \pm 5.1$ ppm $K^{-1}$
Polymer shrinkage upon cross-linking	7.5%

**Table 1.1** Physical properties of the SU-8 photoresist [39].

SU-8 can be polymerized with cationic initiation by an acid catalyst. The process is sensitive to moisture and base concentrations, which will cause chain transfer or chain termination reactions (Figure 1.7).

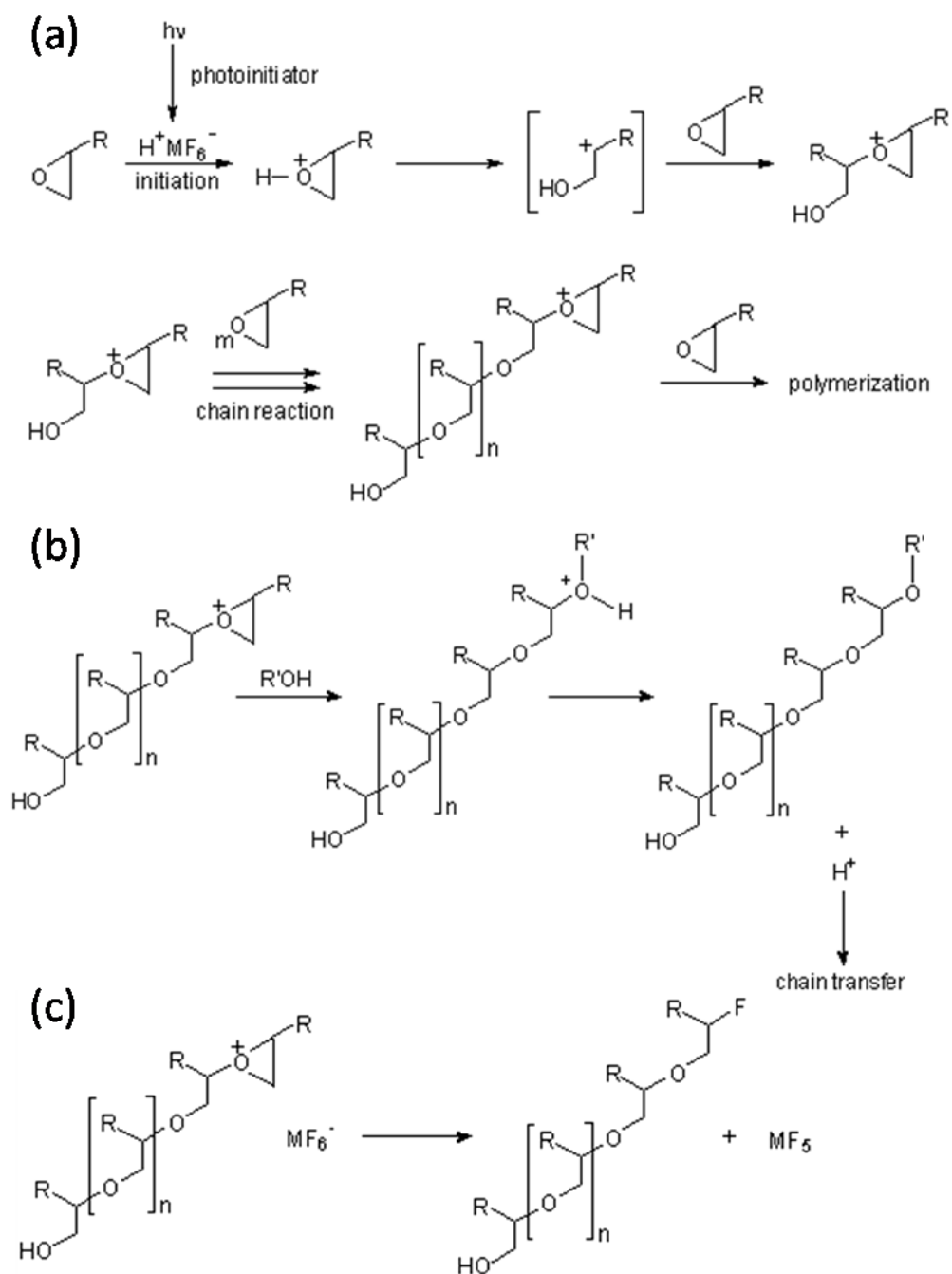


**Figure 1.7** (a) Epoxide ring opening polymerization process (b) Chain transfer reaction of epoxy polymerization (c) Chain termination reaction [58]

### 1.2.3 Initiator Systems

Several different types of initiator systems have been developed for cationic polymerizations [59]. Below describes two types of initiator systems that have been used in SU-8.

#### 1.2.3.1 Onium Salt Photoacid Generator

Onium salts are the most common cationic photoinitiators due to being both efficient and stable [60]. The salts contain cations with heteroatom centers and non-nucleophilic anions. The functions of the cation and anion are outlined in Figure 1.8. The light-absorbing cation determines the photochemistry, which includes absorption spectrum, photosensitivity and thermal stability. The anion controls the kinetics of the reaction by determining the strength of the acid formed during photolysis. Triarylsulfonium and diaryliodonium salts are among the most widely used. Specifically, a mixture of sulfonium salts shown in Figure 1.9 have been used in many commercial applications, coupled with SU-8 photoresist due to its excellent sensitivity, thermal stability and long UV absorption band. Diaryliodonium has an advantage in that it can be easily sensitized to operate at visible wavelength with proper photosensitizers [60].

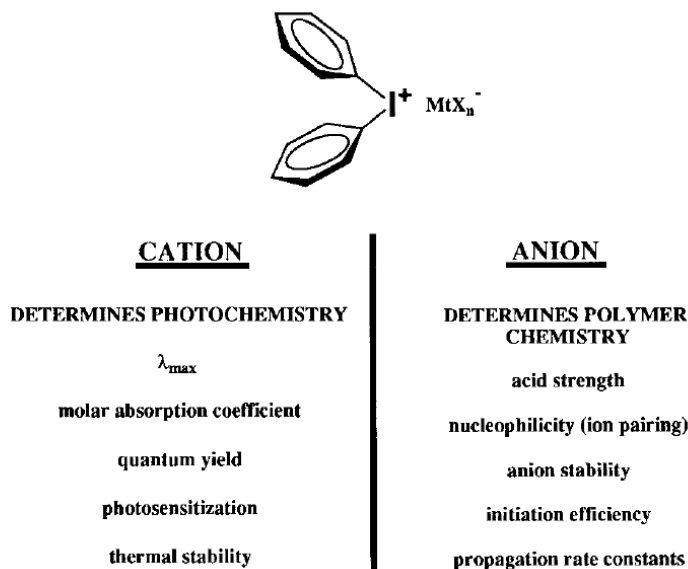


**Figure 1.8** Anatomy of an onium salt photoinitiator [60].



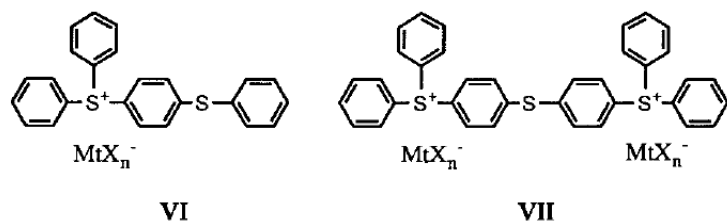


**Figure 1.9** Sulfonium salt mixture [60].

Xanthene dyes are known to be outstanding photosensitizers. Examples of the dyes can be seen in reference [61] and shown in Figure 1.10. The mechanism involves a photoinduced electron transfer from an excited photosensitizer to diaryliodonium salt via an exciplex; with consequent reduction of the diaryliodonium salt (Figure 1.11) [58]. The decomposition of the diaryliodonine free radical prevents back electron transfer from occurring. In some cases addition of co-initiators improves the efficiency of photoacid generation [61].

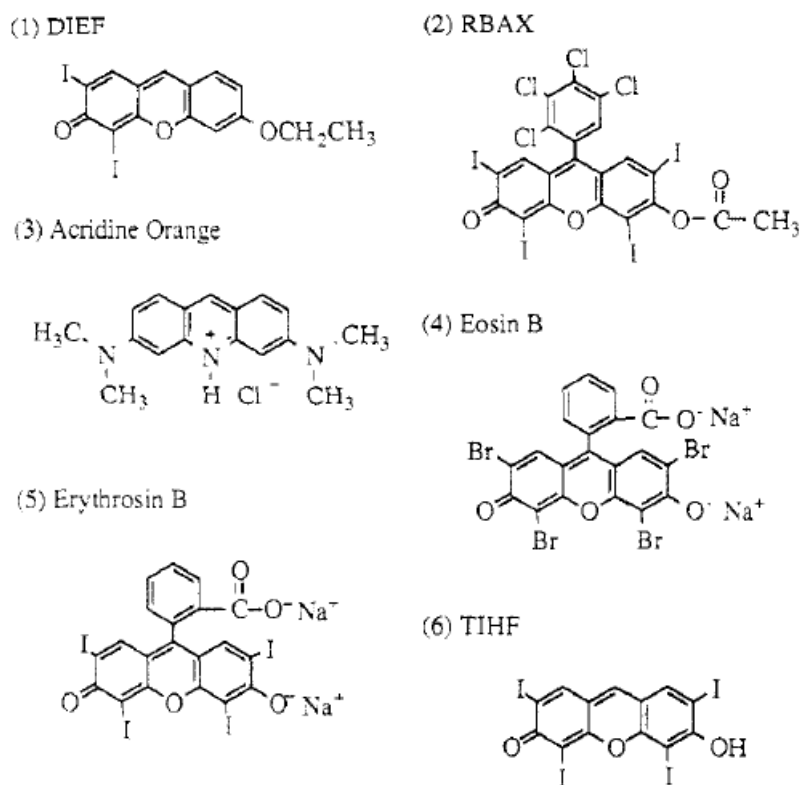


**Figure 1.10** Structures of different photosensitizers [61].

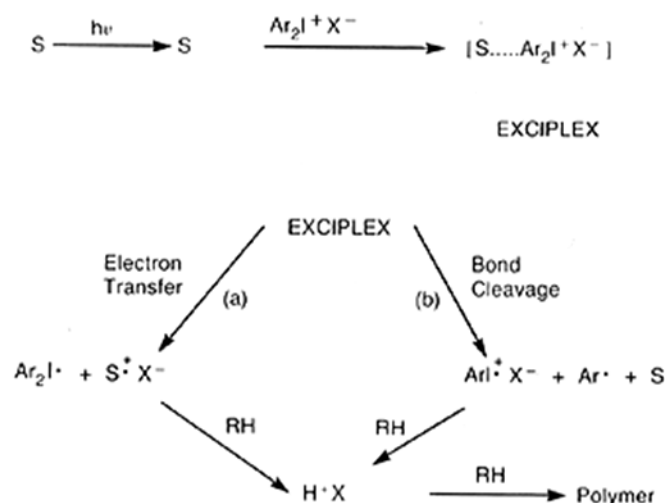


**Figure 1.11** Mechanism of photosensitization [58].

### 1.2.3.2 Iron Arene Complexes

Iron arene complexes are a different class of photoinitiator than onium salts. They can serve as either cationic or free radical photoinitiators [62]. However as a cationic initiator it can only be used for ring-opening polymerizations such as for epoxies [59]. Figure 1.13 shows examples of iron arene complexes. Upon irradiation, the salt undergoes photolysis and generates an iron-based Lewis-acid with the loss of the arene ligand. Coordination of this later species with an epoxy monomer is followed by ring opening polymerization. The mechanism is shown in Figure 1.13. Oxygen was found to promote the efficiency of iron-arene complexes, due to the oxidation of iron (II) to iron (III) species [62]. Depending on the environment, the iron-arene complex initiator can have a wide spectrum range from UV into the visible [63].

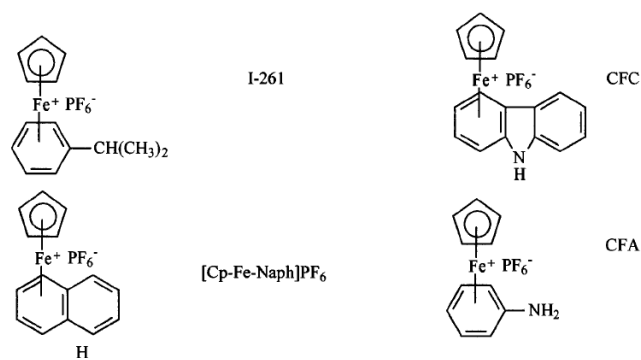


**Figure 1.12** Examples of iron-arene salts [64].

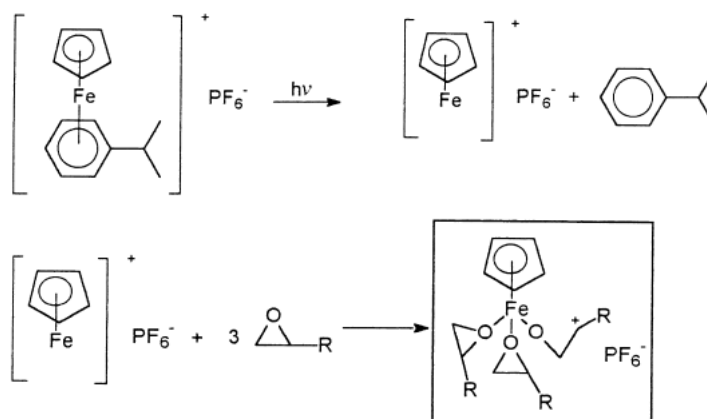


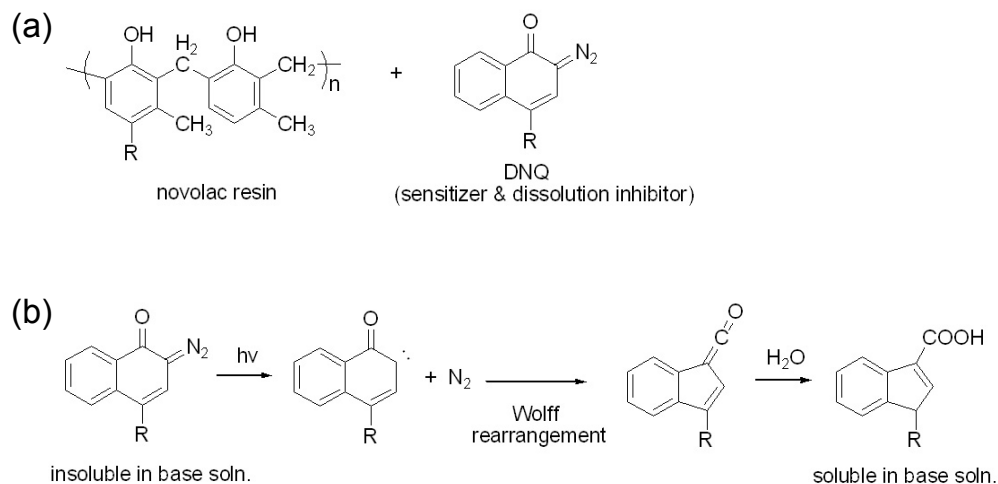
**Figure 1.13** Process of ring opening polymerization initiated by iron-arene complex [59].

#### 1.2.4 Positive Photoresists

Negative resist based on crosslinking can suffer from image distortion due to swelling in the developer. Positive photoresist, which is often based on a polarity change mechanism, is less prone to distortion. It also does not experience the intrinsic shrinkage from the crosslinking reaction. This makes the application of positive resist system to holographic photonic crystal fabrication especially interesting since the crystal's optical properties are strongly dependent on the crystal geometry.

##### 1.2.4.1 DNQ Based System

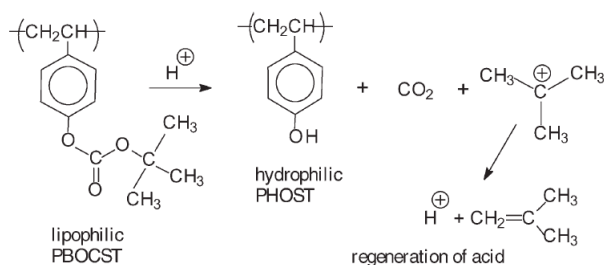
A typical commercialized broadband positive photoresist system consists of phenolic-based Novolac resin and diazonaphthoquinone (DNQ) derivatives as photosensitizer and dissolution inhibitor against base developer (Figure 1.14 (a)). When exposed to light, DNQ undergoes Wolff rearrangement and becomes soluble in base solutions (Figure 1.14 (b)). Since Novolac is also highly soluble in base solutions, photopatterning can be achieved. However, it is observed that thick film patterning of this type of resist is difficult due to considerable absorption of light by DNQ. The sensitivity of DNQ is also relatively low, so long exposure time is needed which makes the patterning process sensitive to vibration [44].



**Figure 1.14** Commercialized DNQ + novolac positive photoresist (a) composition (b) photochemical mechanism [44].

#### 1.2.4.2 Chemically Amplified System

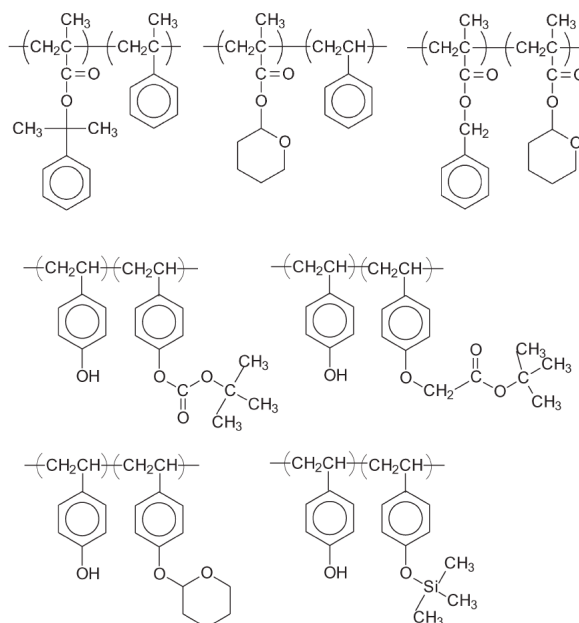
The most common mechanism of chemically amplified positive photoresist is acid-catalyzed cleavage of pendant protecting groups to generate base-soluble acidic functionalities such as phenol and carboxylic acid [56]. The first photoresist developed with this mechanism, t-BOC, is shown in Figure 1.15.



**Figure 1.15** Acid-catalyzed deprotection from polarity change (tBOC resist) [56].

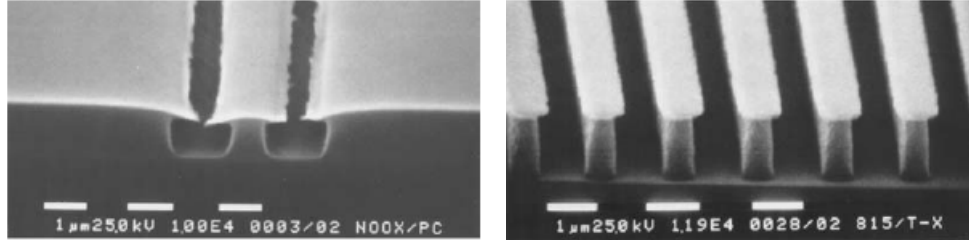
The deep-UV photoresists adopted in the industry are based on copolymer design. This provides much more flexibility because one component does not need to have all the functionality, and the overall functionality is tunable based on the monomer type and ratio used. Design considerations include hydrophobicity, thermal stability, absorption property and compatibility with other components, such as the photoinitiator. Examples of the copolymers are shown in

Figure 1.16. Usually the protecting group is between 20% and 30% concentration because the by-product may evaporate during postbaking and cause shrinkage.



**Figure 1.16** Methacrylate copolymers and hydroxystyrene copolymers for acid-catalyst deprotection [56].

Compared to the DNQ system, chemically amplified positive photoresist is much more responsive for photopatterning with a lower absorption. However the acid-catalyzed reaction is very sensitive to airborne base contamination. A typical artifact observed in lithography is a skin or T-top formation, as shown in Figure 1.17, which is a surface insoluble layer due to acid neutralization by base contamination. The neutralization happens during and after exposure, and the skin effect is especially serious when the sample is not baked right away. The skin formation is sometimes called a post exposure delay (PED) effect. This effect also occurs in the SU-8 system, a negative chemically amplified resist, but since the resist is negative tone the top layer can be dissolved away instead and not affecting the development process as much.



**Figure 1.17** Skin and T-top profiles formation due to air contamination [56].

The contamination problem can be solved by filtering the air with activated carbon. Figure 1.18 shows the effect with and without air filtration. Only 10 ppb (parts per billion) of NMP for 1 minute is needed to cause a skin effect [56]. Other methods to overcome the skin effects include using a protective overcoat, adding a small amount of base additive as quencher, or tuning the polymer so that the activation energy is low (so no post bake required) and annealing to reduce free volume [56]. Photobase is a particularly interesting additive in that the overall contrast can be enhanced. Upon radiation the photobase is neutralized while the photoacid is generated, and the dark area remains basic, thus contrast is enhanced [56].

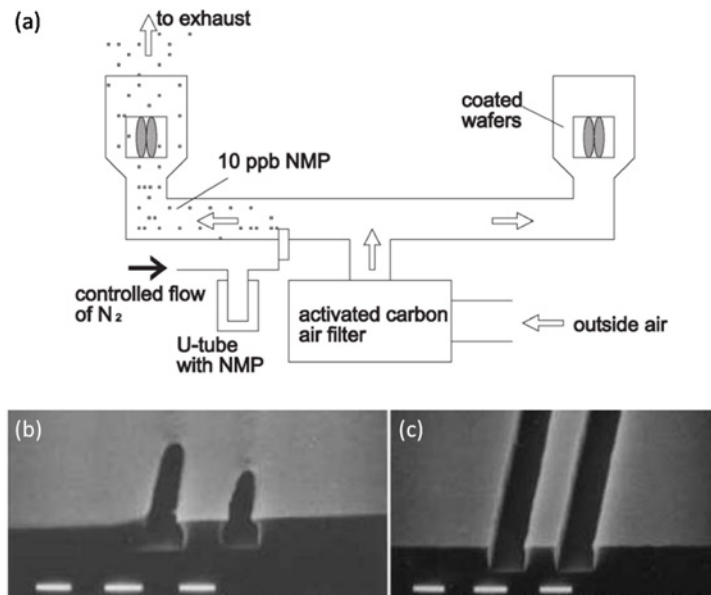


**Figure 1.18** Activated carbon filtration (a) setup (b) without filtration (c) with filtration [56].

### 1.3 X-ray Transmission Microscopy

#### 1.3.1 Introduction to X-ray

In the electromagnetic spectrum, x-ray wavelengths range from  $10^{-2}$  to 10 nanometers (Figure 1.19). They can be generated either by electrons changing energy level within an atom or by accelerated free electrons, as illustrated and explained in Figure 1.20. In medicine, x-ray wavelengths have long been used for imaging because its high energy can transmit through bodies of living creatures and resolve imbedded features such as bone fractures and tumors. In materials science, the typical application for x-ray is using its diffraction to study atomic arrangement of material structures at the angstrom level. However x-rays have also become an important imaging tool due to recent improvement in x-ray optics that led to advances in x-ray microscopy.

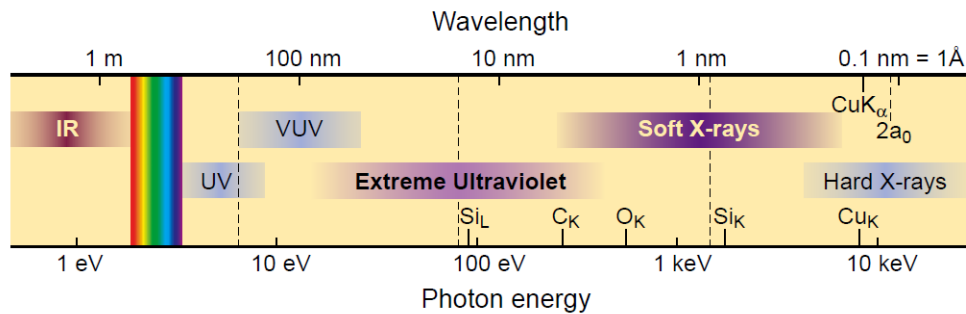


**Figure 1.19** Electromagnetic spectrum from infrared to x-ray [65].

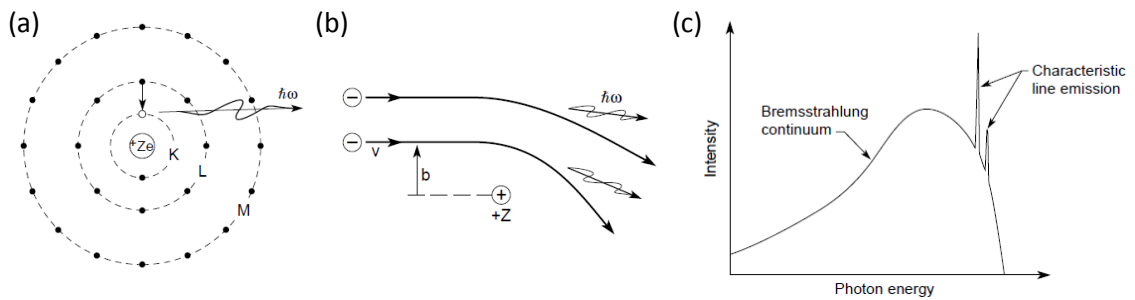


**Figure 1.20** (a) Characteristic x-ray radiation from fluorescence emission of an atom, (b) Bremsstrahlung radiation when incident electron is accelerated by passing through a nuclei, (c) continuum radiation and narrow line emission from a solid target with incident electrons that can be observed from the anode of an x-ray tube [65].

### *1.3.2 X-ray Microscopy*

Visible light optical microscopy and electron microscopy are most commonly used for direct imaging of structures. However to non-destructively image optically opaque samples or those that are too thick for electrons to penetrate, these two techniques are not applicable. X-ray microscopy complements the two techniques in that it has better resolution compared to visible light due to its short wavelength, and better penetrating power than electrons since they do not interact with matter as strongly as a charged particle [66]. Unlike electron microscopy, metal coating and vacuum compatibility are not required. This is especially advantageous for soft or biological samples because they can be imaged at their natural state. X-ray microscopy is also ideal for defect analysis on irreplaceable samples which cannot be modified [67].

#### *1.3.2.1 Soft X-ray and Hard X-ray Microscopy*

Soft x-ray ( $< 3\text{-}5\text{ keV}$ ) is particularly suitable for biological microscopy. Biological specimens are usually thick and embedded in water. In the water window, between K shell absorption edges of oxygen (543 eV, 2.3 nm) and carbon (284 eV, 4.4 nm), nitrogen and carbon have inherent absorption contrast against water which has a much longer absorption distance at those wavelength values. This can be very useful for imaging various biological materials such as proteins in water/ice (Figure 1.21 water window). With optical microscopy, the contrast needs to rely on dyes and for electron microscopy on heavy metal stains. To date, zone plate based soft x-ray microscopy has a spatial resolution better than 15 nm [68].

#### *1.3.2.2 Types of X-ray Microscopy*

Figure 1.22 shows four types of microscopy techniques: projection, magnified projection, lens imaging, and scanning microscopy. The simple projection technique uses a synchrotron source. X-ray optics is required and the resolution is limited by the detector. The magnified projection design focuses the incoming synchrotron radiation with x-ray optics such as Kirkpatrick-Baez mirrors [69], Fresnel zone plates [70, 71], or parabolic refractive x-ray lens [72], which can relax the resolution requirement for the detector. Lens imaging technique resembles



optical microscopy. With the highly quality focusing lens--either a Fresnel zone plate or a parabolic refractive lens, the source requirement can be relaxed to non-synchrotron source. In scanning microscopy high quality optics focus synchrotron radiation to a line that is less than one micron wide and up to a millimeter deep. The beam scans the sample and signals such as diffraction, small-angle scattering, fluorescence and absorption are measured for each beam position. When incorporated with tomography, the rich information of the 3D structure can be constructed.

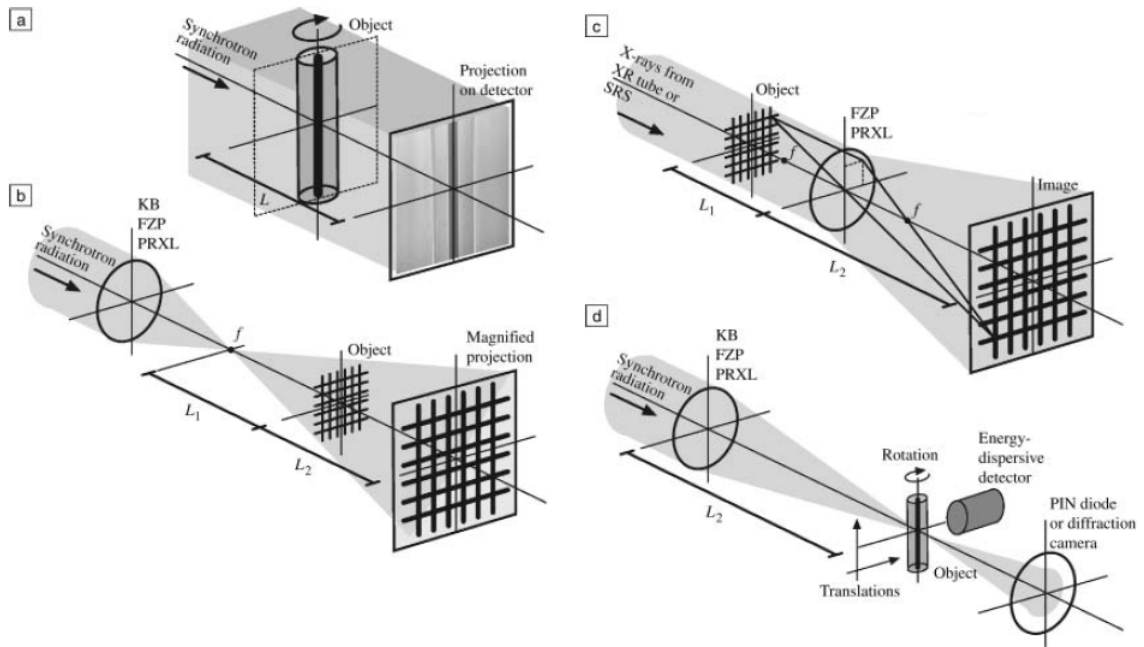


**Figure 1.22** Schematic illustration of different types of microscopy techniques. (a) Projection imaging, (b) magnified projection imaging, (c) full field microscopy, (d) scanning microscopy [73].

### 1.3.2.3 Absorption Contrast and Phase Contrast

\*Summarized from reference [74]

Similar to optical microscopy, the image contrast in x-ray microscopy comes from variation in absorption or phase. In absorption contrast mode, the contrast comes from the

variation in optical density,  $D(x, y)$ . Assuming x-rays are traveling straight through the material along the z-axis, the optical density can be expressed by

$$D(x, y) = -\ln T(x, y) = \int \mu(x, y, z) dz$$

where  $T(x, y)$  is transmission and  $\mu(x, y, z)$  is the absorption coefficient. From the atomic point of view, the absorption coefficient  $\mu(x, y, z)$  is related to atomic density  $N_k(x, y, z)$  and absorption cross-section  $\mu_k^a$ .

$$\mu(x, y, z) = \sum_k N_k(x, y, z) \mu_k^a dz$$

Absorption cross-section is determined by the classical electron radius ( $r_0$ ), x-ray wavelength ( $\lambda$ ), and the imaginary part of the atomic scattering factor ( $f = f_1 + i f_2$ ). ( $f$  measures scattering amplitude of a wave by an isolated atom.)

$$\mu_k^a = 2r_0\lambda f_2$$

In phase contrast mode, the contrast comes from the variation in phase shift,  $\Phi(x, y)$ .

$$\Phi(x, y) = \frac{2\pi}{\lambda} \int \delta(x, y, z) dz$$

where  $\delta(x, y, z)$  is the refractive index decrement from unity x-ray penetrating the material.

From the atomic point of view, it is related to the atomic density, atomic number  $Z$ , and the real part of the anomalous dispersion correction of element  $k$ ,  $f_k$ , and classical electron radius,  $r_e$ .

$$\delta(x, y, z) = \frac{r_e \lambda^2}{2\pi} \sum_k N_k(x, y, z) (Z_k + f'_k)$$

Optical density and phase shift can be written as

$$D(x, y) = \int \sum_k N_k(x, y, z) \mu_k^a dz$$

$$\Phi(x, y) = \int \sum_k N_k(x, y, z) p_k dz$$

where  $p_k = r_e \lambda (Z_k + f'_k)$  is the x-ray phase shift cross-section.

Thus, to judge the sensitivity of phase contrast and absorption contrast for the same material, the absorption and phase shift cross-section should be compared. Figure 1.23 plots the two values versus the atomic number. The figure shows that the phase shift cross section is always larger than the absorption cross section for a range of energies. When atomic number is low, the difference can be three orders of magnitude.

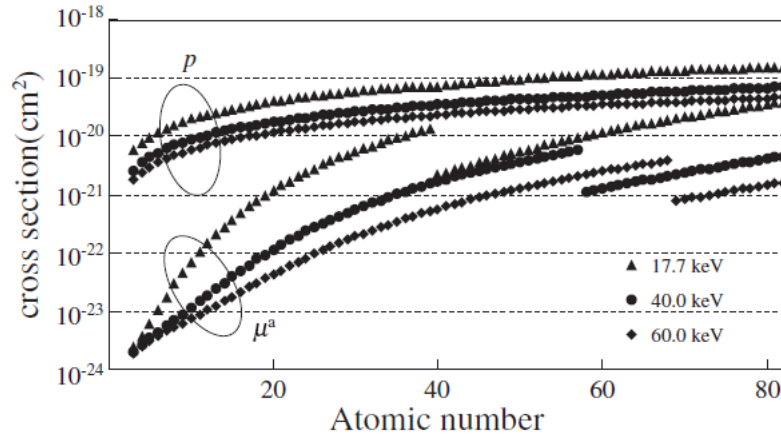


**Figure 1.23** Interaction cross sections of absorption ( $\mu^a$ ) and phase shift ( $p$ ) versus atomic number [74].

From the macroscopic point of view, the interaction of x-rays with matters can be described by the index of refraction.

$$n = 1 - \delta + i\beta$$

where the dispersive decrement  $\delta$  is on the order of  $10^{-6}$ , a small quantity. The imaginary part of the refractive index is related to the linear absorption coefficient  $\mu$  with

$$\beta = \frac{\lambda}{4\pi} \mu$$

Absorption and phase contrast can be described by  $\beta/\rho$  and  $\delta/\rho$ , where  $\rho$  is the material density.

Absorption is approximately proportional to  $(Z/E)^3$ , where  $Z$  is the atomic number and  $E$  is photon energy; and phase contrast is almost independent of  $Z$ . So for low  $Z$  materials with high  $E$ , phase contrast is much more favorable than absorption contrast [73].

Phase imaging requires a coherent light source, i.e. light source with defined phase. The temporal coherence  $l_t$  is determined by the spectral width  $l_t \sim \lambda^2 / \Delta\lambda$ . It can be enlarged by monochromatizing. In the case of hard x-rays, a double-crystal silicon monochromator is used on a synchrotron x-ray beam. The spatial coherence  $l_s$  is related to the intensity distribution of the x-ray source.  $l_s \sim \lambda / (2\pi\Delta\theta)$ , where  $\Delta\theta$  is the angular size of an x-ray source. The smaller source would contribute to higher spatial coherency. Coherence filters such as a narrow aperture and a crystal collimator can be used but suffer a decrease in x-ray density [74].

Unlike absorption contrast, a single phase contrast projection image does not directly correspond to a quantitative physical property such as density, and its resolution is limited to the fringe width. Holotomography has been developed to obtain more quantitative measurements by phase imaging [75]. It involves taking measurements (typically three to four) at varying distances from the sample. Through phase mapping and 3D reconstruction, the electron density of the object can be realized.

X-ray and materials interaction including refractive index, transmission, reflection, etc. can be calculated with an excellent reference website: [http://henke.lbl.gov/optical\\_constants/](http://henke.lbl.gov/optical_constants/)

### 1.3.3 Computed Tomography

\* Summarized from reference [76]

Tomography is imaging of objects by cross-sections from data collected by illuminating from many different directions. The projection at a specific angle is the integral of the image in the specified direction (Figure 1.24). The mathematical method is developed by Rodon in 1917, and the first medical application with x-ray CT was invented by Hounsfield, who won the 1979 Nobel Prize in medicine (together with Allan Cormack, who independently developed a CT algorithm). For medical applications computed tomography has since been extended to other imaging techniques including radioisotopes, ultrasound and magnetic resonance.

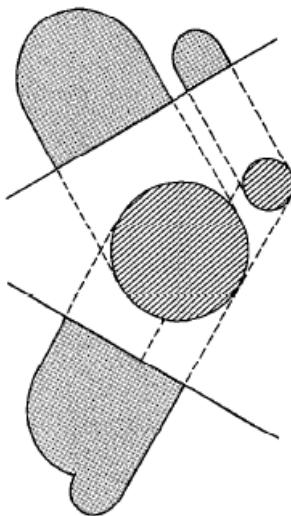


**Figure 1.24** Two projection of the combination of two cylinders [76].

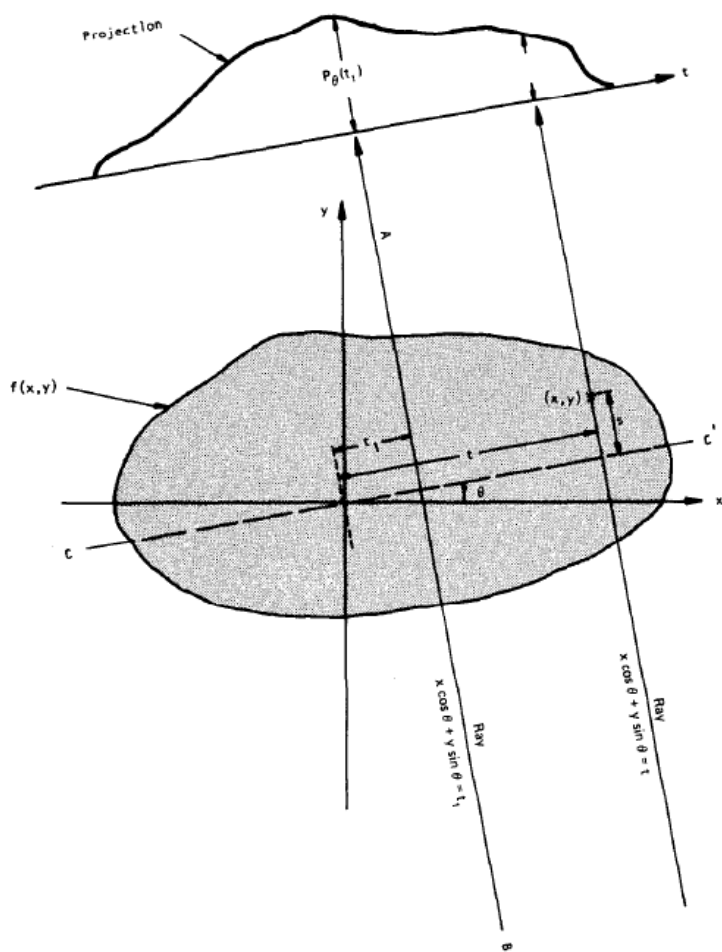


**Figure 1.25** An object,  $f(x, y)$ , and its projection,  $P_\theta(t_1)$ , are shown for an angle of  $\theta$  [76].

Each measurement of projected data can be presented as a series of line integrals (Figure 1.25). One dimensional Fourier transform was applied to the projection. With all the projection data Fourier-transformed, it is possible to estimate the object with a 2-dimensional inverse Fourier transform (Fourier Slice Theorem). The filtered back projection algorithm is applied for reconstruction, assuming x-ray projection is parallel.

The reconstruction quality depends on the quality of each projection data, number of the projections, the angle range across which projections are taken, and the monochromaticity of the x-ray. Artifacts can present in the reconstruction data depending on the condition of the imaging. Figure 1.26 and Figure 1.27 illustrate two types of typical reconstruction artifacts.

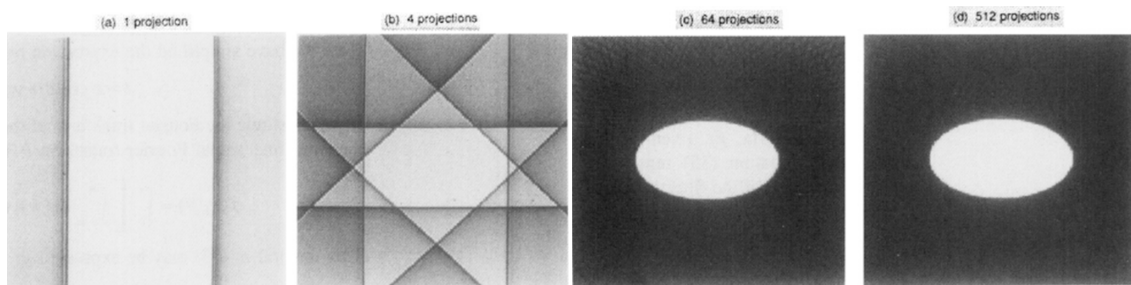


**Figure 1.26** The reconstruction result of an ellipse from different numbers of projections [76].

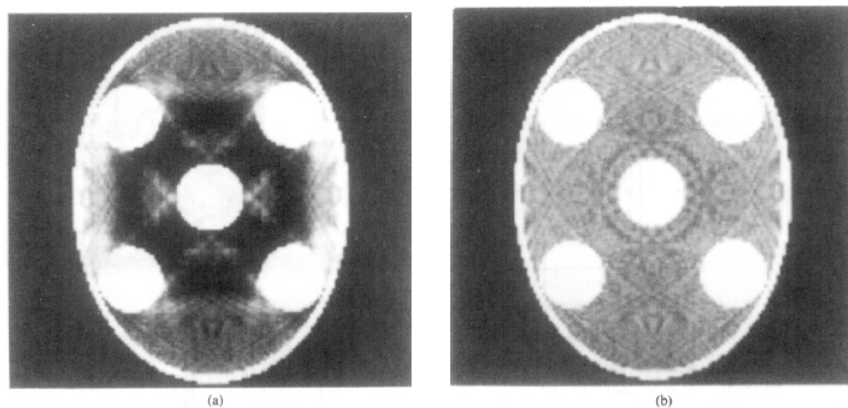


**Figure 1.27** Reconstructed images of a phantom that has a skull with five circular pieces of bone and water inside. (a) Reconstruction from polychromatic x-rays projections. The wide dark streaks are caused by the polychromaticity of the x-rays. (b) Reconstruction image with monochromatic x-ray projections [76].

#### 1.3.4 Xradia nanoXCT System

The tomographic x-ray microscopy system used in this research is a nanoXCT from Xradia Inc. The main components of the microscope are shown in Figure 1.28, while inside of the microscope is shown in Figure 1.29. The imaging quality depends highly on the microscope configuration, and each component is explained below.

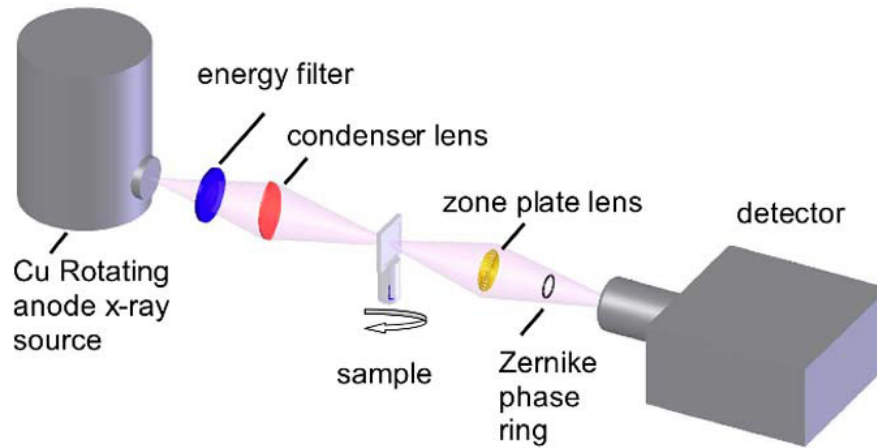


**Figure 1.28** Illustration of the zone-plate based x-ray microscope operating in Zernike phase contrast mode [66].

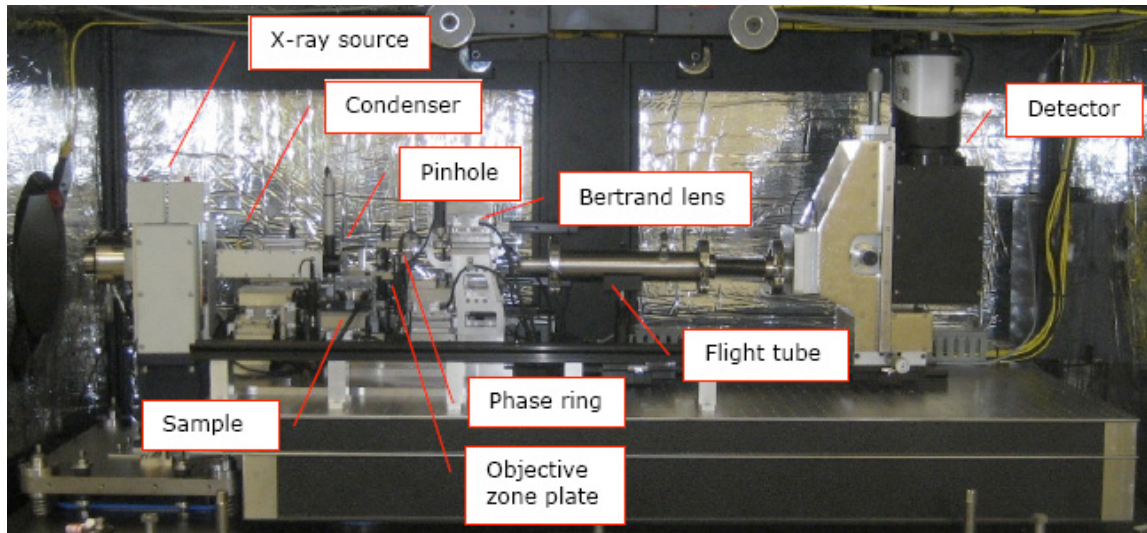


**Figure 1.29** Overview of the nanoXCT components [77].

#### 1.3.4.1 X-ray Source

The x-ray is generated by a rotating anode source with a copper target. The configuration of the x-ray generator is shown in Figure 1.30. The electrons are accelerated from the cathode (tungsten filament) with high voltage to collide into the rotating anode. This causes the electrons of the anode material to move to their excited states. When the electrons fall back to their ground states, x-rays are released with characteristic emission lines. In the case of the copper rotation anode in the nanoXCT system, the highest intensity of the spectrum comes from the  $K_{\alpha}$  line, which is 8keV ( $\sim 0.154$  nm). The x-ray generator is operating under 40 kV and 30 mA, a total of 1.2 kW.

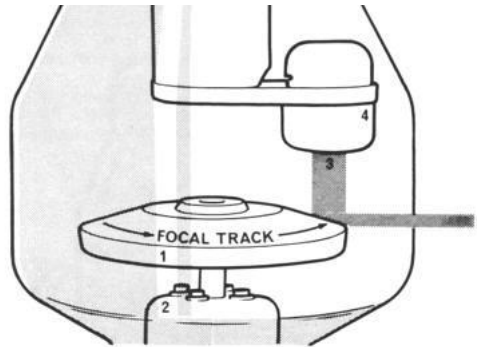


**Figure 1.30** Illustration of a rotation anode x-ray source. The anode target disc (1) rotates on a highly specialized ball bearing system (2). The target is subjected to a focused stream of electrons (3) emanating from the cathode (4) and accelerated by a high potential difference between the target disc and the cathode, when the electron beam hits the anode, it produces the x-ray beam (5) [78].

#### 1.3.4.2 Condenser

The x-rays produced by the x-ray tube are focused with an ellipsoidal parabolic glass capillary. X-rays are captured and reflected off the internal surface of the capillary at glancing angles and focused onto the sample. In the center of the optics there is a Au central stop which prevents x-rays from going straight through without reflection. This creates a hollow cone of illumination. Compared with the commonly used Fresnel zone plate (see next section) as condensers (Figure 1.31(a)), the capillary has larger NA and better focusing efficiency. The focus of the capillary lens experiences aberration from off-axis illumination, rendering it



unsuitable for imaging purposes as an objective, but sufficient as condenser (Figure 1.31(b)). In the nanoXCT system, a pinhole is placed just before the sample in order to isolate the first order of the reflected light.

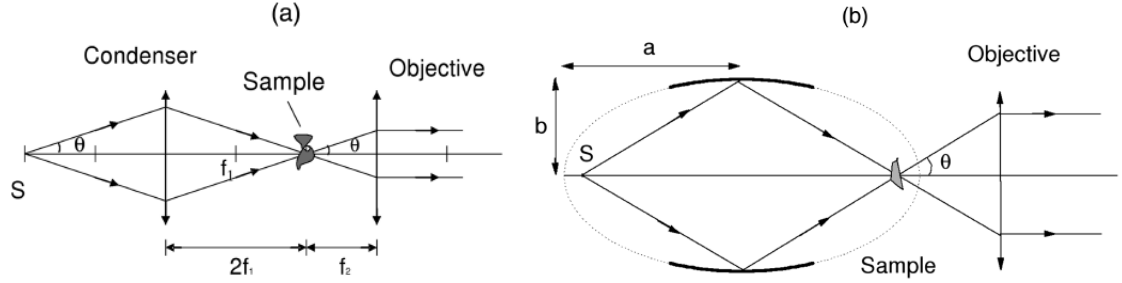


**Figure 1.31** (a) Zone plate as condenser for a laboratory x-ray source. The NA of the condenser zone plate is twice the NA of the objective zone plate. (b) Capillary ellipsoid as condenser [79].

#### 1.3.4.3 Fresnel Zone Plate (Objective)

Fresnel zone plates are diffractive based lenses with circular gratings in which each zone has the same area (Figure 1.32). They are used as the objective of the microscope and determine important properties including resolution and depth of focus. The radii of the zone plate edges ( $r_n$ ) are given by

$$f^2 + r_n^2 = \left(f + \frac{n\lambda}{2}\right)^2$$

where  $n$  is the zone number,  $f$  is the first order focal length and  $\lambda$  is the wavelength. After expansion, the relationship can be expressed by

$$r_n^2 = n\lambda f + \frac{n^2\lambda^2}{4}$$

When using a monochromatic light source, the Fresnel lens follows the thin lens equation

$$\frac{1}{p} + \frac{1}{q} = \frac{1}{f}$$

where  $p$  and  $q$  are object and image distance, and the magnification is

$$M = \frac{p}{q}$$

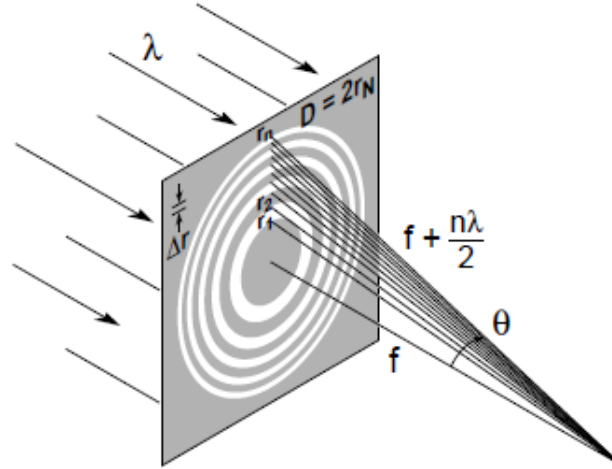


**Figure 1.32** A Fresnel zone plate lens with plane wave illumination showing first order diffraction. Sequential zones of radius are specified so that the incremental path to the focal point is  $n\lambda/2$ . Lens characteristics such as focal length ( $f$ ), diameter ( $D$ ), and numerical aperture ( $NA$ ) are described in terms of  $\lambda$ ,  $N$  (number of zones), and  $\Delta r$ , the outer zone width [65].

The Rayleigh resolution of optics is  $0.61\lambda/NA$ . For a Fresnel zone plate it is equal to  $\frac{\lambda}{2\Delta r}$ , where  $\Delta r$  is the outer zone width. So the Rayleigh resolution becomes directly related to the outer zone width.

$$\delta = 1.22\Delta r$$

This relation is only for parallel coherent illumination shown in Figure 1.32. Better resolutions may be obtained with partial coherent light [65]. The depth of focus (DOF) is related to the numerical aperture, thus also related to the zone width.

$$DOF = \pm \frac{\lambda}{2NA^2} = \pm \frac{2\Delta r_n^2}{\lambda}$$

Resolution and DOF can be traded-off with each other especially for the soft x-ray wavelength. For wavelength of 3 nm using a zone plate with an outer zone width of 35nm, DOF is less than 2  $\mu\text{m}$ . For a 0.15 nm light source, the DOF is about 32  $\mu\text{m}$ .

The limiting factor of the x-ray microscopy resolution comes from the fabrication capability of the zone plates. Currently the outer zone width of 15 nm has been achieved for soft-xray zone plates [68]. For hard x-rays, the zone plate lenses are more difficult to fabricate

because of the required high aspect ratio ( $>10$ ) zone thickness necessary to attenuate high energy x-rays (Figure 1.33). Typically, the higher the aspect ratio, the higher the diffraction efficiency can be, as shown in Figure 1.34. Fabrication efforts to increase the aspect ratio of zone plate include fine-tuning the e-beam lithography process and electrodeposition conditions [71] as well as by doubling aspect ratio by permanently bonding two identical zone plates together [80], as shown in Figure 1.35. The Beckman Institute nanoXCT system has the stacked zone plates, each has outer most zone width of 30 nm and zone height of 450 nm.

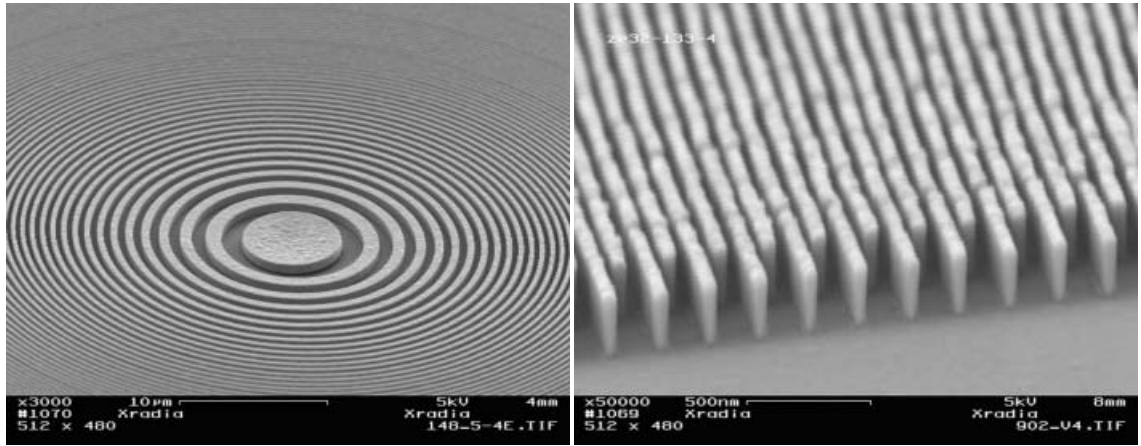


**Figure 1.33** SEM images of a Au Fresnel zone plate used in hard X-ray microscopy. The outermost zone is about 50 nm wide and the zone height is about 450 nm. Two zone plates can be bonded together to increase efficiency [66].

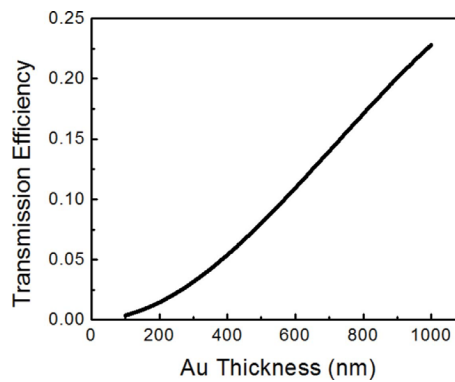


**Figure 1.34** Calculated efficiency as a function of the Au thickness for a zone plate at 8 keV [71].

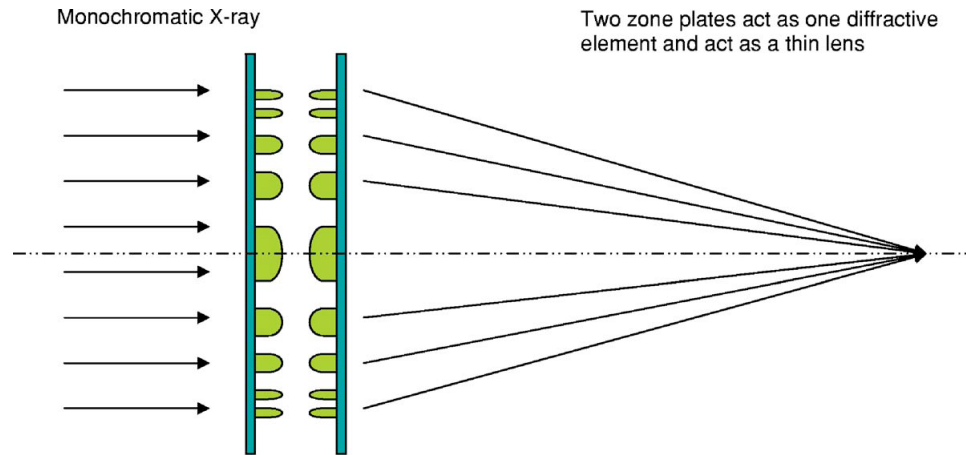


**Figure 1.35** Schematic of two zone plate aligned and bonded together face to face [80].

It is possible to image with higher diffraction orders using the zone plates (Figure 1.36). The higher numerical aperture of higher orders can significantly improve resolution [81]. However the diffraction efficiency drops dramatically with higher orders. For a zone plate, 50% energy is absorbed and 25% is traveling straight in the forward direction (zero order). The first order has theoretical diffraction efficiency around 10%, while the third order only has around 1% [65].

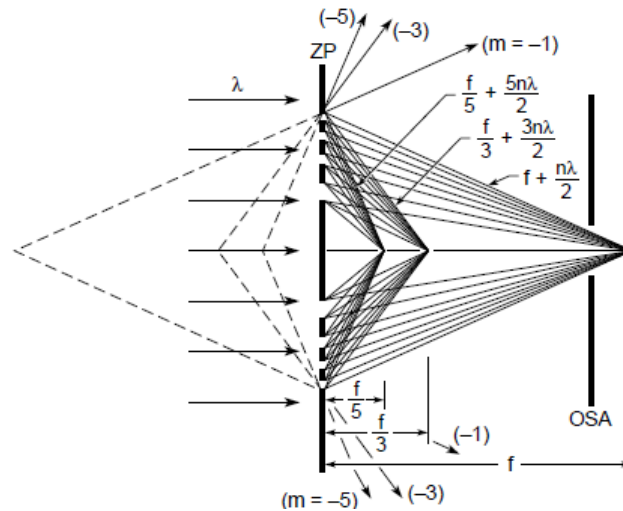


**Figure 1.36** Zone plate diffractive focusing is illustrated for the first three positive orders. An order sorting aperture (OSA) shown is used to block all but the first order. The negative orders are also shown [65].

### 1.3.4.4 Phase ring

The nanoXCT can operate in Zernike phase contrast mode by inserting a phase ring at the back focal plane to phase shift by  $3\pi/2$  the light that is not diffracted by the sample (Figure 1.37). When the diffracted light and un-diffracted light recombine, a phase cancellation of the background is created, producing negative phase contrast. Phase variations can be changed to amplitude variation. The phase ring is made from gold with optimized thickness on a silicon nitride substrate. For the nanoXCT system, the gold ring is about 2.5 microns thick (Figure 1.38) [66].

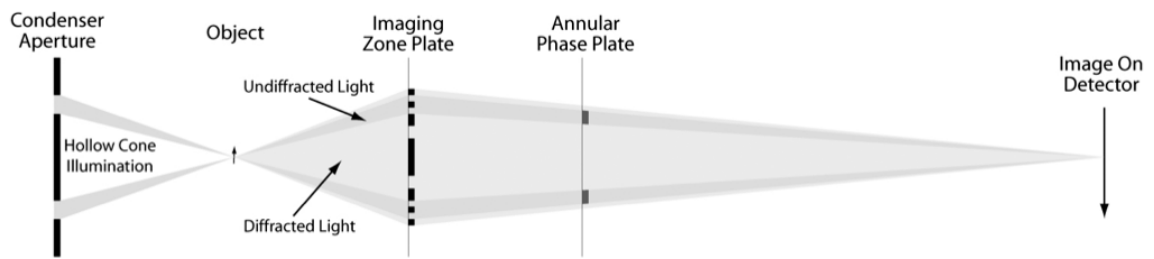


**Figure 1.37** Imaging geometry: capillary reflective condenser produces hollow cone illumination designed to nearly match the NA of the imaging zone plate. The annular phase ring is positioned at the back focal plane of the imaging zone plate to intercept the un-diffracted x-ray light (darker shade of grey). Diameter and width of the phase ring were chosen to intercept all of the un-diffracted light [66].

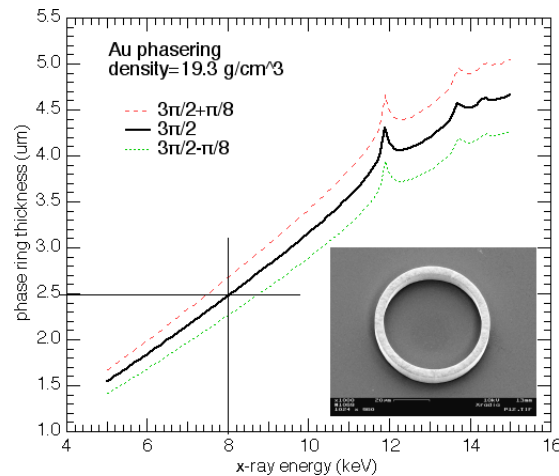


**Figure 1.38** Thickness of the Au phase ring plotted as a function of x-ray energy required to produce a phase shift  $3\pi/2$  (solid curve). The inset is an SEM image of the Au phase ring structure on top of silicon nitride window. The target phase shift ring thickness was selected to produce  $3\pi/2 \pm \pi/8$  phase shift (dashed curves) for optimal negative Zernike phase contrast at 8 keV [66].

Due to the low coherence of the x-ray source and single sample position phase contrast imaging of the nanoXCT system, artifacts can arise from 3D reconstruction. The typical artifacts are bright halos, especially around the edges of the lower spatial frequency features. The resolution is also not as good as in absorption contrast mode, but the sensitivity allows features of the sample be distinguished.

#### *1.3.4.5 Flight tube*

Air consists of mostly nitrogen ( $Z=7$ ) and oxygen ( $Z=8$ ) and can absorb significant amount of x-ray given a long distance. In order to minimize the loss, a flight tube is installed and covers most of the optical path. It is filled with 3 PSI helium ( $Z=2$ ) and sealed with a thin Be ( $Z=4$ ) window.

#### *1.3.4.6 Detector*

The detector is composed of a scintillator screen, an optical objective lens, and a CCD camera (Figure 1.39(a)). Scintillators are optically transparent, non-scattering luminescent screens. They absorb the incoming x-rays and emit visible light. In this case it is a crystal made with high atomic number that is doped with activator impurity elements. The crystal should be made thin to ensure resolution, as shown in Figure 1.39(b), since the planes before and behind the focus at the CCD will add up to the total signal. After the scintillator, a 20x objective magnifies the image before it is projected onto the CCD camera. The CCD camera is from Princeton Instrument model 1024. It has 1024 x 1024 pixel resolution, with each pixel 13 x 13  $\mu\text{m}$  in size.

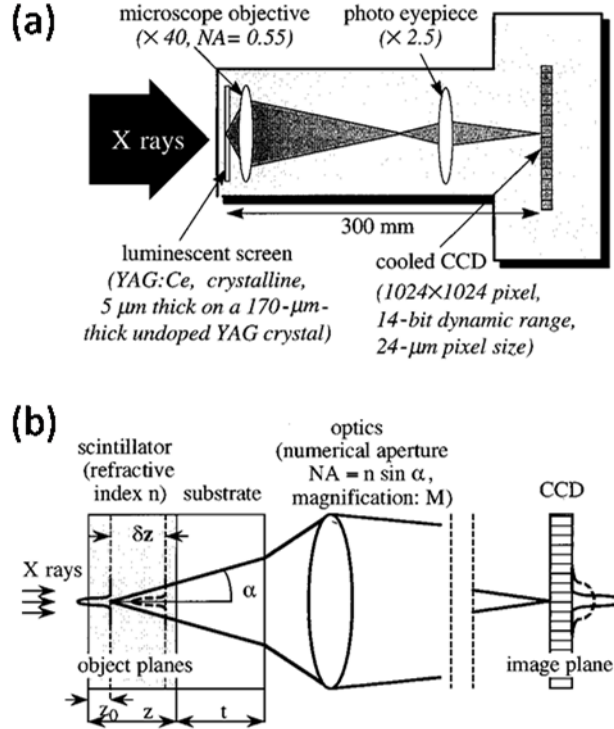


**Figure 1.39** (a) Optical setup of the camera (b) X-ray imaging with scintillators. Identical visible light images are created by the x-ray beam in different planes of the scintillator. An image in plane  $z_0$  is focused on to the CCD (solid curves) while  $z_0 + \delta z$  is not [82].

#### 1.4 References

- [1] <http://ab-initio.mit.edu/photons/tutorial/>.
- [2] J. D. Joannopoulos, P. R. Villeneuve, and S. H. Fan, "Photonic crystals: Putting a new twist on light," *Nature*, vol. 386, pp. 143-149, 1997.
- [3] K. Busch, G. von Freymann, S. Linden, S. F. Mingaleev, L. Tkeshelashvili, and M. Wegener, "Periodic nanostructures for photonics," *Physics Reports-Review Section of Physics Letters*, vol. 444, pp. 101-202, 2007.
- [4] C. Lopez, "Three-dimensional photonic bandgap materials: semiconductors for light," *Journal of Optics a-Pure and Applied Optics*, vol. 8, pp. R1-R14, 2006.
- [5] D. W. Prather, S. Y. Shi, J. Murakowski, G. J. Schneider, A. Sharkawy, C. H. Chen, and B. L. Miao, "Photonic crystal structures and applications: Perspective, overview, and development," *Ieee Journal of Selected Topics in Quantum Electronics*, vol. 12, pp. 1416-1437, 2006.

- [6] Y. A. Vlasov, X. Z. Bo, J. C. Sturm, and D. J. Norris, "On-chip natural assembly of silicon photonic bandgap crystals," *Nature*, vol. 414, pp. 289-293, 2001.
- [7] B. H. Cumpston, S. P. Ananthavel, S. Barlow, D. L. Dyer, J. E. Ehrlich, L. L. Erskine, A. A. Heikal, S. M. Kuebler, I. Y. S. Lee, D. McCord-Maughon, J. Q. Qin, H. Rockel, M. Rumi, X. L. Wu, S. R. Marder, and J. W. Perry, "Two-photon polymerization initiators for three-dimensional optical data storage and microfabrication," *Nature*, vol. 398, pp. 51-54, 1999.
- [8] G. M. Gratson, M. J. Xu, and J. A. Lewis, "Microperiodic structures - Direct writing of three-dimensional webs," *Nature*, vol. 428, pp. 386-386, 2004.
- [9] M. Campbell, D. N. Sharp, M. T. Harrison, R. G. Denning, and A. J. Turberfield, "Fabrication of photonic crystals for the visible spectrum by holographic lithography," *Nature*, vol. 404, pp. 53-56, 2000.
- [10] S. Jeon, V. Malyarchuk, J. A. Rogers, and G. P. Wiederrecht, "Fabricating three dimensional nanostructures using two photon lithography in a single exposure step," *Optics Express*, vol. 14, pp. 2300-2308, 2006.
- [11] S. Y. Lin, J. G. Fleming, D. L. Hetherington, B. K. Smith, R. Biswas, K. M. Ho, M. M. Sigalas, W. Zubrzycki, S. R. Kurtz, and J. Bur, "A three-dimensional photonic crystal operating at infrared wavelengths," *Nature*, vol. 394, pp. 251-253, 1998.
- [12] J. H. Jang, C. K. Ullal, M. Maldovan, T. Gorishnyy, S. Kooi, C. Y. Koh, and E. L. Thomas, "3D micro- and nanostructures via interference lithography," *Advanced Functional Materials*, vol. 17, pp. 3027-3041, 2007.
- [13] M. J. Escuti and G. P. Crawford, "Holographic photonic crystals," *Optical Engineering*, vol. 43, pp. 1973-1987, 2004.
- [14] J. H. Moon, J. Ford, and S. Yang, "Fabricating three-dimensional polymeric photonic structures by multi-beam interference lithography," *Polymers for Advanced Technologies*, vol. 17, pp. 83-93, 2006.
- [15] B. E. A. Saleh and M. C. Teich, *Fundamental of photonics*, Second ed.: John Wiley & Sons, 2007.
- [16] D. B. Mei, B. Y. Cheng, W. Hu, Z. L. Li, and D. H. Zhan, "3-dimensional ordered patterns by light interference," *Optics Letters*, vol. 20, pp. 429-431, 1995.
- [17] V. Berger, O. GauthierLafaye, and E. Costard, "Photonic band gaps and holography," *Journal of Applied Physics*, vol. 82, pp. 60-64, 1997.
- [18] S. Shoji and S. Kawata, "Photofabrication of three-dimensional photonic crystals by multibeam laser interference into a photopolymerizable resin," *Applied Physics Letters*, vol. 76, pp. 2668-2670, 2000.
- [19] S. H. Fan, P. R. Villeneuve, R. D. Meade, and J. D. Joannopoulos, "Design of 3-dimensional photonic crystals at submicron length scales," *Applied Physics Letters*, vol. 65, pp. 1466-1468, 1994.



- [20] M. Maldovan, C. K. Ullal, W. C. Carter, and E. L. Thomas, "Exploring for 3D photonic bandgap structures in the 11 f.c.c. space groups," *Nature Materials*, vol. 2, pp. 664-667, 2003.
- [21] S. G. Johnson and J. D. Joannopoulos, "Three-dimensionally periodic dielectric layered structure with omnidirectional photonic band gap," *Applied Physics Letters*, vol. 77, pp. 3490-3492, 2000.
- [22] L. Z. Cai, X. L. Yang, and Y. R. Wang, "All fourteen Bravais lattices can be formed by interference of four noncoplanar beams," *Optics Letters*, vol. 27, pp. 900-902, 2002.
- [23] C. K. Ullal, M. Maldovan, M. Wohlgemuth, and E. L. Thomas, "Triply periodic bicontinuous structures through interference lithography: a level-set approach," *Journal of the Optical Society of America a-Optics Image Science and Vision*, vol. 20, pp. 948-954, 2003.
- [24] D. C. Meisel, M. Wegener, and K. Busch, "Three-dimensional photonic crystals by holographic lithography using the umbrella configuration: Symmetries and complete photonic band gaps," *Physical Review B*, vol. 70, 2004.
- [25] C. K. Ullal, M. Maldovan, E. L. Thomas, G. Chen, Y. J. Han, and S. Yang, "Photonic crystals through holographic lithography: Simple cubic, diamond-like, and gyroid-like structures," *Applied Physics Letters*, vol. 84, pp. 5434-5436, 2004.
- [26] O. Toader, T. Y. M. Chan, and S. John, "Photonic band gap architectures for holographic lithography," *Physical Review Letters*, vol. 92, 2004.
- [27] D. N. Sharp, A. J. Turberfield, and R. G. Denning, "Holographic photonic crystals with diamond symmetry," *Physical Review B*, vol. 68, 2003.
- [28] J. W. Rinne and P. Wiltzius, "Design of holographic structures using genetic algorithms," *Optics Express*, vol. 14, pp. 9909-9916, 2006.
- [29] T. Y. M. Chan and S. John, "Circuits for light in holographically defined photonic-band-gap materials," *Physical Review A*, vol. 78, 2008.
- [30] S. Yang, M. Megens, J. Aizenberg, P. Wiltzius, P. M. Chaikin, and W. B. Russel, "Creating periodic three-dimensional structures by multibeam interference of visible laser," *Chemistry of Materials*, vol. 14, p. 2831, 2002.
- [31] X. Wang, J. F. Xu, H. M. Su, Z. H. Zeng, Y. L. Chen, H. Z. Wang, Y. K. Pang, and W. Y. Tam, "Three-dimensional photonic crystals fabricated by visible light holographic lithography," *Applied Physics Letters*, vol. 82, pp. 2212-2214, 2003.
- [32] V. Ramanan, E. Nelson, A. Brzezinski, P. V. Braun, and P. Wiltzius, "Three dimensional silicon-air photonic crystals with controlled defects using interference lithography," *Applied Physics Letters*, vol. 92, p. 173304, 2008.
- [33] X. Wang, J. Xu, J. C. W. Lee, Y. K. Pang, W. Y. Tam, C. T. Chan, and P. Sheng, "Realization of optical periodic quasicrystals using holographic lithography," *Applied Physics Letters*, vol. 88, 2006.

- [34] Y. C. Chen, J. B. Geddes, J. T. Lee, P. V. Braun, and P. Wiltzius, "Holographically fabricated photonic crystals with large reflectance," *Applied Physics Letters*, vol. 91, p. 241103, 2007.
- [35] M. Maldovan and E. L. Thomas, "Photonic crystals: six connected dielectric networks with simple cubic symmetry," *Journal of the Optical Society of America B-Optical Physics*, vol. 22, pp. 466-473, 2005.
- [36] Y. K. Pang, J. C. W. Lee, H. F. Lee, W. Y. Tam, C. T. Chan, and P. Sheng, "Chiral microstructures (spirals) fabrication by holographic lithography," *Optics Express*, vol. 13, pp. 7615-7620, 2005.
- [37] S. Shoji, H. B. Sun, and S. Kawata, "Photofabrication of wood-pile three-dimensional photonic crystals using four-beam laser interference," *Applied Physics Letters*, vol. 83, pp. 608-610, 2003.
- [38] Y. V. Miklyaev, D. C. Meisel, A. Blanco, G. von Freymann, K. Busch, W. Koch, C. Enkrich, M. Deubel, and M. Wegener, "Three-dimensional face-centered-cubic photonic crystal templates by laser holography: fabrication, optical characterization, and band-structure calculations," *Applied Physics Letters*, vol. 82, pp. 1284-1286, 2003.
- [39] A. del Campo and C. Greiner, "SU-8: a photoresist for high-aspect-ratio and 3D submicron lithography," *Journal of Micromechanics and Microengineering*, vol. 17, pp. R81-R95, 2007.
- [40] K. Saravanamuttu, C. F. Blanford, D. N. Sharp, E. R. Dedman, A. J. Turberfield, and R. G. Denning, "Sol-gel organic-inorganic composites for 3-D holographic lithography of photonic crystals with submicron periodicity," *Chemistry of Materials*, vol. 15, pp. 2301-2304, 2003.
- [41] M. Salauen, M. Audier, F. Delyon, and M. Duneau, "3-D holographic lithography of organic-inorganic hybrids," *Applied Surface Science*, vol. 254, pp. 830-835, 2007.
- [42] M. C. George, E. C. Nelson, J. A. Rogers, and P. V. Braun, "Direct Fabrication of 3D Periodic Inorganic Microstructures using Conformal Phase Masks," *Angewandte Chemie-International Edition*, vol. 48, pp. 144-148, 2009.
- [43] Y. Jun, P. Nagpal, and D. J. Norris, "Thermally stable organic-inorganic hybrid photoresists for fabrication of photonic band gap structures with direct laser writing," *Advanced Materials*, vol. 20, pp. 606-610, 2008.
- [44] J. H. Jang, C. K. Ullal, T. Gorishnyy, V. V. Tsukruk, and E. L. Thomas, "Mechanically tunable three-dimensional elastomeric network/air structures via interference lithography," *Nano Letters*, vol. 6, pp. 740-743, 2006.
- [45] A. Hayek, Y. G. Xu, T. Okada, S. Barlow, X. L. Zhu, J. H. Moon, S. R. Marder, and S. Yang, "Poly(glycidyl methacrylate)s with controlled molecular weights as low-shrinkage resins for 3D multibeam interference lithography," *Journal of Materials Chemistry*, vol. 18, pp. 3316-3318, 2008.

- [46] J. H. Kang, J. H. Moon, S. K. Lee, S. G. Park, S. G. Jang, S. Yang, and S. M. Yang, "Thermoresponsive hydrogel photonic crystals by three-dimensional holographic lithography," *Advanced Materials*, vol. 20, pp. 3061-3065, 2008.
- [47] M. J. Escuti, J. Qi, and G. P. Crawford, "Tunable face-centered-cubic photonic crystal formed in holographic polymer dispersed liquid crystals," *Optics Letters*, vol. 28, pp. 522-524, 2003.
- [48] S. Wong, M. Deubel, F. Perez-Willard, S. John, G. A. Ozin, M. Wegener, and G. von Freymann, "Direct laser writing of three-dimensional photonic crystals with complete a photonic bandgap in chalcogenide glasses," *Advanced Materials*, vol. 18, pp. 265-269, 2006.
- [49] J. H. Moon, S. Yang, W. T. Dong, J. W. Perry, A. Adibi, and S. M. Yang, "Core-shell diamond-like silicon photonic crystals from 3D polymer templates created by holographic lithography," *Optics Express*, vol. 14, pp. 6297-6302, 2006.
- [50] J. S. King, E. Graugnard, O. M. Roche, D. N. Sharp, J. Scrimgeour, R. G. Denning, A. J. Turberfield, and C. J. Summers, "Infiltration and inversion of holographically defined polymer photonic crystal templates by atomic layer deposition," *Advanced Materials*, vol. 18, pp. 1561-1565, 2006.
- [51] Y. Xu, X. Zhu, Y. Dan, J. H. Moon, V. W. Chen, A. T. Johnson, J. W. Perry, and S. Yang, "Electrodeposition of three-dimensional titania photonic crystals from holographically patterned microporous polymer templates," *Chemistry of Materials*, vol. 20, pp. 1816-1823, 2008.
- [52] M. Miyake, Y. C. Chen, P. V. Braun, and P. Wiltzius, "Fabrication of Three-Dimensional Photonic Crystals Using Multibeam Interference Lithography and Electrodeposition," *Advanced Materials*, vol. 21, pp. 3012-3015, 2009.
- [53] J. Scrimgeour, D. N. Sharp, C. F. Blanford, O. M. Roche, R. G. Denning, and A. J. Turberfield, "Three-dimensional optical lithography for photonic microstructures," *Advanced Materials*, vol. 18, pp. 1557-1560, 2006.
- [54] E. Yablonovitch, "Photonic crystals: Semiconductors of light," *Scientific American*, vol. 285, pp. 46-55, 2001.
- [55] D. Shir, E. C. Nelson, Y. C. Chen, A. Brzezinski, H. Liao, P. V. Braun, P. Wiltzius, K. H. A. Bogart, and J. A. Rogers, "Three dimensional silicon photonic crystals fabricated by two photon phase mask lithography," *Applied Physics Letters*, vol. 94, p. 011101, 2009.
- [56] H. Ito, "Chemical amplification resists for microlithography," in *Microlithography - Molecular Imprinting*. vol. 172, 2005, pp. 37-245.
- [57] K. Y. Lee, N. LaBianca, S. A. Rishton, S. Zolgharnain, J. D. Gelorme, J. Shaw, and T. H. P. Chang, "Micromachining applications of a high resolution ultrathick photoresist," 1995, pp. 3012-3016.
- [58] J. V. Crivello and K. Dietliker, *Photoinitiators for Free radical Cationic & Anionic Photopolymerisation.*, 2nd ed. vol. III: John Wiley & Sons, 1998.

- [59] Y. Yagci and I. Reetz, "Externally stimulated initiator systems for cationic polymerization," *Progress in Polymer Science*, vol. 23, pp. 1485-1538, 1998.
- [60] J. V. Crivello, "The discovery and development of onium salt cationic photoinitiators," *Journal of Polymer Science Part a-Polymer Chemistry*, vol. 37, pp. 4241-4254, 1999.
- [61] Y. B. Bi and D. C. Neckers, "A visible-light initiating system for free-radical promoted cationic polymerization," *Macromolecules*, vol. 27, pp. 3683-3693, 1994.
- [62] R. Bowser and R. S. Davidson, "Iron arene complexes as free-radical and cationic photoinitiators," *Journal of Photochemistry and Photobiology a-Chemistry*, vol. 77, pp. 269-276, 1994.
- [63] V. Jakubek and A. J. Lees, "Wavelength dependent photochemistry of an iron-arene organometallic photoinitiator: a quantitative study of the photoreactivity," *Chemical Communications*, pp. 1631-1632, 1999.
- [64] T. Wang, B. S. Li, and L. X. Zhang, "Carbazole-bound ferrocenium salt as an efficient cationic photoinitiator for epoxy polymerization," *Polymer International*, vol. 54, pp. 1251-1255, 2005.
- [65] D. Attwood, *Soft X-ray and Extreme Ultraviolet Radiation*, 1 ed.: Cambridge University Press, 2007.
- [66] A. Tkachuk, F. Duewer, H. T. Cui, M. Feser, S. Wang, and W. B. Yun, "X-ray computed tomography in Zernike phase contrast mode at 8 keV with 50-nm resolution using Cu rotating anode X-ray source," *Zeitschrift Fur Kristallographie*, vol. 222, pp. 650-655, 2007.
- [67] B. C. Larson and B. Lengeler, "High-resolution three-dimensional x-ray microscopy," *MRS Bulletin*, vol. 29, pp. 152-154, 2004.
- [68] W. L. Chao, B. D. Harteneck, J. A. Liddle, E. H. Anderson, and D. T. Attwood, "Soft X-ray microscopy at a spatial resolution better than 15nm," *Nature*, vol. 435, pp. 1210-1213, 2005.
- [69] P. Kirkpatrick and A. V. Baez, "Formation of optical images by x-rays," *Journal of the Optical Society of America*, vol. 38, pp. 766-773, 1948.
- [70] M. Young, "Zone plates and their aberrations," *Journal of the Optical Society of America*, vol. 62, pp. 972-976, 1972.
- [71] Y. T. Chen, T. N. Lo, C. W. Chiu, J. Y. Wang, C. L. Wang, C. J. Liu, S. R. Wu, S. T. Jeng, C. C. Yang, J. Shiue, C. H. Chen, Y. Hwu, G. C. Yin, H. M. Lin, J. H. Je, and G. Margaritondo, "Fabrication of high-aspect-ratio Fresnel zone plates by e-beam lithography and electroplating," *Journal of Synchrotron Radiation*, vol. 15, pp. 170-175, 2008.
- [72] A. Snigirev, V. Kohn, I. Snigireva, and B. Lengeler, "A compound refractive lens for focusing high-energy X-rays," *Nature*, vol. 384, pp. 49-51, 1996.

- [73] C. G. Schroer, P. Cloetens, M. Rivers, A. Snigirev, A. Takeuchi, and W. B. Yun, "High-resolution 3D imaging microscopy using hard x-rays," *MRS Bulletin*, vol. 29, pp. 157-165, 2004.
- [74] A. Momose, "Recent advances in X-ray phase imaging," *Japanese Journal of Applied Physics Part 1-Regular Papers Brief Communications & Review Papers*, vol. 44, pp. 6355-6367, 2005.
- [75] P. Cloetens, W. Ludwig, J. Baruchel, D. Van Dyck, J. Van Landuyt, J. P. Guigay, and M. Schlenker, "Holotomography: Quantitative phase tomography with micrometer resolution using hard synchrotron radiation x rays," *Applied Physics Letters*, vol. 75, pp. 2912-2914, 1999.
- [76] A. C. Kak and M. Slaney *Principles of Computerized Tomographic Imaging*: IEEE Press. , 1988.
- [77] *Xradia nanoXCT laboratory user tool manual*, 2008.
- [78] <http://www.e-radiography.net/nickspdf/RS%20Introduction%20to%20Rotating%20Anode%20X-ray%20tube.pdf>
- [79] X. H. Zeng, F. Duewer, M. Feser, C. Huang, A. Lyon, A. Tkachuk, and W. B. Yun, "Ellipsoidal and parabolic glass capillaries as condensers for x-ray microscopes," *Applied Optics*, vol. 47, pp. 2376-2381, 2008.
- [80] Y. Feng, M. Feser, A. Lyon, S. Rishton, X. H. Zeng, S. Chen, S. Sassolini, and W. B. Yun, "Nanofabrication of high aspect ratio 24 nm x-ray zone plates for x-ray imaging applications," pp. 2004-2007, 2007.
- [81] G. C. Yin, Y. F. Song, M. T. Tang, F. R. Chen, K. S. Liang, F. W. Duewer, M. Feser, W. B. Yun, and H. P. D. Shieh, "30 nm resolution x-ray imaging at 8 keV using third order diffraction of a zone plate lens objective in a transmission microscope," *Applied Physics Letters*, vol. 89, p. 221122, 2006.
- [82] A. Koch, C. Raven, P. Spanne, and A. Snigirev, "X-ray imaging with submicrometer resolution employing transparent luminescent screens," *Journal of the Optical Society of America a-Optics Image Science and Vision*, vol. 15, pp. 1940-1951, 1998.

## CHAPTER 2

### FABRICATION OF PHOTONIC CRYSTAL TEMPLATES WITH MULTIBEAM INTERFERENCE LITHOGRAPHY

#### 2.1 Introduction

Interference lithography, including multibeam interference lithography and phase mask lithography, is among the most promising techniques for the fabrication of three-dimensional photonic crystals [1]. In this method, the periodic patterns of the crystals are generated and recorded in photosensitive materials via interference of multiple coherent laser beams. This technique is attractive due to its versatility in creating different crystalline symmetries and bases, facilitating the experimental demonstration of various structures. Holographically defined polymer photonic crystals can serve as templates for the subsequent deposition of high refractive index materials for applications requiring a pseudo- or complete photonic band gap. To incorporate functionality using the band gap, controlled defects can be placed into the crystals via multiphoton polymerization either by using the same photoresist before hologram development or by infiltrating the developed structure with other recordable media.

Photonic crystals fabricated by multibeam interference lithography are expected to exhibit excellent optical properties due to their large areas and defect-free nature. However, previously reported peak reflectances of multibeam fabricated polymer crystals are only around 30%, while reflectances from self-assembled colloidal crystals can exceed 70% with the same number of layers [2]. This underwhelming optical response of the polymeric crystal template would set an upper bound on the optical properties of structures and components formed via replication with high dielectric constant materials. Through the past few years we have been able to develop the fabrication route to significantly improve the optical properties. In this chapter, details outlining of fabrication and improvement of this method are presented and discussed.

Figure 2.1 shows typical a 3D photonic crystal fabricated in our lab using multibeam interference lithography.

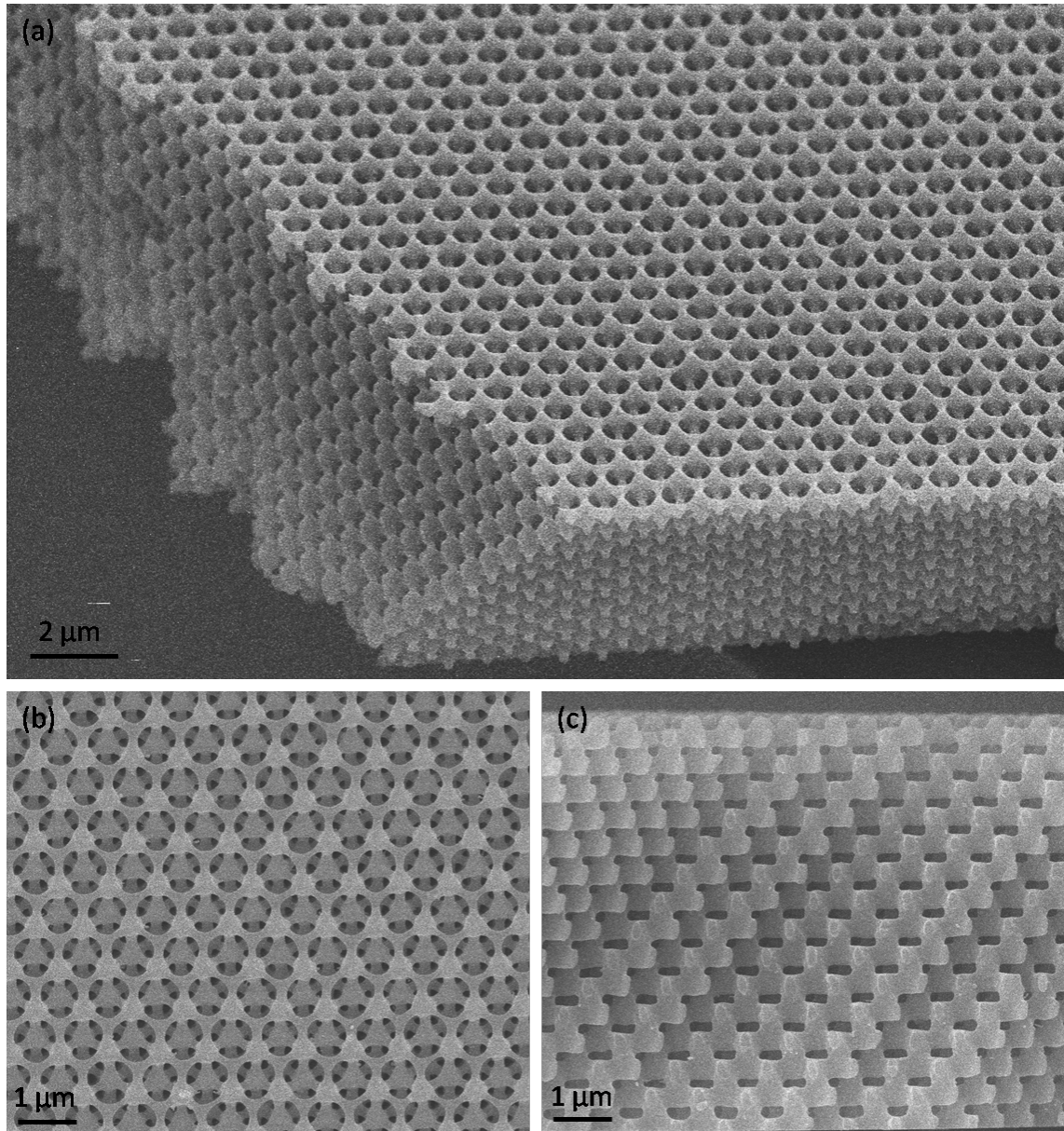


**Figure 2.1** Scanning electron micrograph of a 3D photonic crystal fabricated by multibeam interference lithography. (a)  $\sim 45^\circ$  viewing angle (b) top view (c) cross-section

## 2.2 Optical Setup

### 2.2.1 Laser

For a multi-beam interference setup, the laser needs to have long coherence length (narrow frequency range) for the beams to remain in phase at the target after travelling through all the optical elements. The laser should have high enough power so that the exposure time can be minimized. In addition, the high power allows the beam being expanded to fabricated larger and more uniform crystals. The laser we used for the multi-beam interference setup is a diode pump solid state laser at 532 nm. Compare to the normally used UV wavelengths, this wavelength is advantageous for a typical photoresist system such as SU-8.

The first laser that was installed for the setup, Compass 315M (Coherent Inc.), was a frequency doubled Nd:YAG laser with a maximum power of 150 mW and beam diameter of 0.34 mm (where intensity value is  $1/e^2$  of maximum intensity). The relatively low power required long exposure times (~20 sec) which made the sample susceptible to vibration during exposure. Since the beam has Gaussian intensity distribution within its diameter, across its small area there was a large intensity variation. With Compass 315M, crystal fabrication was often unstable and irreproducible, and the resultant structures had poor optical properties. The second laser installed was Verdi 5W (Coherent Inc.), a frequency doubled Nd:YVO<sub>4</sub> laser that has maximum power of 5.5 W and beam diameter of 2.25 mm. In addition to higher power, the laser also has smaller beam divergence and better stability than the Compass 315M. The crystal quality and process reproducibility improved immediately after the laser upgrade. Due to the ample power of the laser, we can expand the beam diameter by a factor of four and retain acceptable exposure times under 1 second.

### 2.2.2 Optical Table and Vibration Control

For nano-scale patterning, the vibration of the optical setup needs to be carefully controlled in order to prevent the original pattern being smeared during the exposure period. Our



optical setup has a rigid table top (Newport RS-4000) to minimize relative motion of the elements on the table, and pneumatic isolators (Newport I-2000) that float the table and damp the vibration coming from the building (especially important as our lab is on the fourth floor). The optics mounted on the table was kept as low as possible since vibration from the table could amplify with height. For the sample mount, which has to be positioned high off the table, a rigid structural rail (Newport X95) is used. We saw considerable improvements in crystal quality when changing the elevating post from a standard rod post to the structural rail. Sound damping panels were also installed in the room in order to minimize vibration; however there were no noticeable effect.

### 2.2.3 *Spatial Filter*

A spatial filter was installed in the laser beam path in order to both expand and clean up the beam. The spatial filter is composed of a microscope objective lens to focus the laser beam and a pinhole at the focal point to block diffraction rings and let only the central zero order beam through. The resulting laser beam is “cleaned up” because the aberrations due to imperfections such as dust are removed. After the pinhole another lens is used to re-collimate the beam. In this case the position of the lens was chosen to make the beam diameter four times larger than the original so that a bigger crystal can be fabricated.

### 2.2.4 *Waveplates and Beamsplitters*

The rest of the optics in this setup can be seen in Figure 2.2. The laser beam is split into four and arranged by mirrors into an umbrella geometry [3] —one central beam perpendicular to the table, and three equally spaced side beams around it.

The power ratios between the beams are controlled by a polarizing cube beam splitter with a half waveplate before it. The half waveplate is used to adjust the polarization direction and the beam is split by the cube according to its polarization: s-polarization turns  $90^\circ$  and p-

polarization goes straight through. Therefore the power ratio of the split can be controlled by adjusting the fast axis of the half waveplate before the beamsplitter. The final polarizations of the four beams are tuned by additional waveplates: half waveplates for the side beams for their linear polarization, a quarter waveplate for the central beam for its circular polarization [4].

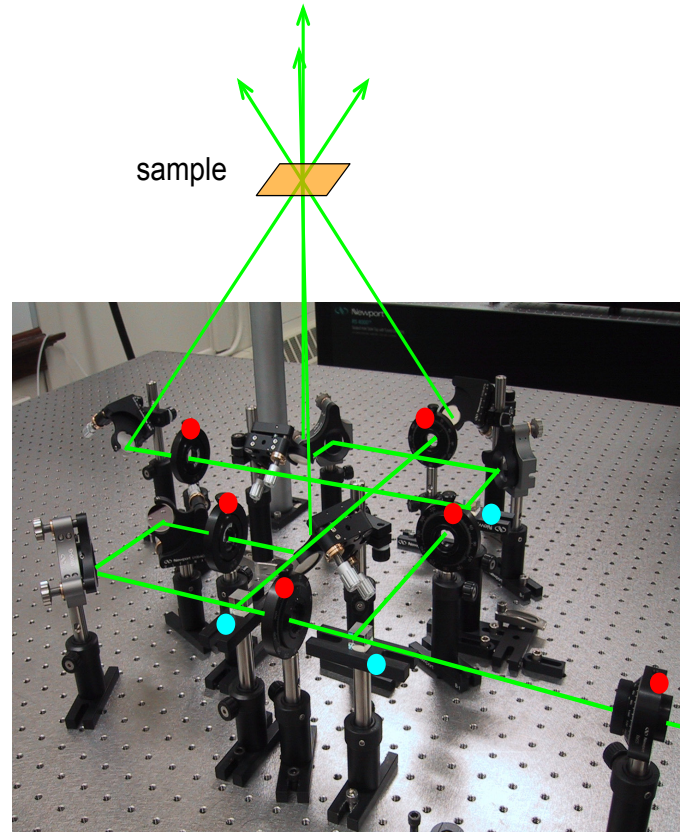


**Figure 2.2** Optical setup of four beam interference.

### 2.2.5 Alignment Process

A diagram of umbrella beam geometry optics arrangement is first drafted. The optical paths for each of the four beams are planned to be equal, and the optical elements are not in the way of other beams. Alignment starts from beam geometry followed by intensity ratio and finally polarization. An adjustable aperture is placed on the beam path with its center aligned with the highest intensity point (not necessary at the geometric center) of the laser beam using a beam profiler. The aperture is opened wide during exposure but is adjusted to a small opening to allow

a defined circular shape for easy alignment. The aperture is also used as a screen to detect beam reflection from the optical components.

The central beam is aligned perpendicular to the table using mirrors. The mirror mounts have lockable fine adjustment screws on its two turning axis. The alignment is checked by fixing a paper screen on the sample holder and marking the beam position. If the central beam is properly aligned, the spot on the screen remains at the same marked position when the sample holder is moving up and down the post. The sample stage has fine screws for two-axis tilt adjustment. A cover glass is put on the stage and tilt is tuned so the reflection of the central beam projected back in to the alignment aperture. This means the central beam is perpendicular to the sample. The three side beams are aligned to the designated conversion point. Four screens (a glass slide with paper tape) of equal heights are set up just on top of the last mirrors of each beam. While the four beams converge, the spots on the screens should form an equilateral triangle with the central beam in the mid-point. The screen is set up close to the table so that the triangle formed is large enough to take an accurate measurement.

The polarization of each beam is tuned with the last waveplate of each beam and measured with a polarizer and a power meter. For linear polarization, the polarizer is aligned to the designed polarization (or its projection), and the waveplate is tuned to a position where the intensity passing the polarizer is maximum. For circular polarization, the waveplate is tuned to where power measurement does not change when turning the polarizer.

The beam is profiled after each component to check for dust on the optics, and the optics are cleaned with nitrogen and methanol or acetone as necessary. The setup is covered with plastic bag after each use. Certain artifacts can come from imperfection of the optics, especially from the cube beamsplitter where two prisms are glued together. The ideal solution would be to have an individual spatial filter for each beam after passing through all the optics. In our case the optics are moved to where minimal artifacts are presented.

## 2.3 Photoresist Systems

A suitable photoresist system for 3D photonic crystal fabrication with multibeam interference lithography should have the following requirements. First, the resist should be able to form a uniform thick film of up to tens of microns and be thermally and mechanically stable. The system should have high sensitivity to the patterning wavelength, so that exposure time is minimized and the resolution is not compromised by vibration. However the resist also needs to have minimal absorption so that exposure is reasonably uniform across the thickness of the film. The contrast and resolution must be high because the features are on the order of tens of nanometers, even though the periodicity is hundreds of nanometers. There should also be minimal intrinsic shrinkage of the resist patterning process, so that the recorded patterns are not distorted.

### 2.3.1 SU-8 Photoresist

SU-8 has been the most popular photoresist system used since the holographic method was demonstrated for photonic crystal fabrication. The commercialized SU-8 photoresist system (Microchem) is made sensitive to the UV wavelength range and comes in varying solvent contents for different spin coating conditions. SU-8 can also be made sensitive to green wavelengths by mixing different sensitizer/photoacid generator and SU-8 monomer [5]. We tried to form the resist solution from mixing solid SU-8 monomer with solvent (cyclopentanone / tetrahydrofuran / gamma-butyrolactone), however we found the resulting solution does not have good spin-coating properties -- the spin-coated film is not smooth. We decided to form the resist by adding initiator and sensitizer to the commercialized Microchem SU-8, because it has special additives that promote spin coating flat films.

When the laser beam enters into the photoresist, its direction changes due to refraction. The angle is determined by the refractive index of the exposed photoresist following Snell's law:

$$n_1 \sin \theta_1 = n_2 \sin \theta_2$$

where  $n_1$  and  $n_2$  are refractive indices and  $\theta_1$  and  $\theta_2$  are the incidence angles. It is important to know the dispersion of both the cured and uncured SU-8. For the four beam umbrella setup, the side beams enter the photoresist at a shallower angle depending on the refractive index at the exposure wavelength. When characterizing the photonic crystal made with SU8, the refractive index value is also required for optical spectroscopy. The refractive index measurement is taken using spectroscopic ellipsometry and the result is shown in Figure 2.3.

The cured and uncured SU-8 have very similar refractive indices and follow the same dispersion curve. The uncured SU-8 has only slightly higher refractive index than the cured SU-8 at all wavelengths. The index values drop rapidly from 1.72 to 1.6 between 300nm and 600nm and leveling off around 1.58. For uncured SU-8, the refractive index is 1.674 at 351nm, 1.607 at 532 nm, and 1.588 at 800 nm. According to Snell's law, the corresponding glancing angles are  $36.68^\circ$  for 351 nm,  $38.48^\circ$  for 532 nm, and  $39.03^\circ$  for 800 nm.

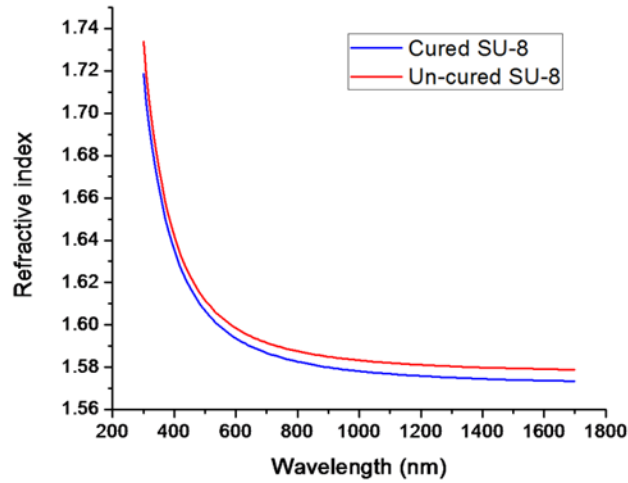


**Figure 2.3** SU-8 refractive index dispersion between 300 nm and 1700 nm measured by ellipsometry. The cured SU-8 is shown in blue and the uncured is shown in red.

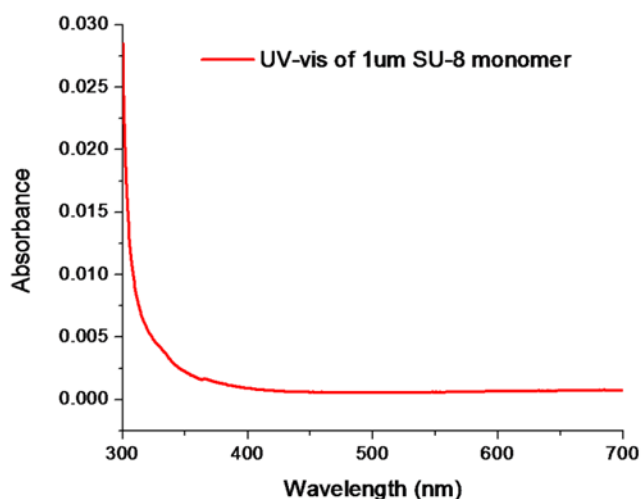


**Figure 2.4** SU-8 monomer UV-vis measurement.

SU-8 monomer, which is the bulk of the photoresist, absorbs strongly at 300nm but becomes transparent around 400 nm (Figure 2.4). The intrinsic absorption of SU-8 determines the uniformity of exposure through the thickness of the photoresist and can in turn significantly affect the uniformity of the fabricated photonic crystal. Thus patterning with a wavelength longer than 400 nm is highly desirable.

### 2.3.2 Photoinitiators

Two different photoinitiation systems were tested. The first system consists of a sensitizer and a photoacid generator (PAG) (Figure 2.5(a)). In the commercialized SU-8 the resist has mixed triarylsulfonium/hexafluoroantimonate salt as PAG. However this PAG does not absorb 532 nm, and as mentioned in chapter 1.2, the sulfonium salts cannot be easily sensitized. A diaryliodonium salt, Uvacure1600 (phenyl-p-octyloxyphenyl-iodonium hexafluorantimonate) is added to the system together with sensitizers. When exposed to light, the sensitizer absorbs photons and transfers energy to Uvacure1600. This generates protons, and at elevated temperatures begins cationic polymerization at the SU-8 epoxide functional groups. In the second case, the photoacid generator itself absorbs enough green light, and no sensitizer is needed

(Figure 2.5(b)). We find the PAG-only system yields much better results, both in terms of efficiency and quality of the template fabricated (see chapter 3 for characterization result).

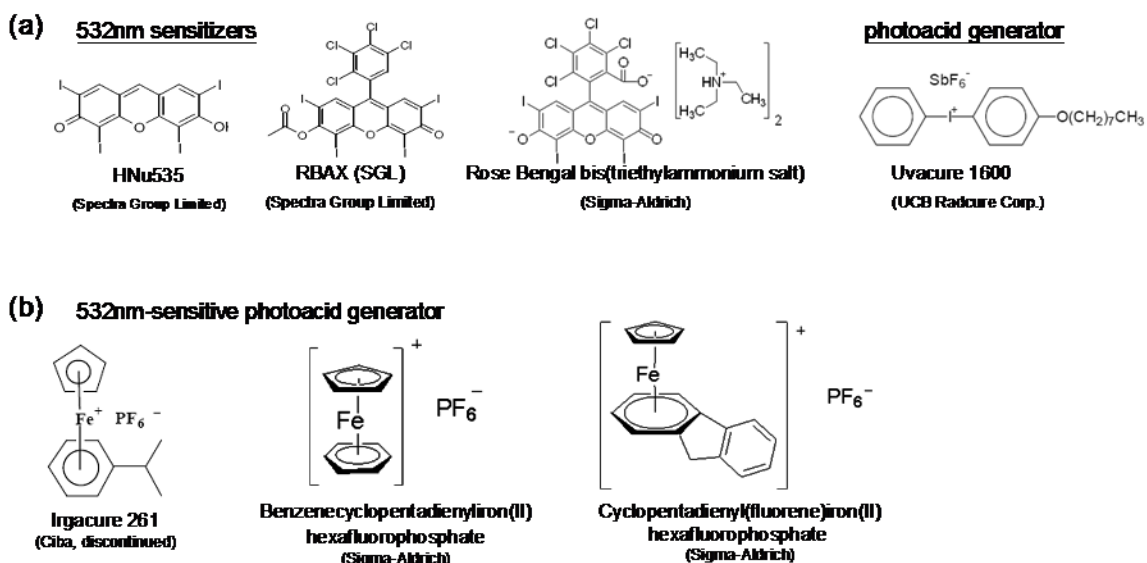


**Figure 2.5** Photoinitiator systems for 532nm (a) sensitizer + PAG system (b)PAG-only system.

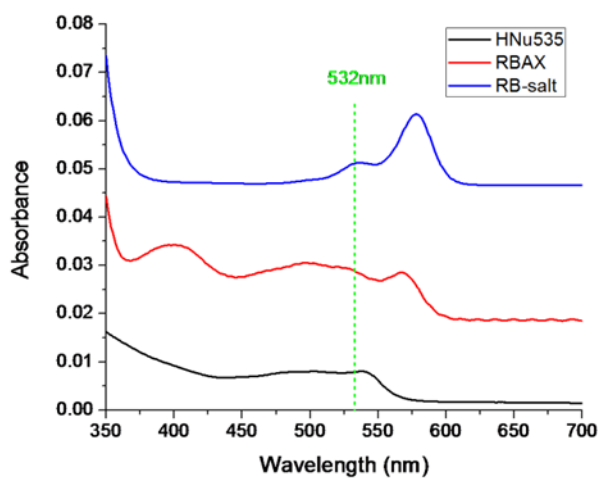


**Figure 2.6** UV-vis spectra of the sensitized photoresist systems.

Figure 2.6 shows the UV-vis spectra of the sensitized photoresist system film (including sensitizer, PAG and SU-8). The values are normalized for a 1  $\mu\text{m}$  thick film. Among the three sensitizers, we first tested HNu535 because of a favorable report in the literature [5]. However

the sensitizer proved to be difficult to work with—it is both hard to dissolve and has inconsistent performance. RBAX is much easier to dissolve and showed more consistent patterning within the same batch. However later batches purchased did not show the same good results. The sensitizer rose bengal bis(trimethylamonium salt) (Aldrich) was not found reported literature. However it has comparable performance to RBAX and has both high solubility and good batch to batch consistency. It is also much cheaper than the other two options. A commercially available 532 nm free-radical initiator, Irgacure 786, can also be used as a sensitizer in combination with a photoacid generator, as shown in Figure 2.7. It was briefly tested on SU-8 with one beam patterning, and the exposed spot was successfully polymerized.

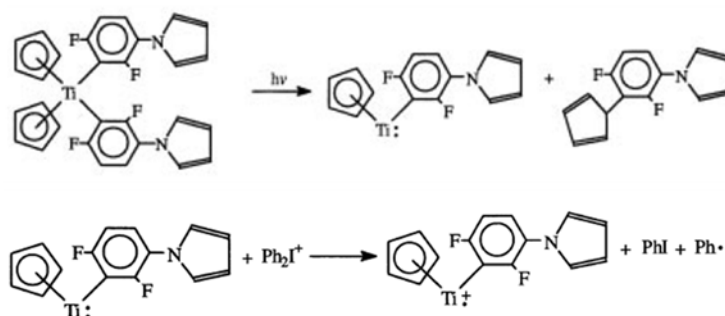


**Figure 2.7** Irgacure 784 as photosensitizer for green light [6].

Iron arene complexes are used as PAG that is sensitive to 532 nm. Irgacure 261 was first reported for use in holographic lithography for photonic crystal fabrication at 532 nm as photoinitiator by [7, 8]. However Irgacure 261 has been discontinued from Ciba Chemicals several years ago. Two suitable iron complexes with similar chemical structures to Irgacure 261, benzenecyclopentadienyliron(II) hexafluorophosphate and cyclopentadienyl(fluorine)iron(II) hexafluorophosphate were found in the Sigma-Aldrich catalog. Although they were not advertized as photoacid generator, both turned out to be very efficient PAGs for 532 nm. While these PAGs have very low absorption at 532 nm as shown in Figure 2.8, they are much more sensitive than the two component system, which is optimal for our application. Three



dimensional photonic crystals fabricated with iron-arene complex supplemented SU-8 photoresist systems were found to have excellent optical performance, as can be seen in the next chapter.

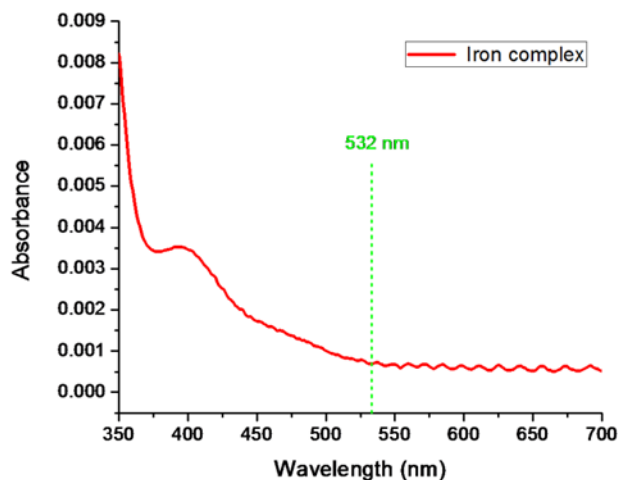


**Figure 2.8** UV-vis spectra of 1  $\mu\text{m}$  SU-8 photoresist film with 2% cyclopentadienyl(fluorine)iron(II) hexafluorophosphate.

## 2.4 Fabrication Process

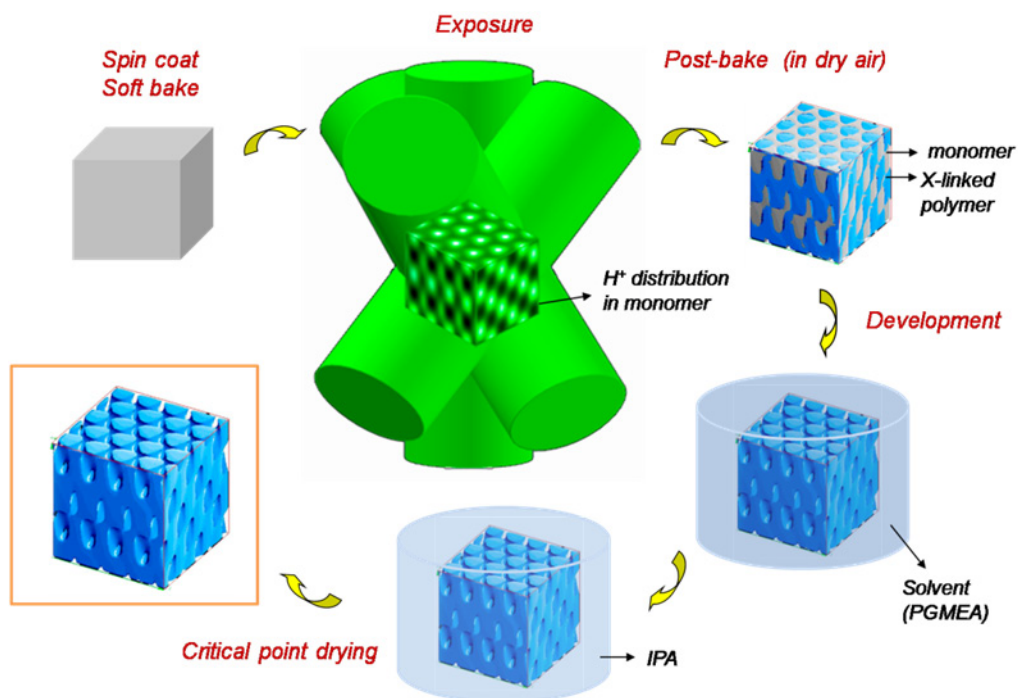


**Figure 2.9** Patterning process of SU-8 photoresist.

#### 2.4.1 Photoresist and Substrate Preparation

The photoresist solution is formed by dissolving the photoinitiators (powder) in cyclopentanone (solvent) for over half an hour before adding SU-8 resins and stirring overnight. Two typical photoresist recipes are listed in Table 2.1.

To fabricate the photonic crystals, we first started with a cover glass substrate. A large cover glass (50x40mm) is used and will be cut into smaller pieces for exposure. Other substrates such as a silicon wafer may be used but anti-reflection coatings may be needed. SU-8 has poor adhesion to glass and without special treatment the crystal often delaminates from the substrate during the development stage. To promote adhesion between glass and SU-8, either a fully crosslinked SU-8 layer is made in between or the glass substrate is cleaned with RIE. Prior to the treatment the substrate is cleaned with soap, water, acetone and isopropanol. The fully crosslinked adhesion layer was made with SU-8 2000 series following the recipe on the datasheet. RIE condition was with 10 sccm O<sub>2</sub> at 150W for 3 minutes. All other adhesion promoting techniques were found to be ineffective at providing strong enough adhesion for the 3D photonic crystal fabrication. When using RIE for adhesion, the substrate should be used immediately; the adhesion layer can last for about a week.

(a)

Rose Bengal bis(triethylammonium salt)	0.04g
Uvacure 1600	0.1g
Cyclopentanone	1g
SU8 2010	10g

(b)

Cyclopentadienyl(fluorine)iron(II) Hexafluorophosphate	0.0672 g
Cyclopentanone	1.8422 g
Dimethyl formamide	0.0626 g
SU8 2025	19 g

**Table 2.1** Customized SU-8 photoresist recipes (a) with sensitizer and photoacid generator (b) with Iron complex photoinitiator.

### 2.4.2 Spin Coat

The spin coat recipe recommended by Microchem Corp. starts at ramping from static to 500 rpm in 5-10 seconds with 100 rpm/second ramping speed followed by spinning at 2000 rpm for 30 seconds with 300 rpm/second acceleration. The thickness of the spin coated film is a function of the spin coating speed and SU-8 concentration. Figure 2.10 shows the variation of film thickness with SU-8 concentration with two spin coating speed (data from Microchem). Note that the relationship is not linear, since the resist viscosity changes non-linearly with the concentration as well as spinning speed. To achieve thickness between 5 $\mu$ m and 45 $\mu$ m with 2000 rpm spin speed, the thickness can be predicted with a fitted curve:

$$y = \begin{cases} 4.63 * 10^{-6} e^{x/4.35} + 10.34 & (x < 58) \\ 0.01x^2 - 0.08x + 0.67 & (x > 58) \end{cases}$$

where  $x$  is the SU-8 concentration and  $y$  is the film thickness. This relation is useful for predicting film thickness for a given concentration or vice-versa. Comparing the case of 1000rpm and 2000rpm, it is experimentally easier to achieve the desired thickness with higher spinning speed because it is less sensitive to concentration variation.

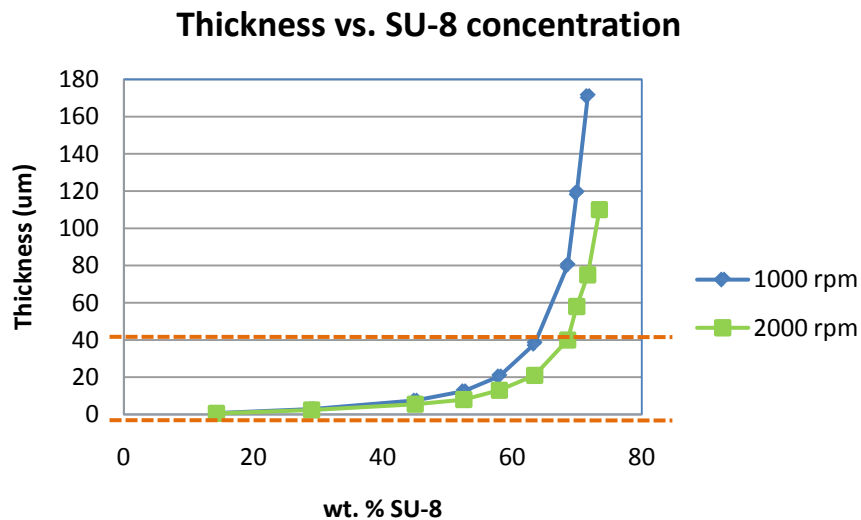


**Figure 2.10** Film thickness with variation of SU-8 concentration at spin coating speeds of 1000 rpm and 2000 rpm. The targeted region is between the two dashed lines (5 $\mu$ m and 45 $\mu$ m). Data is taken from Microchem SU-8 data sheet. Plotted by Arianne Collopy.

#### 2.4.3 *Soft Bake*

After spin coating the film is soft baked to remove solvent. A hotplate is preferred over an oven for soft bake, especially for thick films. When using an oven, the top of the film will dry first and may trap the solvent in the inner layer, causing non-uniformity and stress. Too much residual solvent in the film will cause strong acid diffusion and patterns would be washed out as a result. Since the polymerization reaction is affected by the solvent content, the soft bake condition should be consistent across all samples. After soft bake, the film is cooled for 10 minutes before the exposure step.

#### 2.4.4 *Exposure*

Prior to exposure, the edge of the large cover glass substrate was removed due to thickness variation (edge beads), and the remainder was cut into smaller pieces for exposure. The sample stage was set up so that the convergence spot of the four beams aligns within the sample. To minimize reflection from the substrate, a PDMS block is attached to the back side of the substrate and a black block is attached to the PDMS with water to absorb the laser beam. PDMS is added because it provides optical contact to the glass substrate and is can be peeled off easily. The sample setup is illustrated in Figure 2.11. The exposure is timed by electric shutter.

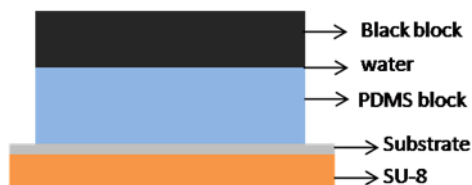


**Figure 2.11** Sample setup for reflection minimization. Laser beams enter from the SU-8 side.

#### 2.4.5 *Post bake*

The post bake should be done immediately after exposure. Delay of this step can cause a lower degree of polymerization due to surface contamination. In addition, polymerization occurs

slowly after exposure at room temperature. It has been observed that after exposure without postbaking for one day, there can be enough crosslinking to form a polymerized spot after development. Because water can cause chain transfer or chain termination in epoxy polymerization (Figure 1.7) and humidity in the lab varies from day to day, the post bake is done in a vacuum oven with controlled atmosphere (compress air from a gas tank). We found that polymerization was inhibited with the oven under vacuum or pure nitrogen. This suggests that oxygen participates the initiation reaction. Dry air is used in the post baking process – after putting the exposed sample into the vacuum oven, the original air is removed and dry air from the tank is purged in.

#### 2.4.6 *Development*

After post bake and cool down, the sample is immersed in propylene glycol monomethyl ether acetate (PGMEA) to dissolve the unexposed regions. Our typical development time is about one hour but it may change depending on the thickness of the film. Slight agitation using magnetic stirrers can help speed up the process. Although many solvents can dissolve SU-8 monomer, not all can thoroughly develop the patterns at the sub-micron level. Solvents tested include acetone, cyclopentanone, THF and gamma-butyrolactone. Among all, PGMEA can resolve the three-dimensional structure most clearly. During development step, the monomer dissolves and the crosslinked polymer swells. If the polymer dries directly out of the PGMEA after development, it would have very poor mechanical properties and the original 3D structure often collapses. Thus after the development, the structure is immersed in isopropanol (IPA), which is a poor solvent for SU-8. The polymer shrinks back under IPA, and mechanical strength is greatly enhanced. If there were still monomers present, they will precipitate out as SU-8 “colloids”, making the solution cloudy. To prevent the monomer that originally dissolved in PGMEA from precipitating onto the crystal, the crystal was rinsed in fresh PGMEA before the transfer. Intermediate solution transfer (mixing IPA with PGMEA, with increasing amounts of

IPA) has been tested. However the optical properties of the direct transfer samples are better than those that are gradually transferred.

#### 2.4.7 Critical Point Drying

A critical point drying technique was applied to the sample to prevent structural collapse or deformation due to surface tension of the solvent during the normal drying process. The method works by going around the liquid-vapor interface of the drying medium passing the critical point. The most common medium for critical point drying is carbon dioxide. Figure 2.12 shows the phase diagram of CO<sub>2</sub> and the critical point drying route. Our patterned sample is transferred completely from IPA to liquid CO<sub>2</sub> in the critical point dryer (Samdri 790) sample chamber at around 0 °C. The chamber is then heated in a controlled fashion so that the pressure and temperature follows a path that go pass the critical point (A-B). After around 15 minutes, the pressure was slowly returned to atmosphere and the sample is cooled to room temperature (B-C).

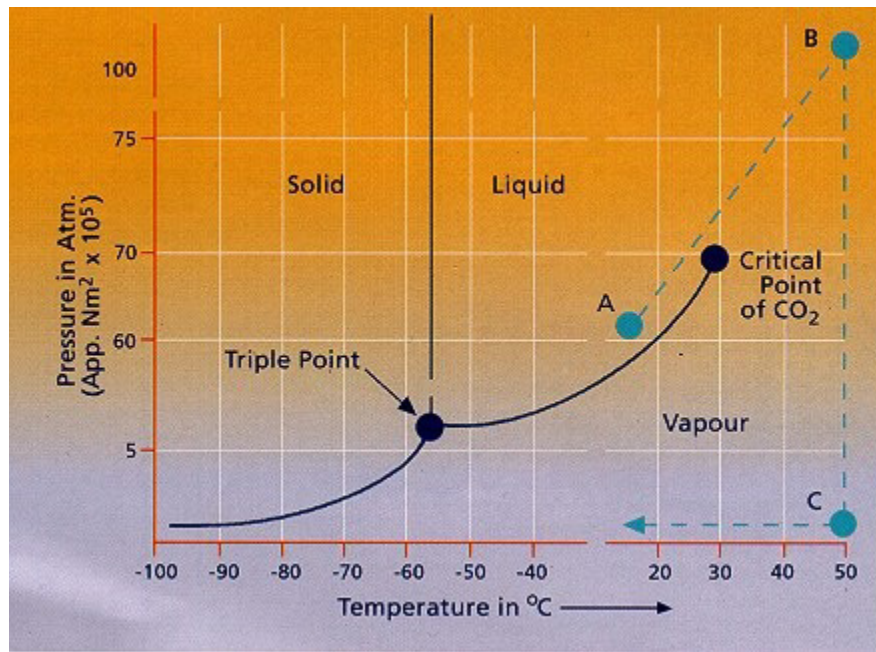


**Figure 2.12** Phase diagram of carbon dioxide and the critical point drying route [9].

## 2.5 Patterning Result

### 2.5.1 Geometry Variation

The customized SU-8 photoresist system has displayed excellent recording properties for multibeam interference lithography using 532 nm laser light source. Figure 2.13 shows the 1D, 2D and 3D periodic pattern results. Figure 2.13(a) is a film patterned with two beam interference. The SU-8 line features have aspect ratio of ~15 and the cross-section was obtained by simple fracture. This demonstrates the ideal mechanical properties of SU-8 as a thick photoresist. Figure 2.13(b) is also patterned by 2 beam interference but turning the sample 90° for the second exposure. The 3D crystal in Figure 2.13(c) is patterned by single exposure of 4 beam interference. The photoresist recipe is listed in Table 2.1(b).

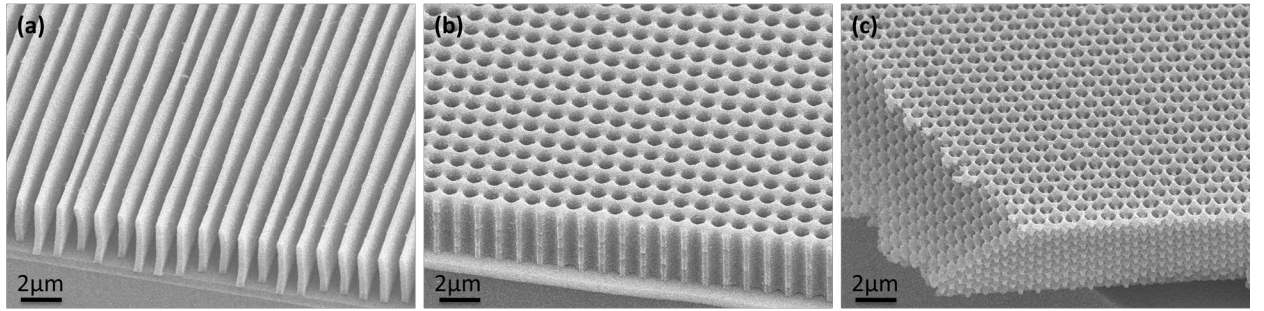


**Figure 2.13** 1D, 2D, 3D periodic patterns generated by interference lithography. Pictures were taken at ~45° tilted angle.

For the four beam umbrella geometry, the dimensions within the crystals change with the angle between the central beam and side beams (the degree which the umbrella opens). Larger angles between the beams lead to smaller periodicity in the crystal. The periodicity generated by two beam interference can be calculated using relation presented in 1.1.2 (Figure 1.2). Using the same principle, we can calculate the periodicity of the 4 beam interference structure shown in Figure 2.14 with simple formulations:

$$a = \frac{2\lambda}{\sqrt{3} \sin \theta} , \quad 3d = \frac{\lambda}{2 \sin^2(\frac{\theta}{2})}$$

where  $a$  is the in-plane periodicity and  $d$  the layer spacing.  $\lambda$  and  $\theta$  are the refractive index corrected wavelength and the central-side beam angle inside the photoresist respectively. Figure 2.15 shows two structures fabricated with  $\theta=25.5^\circ$  and  $\theta=11.9^\circ$ . The smaller angles the larger the periodicities are.

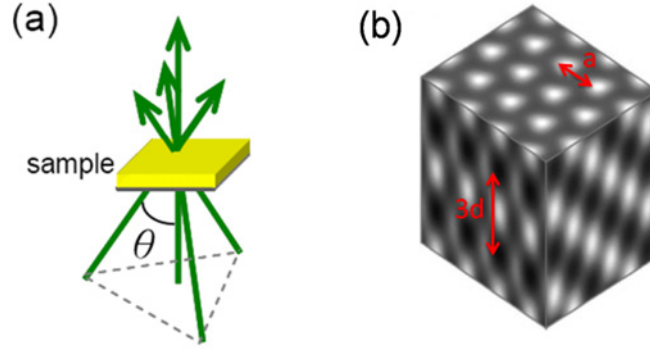


**Figure 2.14** Illustration of the periodicity of the 4 beam umbrella interference pattern.  $a$  is the lateral spacing and  $3d$  the repeating vertical unit length with  $d$  representing the single layer spacing.

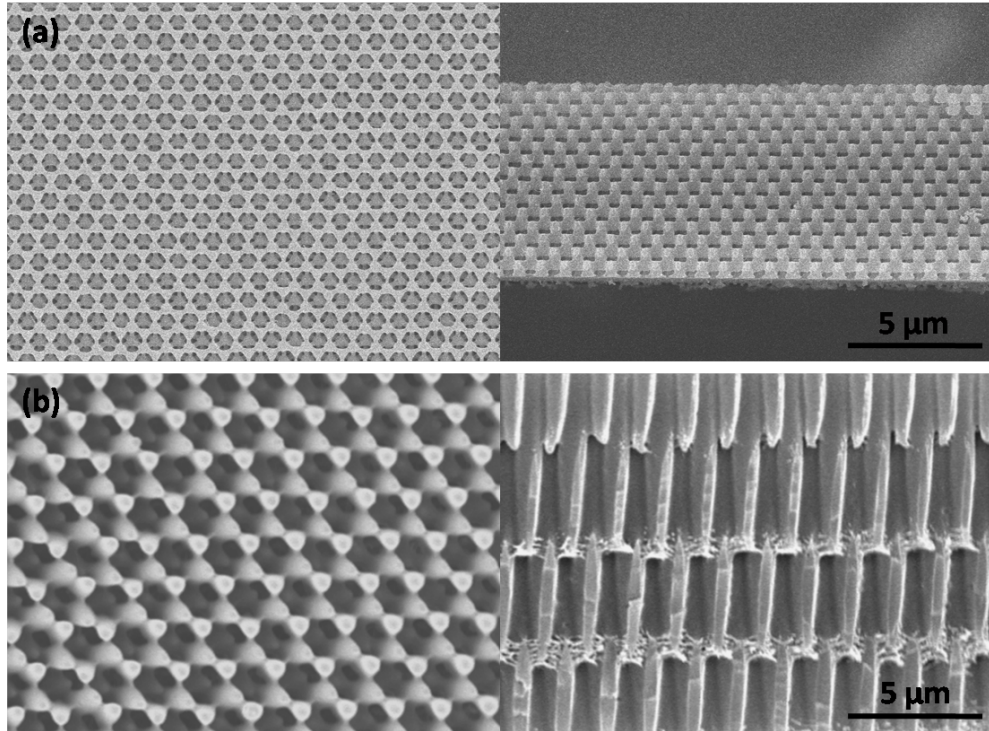


**Figure 2.15** SEM pictures of photonic crystals generated by two different beam geometries. (a)  $\theta=25.5^\circ$  (b)  $\theta=11.9^\circ$ .



To generate a face-centered cubic interference geometry the umbrella angle must be set to  $\theta = 38.9^\circ$ . However as mentioned in section 2.3.1, the largest possible (non-glancing) angle to enter the photoresist for 532 nm light is  $38.48^\circ$ . To overcome this problem, Miklyaev et.al applied a customized prism to couple the light in (Figure 2.15(a))[4]. We have attempted the prism coupling with a more economical prism design, as shown in Figure 2.16(b)&(c). It is formed by a glass plate and three right angle prisms attached using Norland optical adhesive. During exposure, the substrate is bound to the glass plate using glycerol as index matching fluid, and a block of PDMS is placed on top of the photoresist to couple the light away. The sample was stabilized on the setup for 10 minutes before exposure.

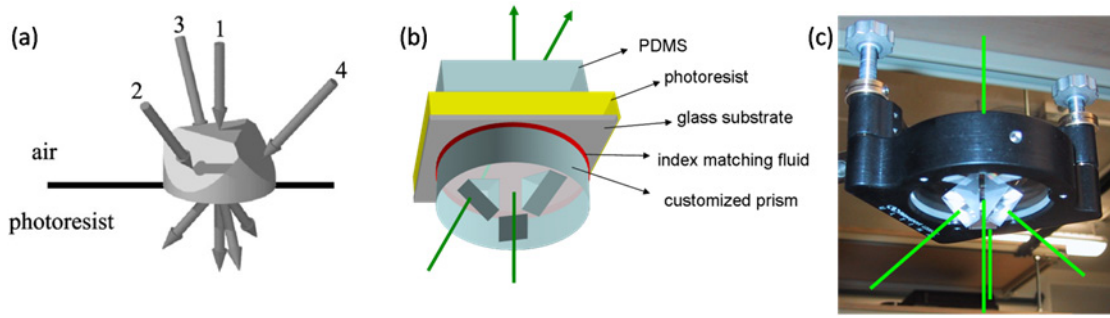


**Figure 2.16** (a) customized prism for coupling light into photoresist from reference [4] (b) sample and prism assembly for exposure (c) picture of the mounted prism setup.

Crystals with much smaller periodicities can be patterned with prism coupling. In-plane periodicity of 0.62 microns was achieved, which is very close to the targeted 0.61 microns for an FCC structure. However, experimental complications arose with the use of prism prevented the fabrication of targeted ideal structures. Although the 3D structures can be seen within the film for a typical fabricated structure, the top layer is usually sealed, as shown in Figure 2.16 (a). The FIB cross-sections, shown in Figure 2.16(b)&(c), also confirm that a periodic three-dimensional structure was fabricated. One reason was severe surface contamination from the PDMS which either neutralized or disabled the photo generated acid. The under-crosslinked SU-8 does not

have strong enough mechanical properties to retain its 3D shape but also cannot be removed by the developer. To test this theory, one film was exposed twice as long as the normal exposure time. This would normally create a fully crosslinked film without 3D patterns. However, as shown in Figure 2.17(d)&(e), the surface of the film showed defined 3D patterns while the rest of the film was over-polymerized. This issue may be potentially solved with a protective overcoat or by reactive ion etching away the top layer of the photoresist before development.

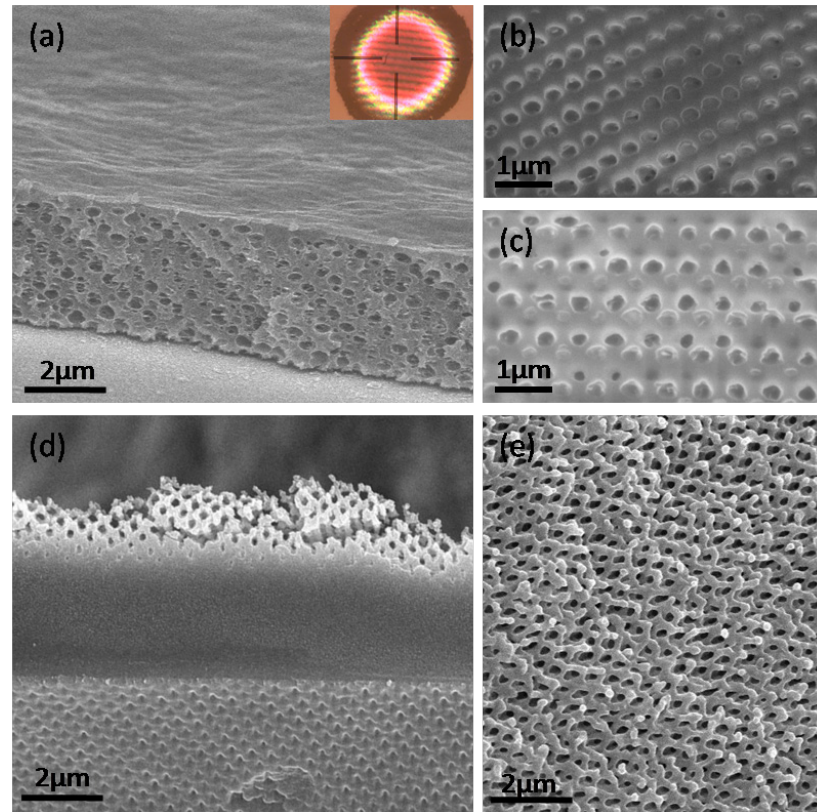


**Figure 2.17** SEM of SU-8 photonic crystals created with prism coupling. (a)-(c) sample with 14 seconds exposure (d)(e) sample with ~30 seconds exposure (a) crystal showing a sealed top (b)(c) FIB cross-section (d) cross-section (tilted up due to delaminating from substrate (e) top view)

The inset of Figure 2.17(a) is an optical micrograph of the fabricated photonic crystal. The concentric rings originate from the Gaussian intensity distribution of the laser beam. The strips that are going across the spot indicate the slight tilt of the film surface to the (111) plane,

and are cutting across the optical plane. Larger spacings between the strips would indicate a better alignment. The central uniform area is around 0.3 mm. In this experiment the laser light source was Compass 315M and the beam was expanded by three times. The sensitizer-PAG patterning photoresist system was used. The prisms were not tested with the Verdi laser and the iron-arene SU-8 photoresist. This is because the realization of the structural shrinkage in the vertical direction from the patterning process. Since it is possible to compensate for shrinkage with creating an elongated interference pattern, prism coupling became unnecessary.

### 2.5.2 Polarization and Intensity Variation

In 3D interference lithography, the periodicity is determined by the beam geometry while the basis is determined by the relative polarization and intensity ratio. When determining polarizations and intensity ratios for a certain geometry, several factors need to be considered include photonic band properties, intensity contrast and bi-continuity threshold regions. We have tested three polarization schemes for the umbrella interference setup. Their projections on the sample are shown in Figure 2.18.

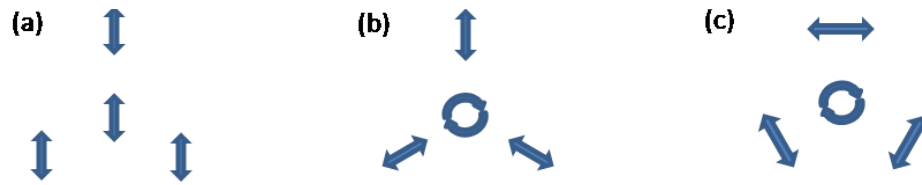


**Figure 2.18** Polarization configurations with projection on sample. (a) All linear polarizations with maximum parallel components, (b) circularly polarized central beam and linearly P-polarized side beams, (c) polarized central beam and linearly S-polarized side beams.

The configuration (a) can provide the highest contrast but has very small or no polymer-air bicontinuous intensity threshold range with the interested beam angle. This means that the structure will either not develop because solvent cannot access the monomer, or the crosslinked

regions will fall apart because they are not connected. The intensity pattern is shown in Figure 2.19(a) and the two non-bicontinuous cases are shown in Figure 2.19(b)&(c). The orbs are highly elongated and were hard to make connect sideways without blocking vertical passage for the developer. Furthermore, the structure does not have the potential to be a photonic band gap structure because of the lack of rotational symmetry.

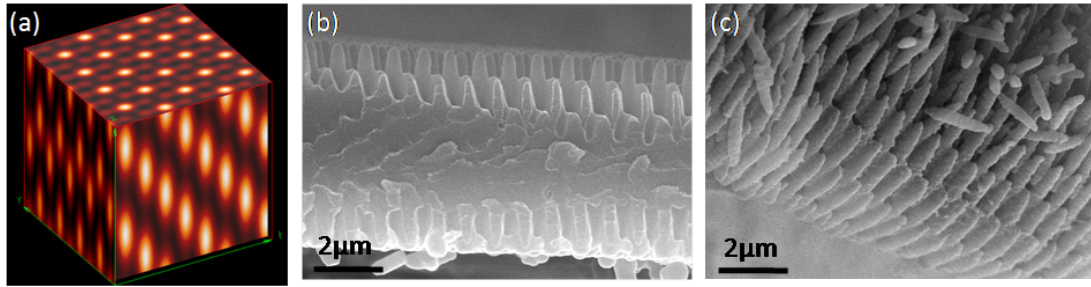


**Figure 2.19** (a) Intensity distribution with maximum parallel polarization (b) non-bicontinuous air (c) non-bicontinuous polymer.

Polarization (b) was first proposed by Miklyaev et.al. [4]. The symmetric beam geometry can generate a structure with a diamond-like photonic band diagram. This band structure has two band gaps, with the larger one at the lower frequency range, which is less sensitive to scattering or imperfections (Figure 2.20). The bi-continuous region is large for this polarization configuration. For beam angle  $25^\circ$  and intensity ratio of 3.7 (central beam to side beam), the filling fraction ranges from 22% to 82% (Figure 2.21(a)).

Polarization configuration (c) was suggested by Dr. Raphi Dror from SOREQ NRC in Israel. By switching the side beam polarization from P-type to S-type, the bi-continuous region increases without sacrificing much in the way of photonic band properties. For the same geometry and intensity ratio, the bi-continuous range increases by around 7% while maintaining large contrast. For optimized intensity ratio of this setup, the bi-continuous range can be increased further. Dr. Dror also suggested the parameter of  $I_{\text{high}}/I_{\text{low}}$  (where  $I_{\text{high}}$  is the intensity value at the high filling fraction boundary and  $I_{\text{low}}$  is the low boundary) is a better indication of

ease of fabrication rather than the common contrast value  $I_{\max}/I_{\min}$ . The reason is because if a structure has  $I_{\min} \sim 0$ , the contrast would approach infinity and be meaningless. As shown in Figure 2.21, the S-polarization should be easier to fabricate due to its large bi-continuous range.

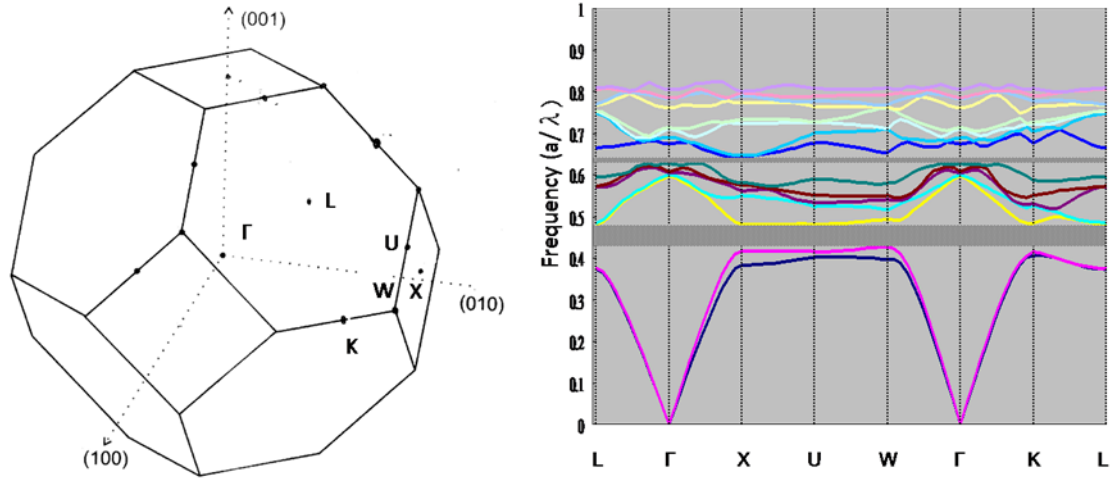


**Figure 2.20** Band diagram of diamond-like structure created by multi-beam interference lithography. Shaded gray area represents band gap region.

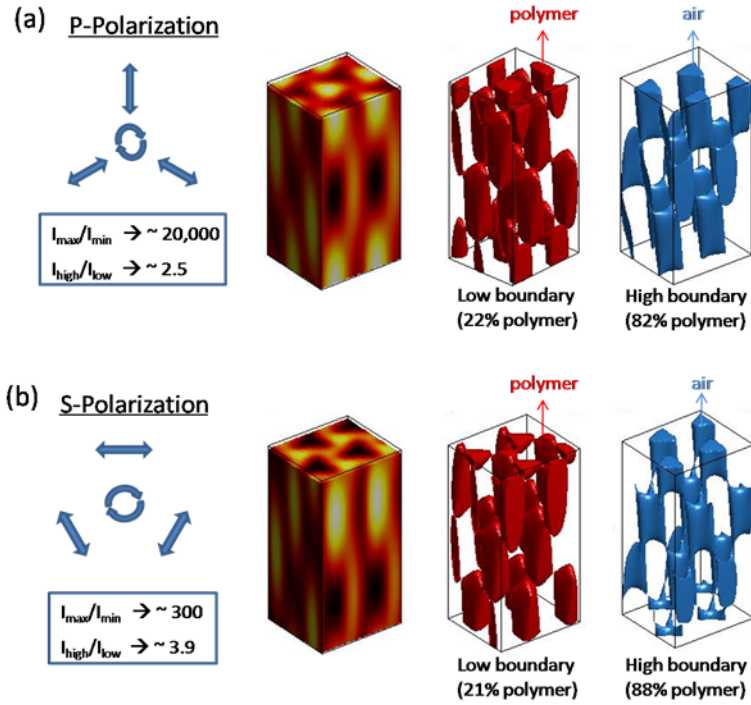


**Figure 2.21** Comparison of P and S polarization configurations. The angle between the central beam and side beam is fixed at  $25^\circ$ , and the intensity ratio is 3.7 (central beam/side beam)



The patterning results of using the two polarization conditions in Figure 2.20 are quite comparable. The samples shown in Figure 2.21 are processed together to minimize variation due to other processing factors. The two samples look almost identical, except the S-polarized sample has a flatter and better defined top surface possibly due to its larger in-plane polarization components from the side beams.

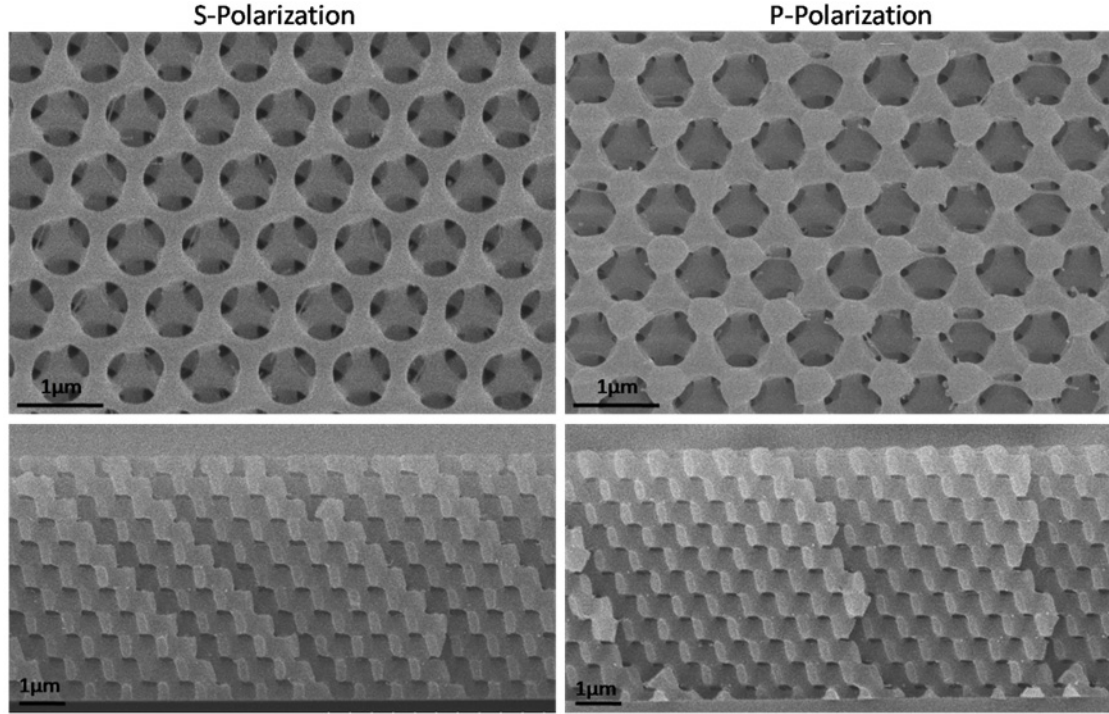


**Figure 2.22** SEM pictures of samples fabricated with P and S polarization configurations.

### 2.5.3 Polymerization Threshold Control

The degree of polymerization from the same intensity pattern can be varied with exposure dose, postbake temperature, and addition of base additives such as thresholding agent. The thresholding agent addition was first demonstrated by Yang et al. [5] by using triethylamine to neutralize the background intensity in order to increase contrast in holographic lithography systems (Figure 2.23). We were able to replicate the triethylamine thresholding effect with our sensitized photoresist system. However we found that the base tends to make the resist insensitive or unstable, and the result was not consistently reproducible. A common proton trap

for cationic polymerization, 2,6-di-tert-butylpyridinium was tested instead and it was proved to work well with the sensitized photoinitiator systems. For the iron complex system however, even with PAG:base = 1:2, the polymerization degree remained unaffected.

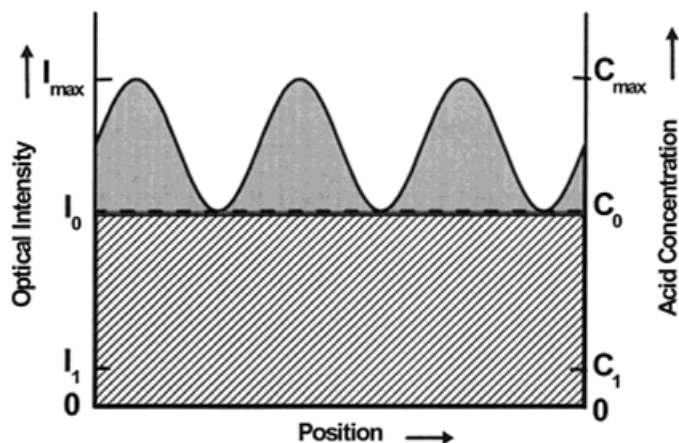


**Figure 2.23** Non-zero backgrounds (slashed area) of the light intensity/dose and the resulting acid concentration generated in the interference pattern [5].

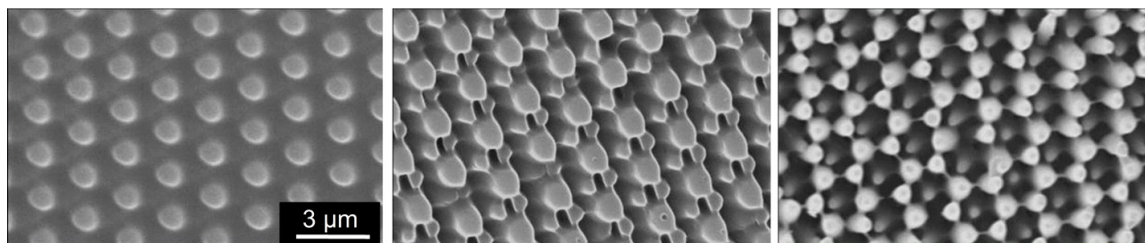


**Figure 2.24** SEM pictures of samples patterning from the same intensity profile with increasing threshold level.

#### 2.5.4 Shrinkage

Comparing the periodicity of the fabricated structure to the calculated intensity pattern, we noticed that there is significant shrinkage in the vertical direction that can range from 10% to 60%, depending on the processing condition of the crystal. The more crosslinking or the larger the pattern (meaning the smaller the central-side beam angle), the less shrinkage takes place. Shrinkage does not occur in the horizontal direction because the crystal is pinned to the substrate (otherwise we would see deformation or cracking of the crystal).

The intrinsic volume change of SU-8 crosslinking is only 7.5% [10], so there are other factors contributing the large shrinkage. The main origin of the shrinkage comes from the fact that crosslinking density, like the intensity distribution, is non-uniform. For an intensity profile that is thresholded to a binary polymer and air structure, the regions just above the threshold would have the lowest crosslinking density, while the highest intensity may not have reached the full crosslink dose (in other words, the contrast is not big enough). The material that is not polymerized enough may also leach out during development, causing shrinkage due to material loss. The low crosslinking density polymer can result in structural collapse due to low mechanical properties. In the photonic crystal fabrication process the shrinkage occurs when transferring the crystal from developer to isopropanol. The shrinkage also contributes for poor adhesion of the crystal to the substrate. A different negative photoresist system has been reported to have much lower shrinkage than SU-8 [11]. It has also been reported that a tight control over the monomer composition, eliminating the monomers that does not have eight functional groups (SU-10, SU-6, SU-4...etc) could significantly reduce shrinkage during multi-beam interference [12]. To completely eliminate shrinkage, however, positive tone photoresist or a much higher contrast intensity pattern should be used. Further discussion of the shrinkage issue and the use of positive photoresist can be found in chapters 4 and 5.

## **2.6 Conclusions and Future Directions**

Detailed fabrication processes of three dimensional SU-8 photonic crystals using four-beam interference lithography have been presented. Following this fabrication route, high quality 3D photonic crystals can be generated, as seen from the optical spectra presented in Chapter 3. Future directions include utilizing low shrinkage, high sensitivity photoresists and fabricate crystals with other beam geometries. Phase control for the beams has not been explored in this research but would be useful for more complex geometry generated by more than 5 beams.



## 2.7 References

- [1] J. H. Jang, C. K. Ullal, M. Maldovan, T. Gorishnyy, S. Kooi, C. Y. Koh, and E. L. Thomas, "3D micro- and nanostructures via interference lithography," *Advanced Functional Materials*, vol. 17, pp. 3027-3041, 2007.
- [2] F. Garcia-Santamaria, "Photonic Crystals Based on Silica Microspheres," in *Department of Materials Science*. vol. PhD Madrid, Spain: Universidad Autonoma de Madrid., 2003, p. Figure 4.8.
- [3] M. Campbell, D. N. Sharp, M. T. Harrison, R. G. Denning, and A. J. Turberfield, "Fabrication of photonic crystals for the visible spectrum by holographic lithography," *Nature*, vol. 404, pp. 53-56, 2000.
- [4] Y. V. Miklyaev, D. C. Meisel, A. Blanco, G. von Freymann, K. Busch, W. Koch, C. Enkrich, M. Deubel, and M. Wegener, "Three-dimensional face-centered-cubic photonic crystal templates by laser holography: fabrication, optical characterization, and band-structure calculations," *Applied Physics Letters*, vol. 82, pp. 1284-1286, 2003.
- [5] S. Yang, M. Megens, J. Aizenberg, P. Wiltzius, P. M. Chaikin, and W. B. Russel, "Creating periodic three-dimensional structures by multibeam interference of visible laser," *Chemistry of Materials*, vol. 14, p. 2831, 2002.
- [6] M. Degirmenci, A. Onen, Y. Yagci, and S. P. Pappas, "Photoinitiation of cationic polymerization by visible light activated titanocene in the presence of onium salts," *Polymer Bulletin*, vol. 46, pp. 443-449, 2001.
- [7] L. J. Wu, Y. C. Zhong, C. T. Chan, K. S. Wong, and G. P. Wang, "Fabrication of large area two- and three-dimensional polymer photonic crystals using single refracting prism holographic lithography," *Applied Physics Letters*, vol. 86, p. 241102, 2005.
- [8] X. Wang, J. F. Xu, H. M. Su, Z. H. Zeng, Y. L. Chen, H. Z. Wang, Y. K. Pang, and W. Y. Tam, "Three-dimensional photonic crystals fabricated by visible light holographic lithography," *Applied Physics Letters*, vol. 82, pp. 2212-2214, 2003.
- [9] O. Toader, T. Y. M. Chan, and S. John, "Photonic band gap architectures for holographic lithography," *Physical Review Letters*, vol. 92, 2004.
- [10] A. del Campo and C. Greiner, "SU-8: a photoresist for high-aspect-ratio and 3D submicron lithography," *Journal of Micromechanics and Microengineering*, vol. 17, pp. R81-R95, 2007.
- [11] A. Hayek, Y. G. Xu, T. Okada, S. Barlow, X. L. Zhu, J. H. Moon, S. R. Marder, and S. Yang, "Poly(glycidyl methacrylate)s with controlled molecular weights as low-shrinkage resins for 3D multibeam interference lithography," *Journal of Materials Chemistry*, vol. 18, pp. 3316-3318, 2008.
- [12] R. G. Denning, C. F. Blanford, H. Bharaj, D. Sharp, H. Urban, and A. Turberfield, "The Control of Shrinkage and Thermal Instability in SU-8 Photoresist Templates Fabricated by Holographic Lithography.," in *2009 MRS Spring Meeting San Francisco CA*, 2009.

## CHAPTER 3

### OPTICAL CHARACTERIZATION

\* Significant portions of this chapter are from “Holographically fabricated photonic crystals with large reflectance” Y. C. Chen, J. B. Geddes III, J. T. Lee, P. V. Braun, and P. Wiltzius *Applied Physics Letters* 91, 241103 (2007) [1]

#### 3.1 Introduction

Optical spectra measurement is the most common method to characterize photonic crystals. The transmittance or reflectance can be strongly modulated from the background by periodic variation of the crystal in their composition, periodicity and filling fraction. In this chapter, the fabricated holographic photonic crystals are characterized by optical spectroscopy, and the spectra are compared to simulation results using both finite difference time domain method (FDTD) and a simple one dimensional transfer matrix method (TMM) based on the theoretical structure constructed from optical measurements and scanning electron microscopy (SEM).

#### 3.2 Optical Spectra Measurement

The fabricated SU-8 photonic crystal is characterized by optical spectroscopy. The photonic crystal in discussion in this chapter is shown in Figure 3.1, and Figure 3.2 shows optical spectra taken from the fabricated crystal at normal incidence with a Fourier-transform infrared spectrometer coupled with an optical microscope. The reflectance measurement was normalized to a silver mirror and transmittance was normalized with air as 100%. The 70% peak in reflection and a transmission dip of 20% at 1.3  $\mu\text{m}$  generated by the internal periodicity, and the periodic oscillations are Fabry-Pérot fringes arising from interference between reflections from the film's interfaces. Transmittance plus reflectance is about 90% over the measured bandwidth. The lost 10% is due to the fact that not all the light is captured by the optics.

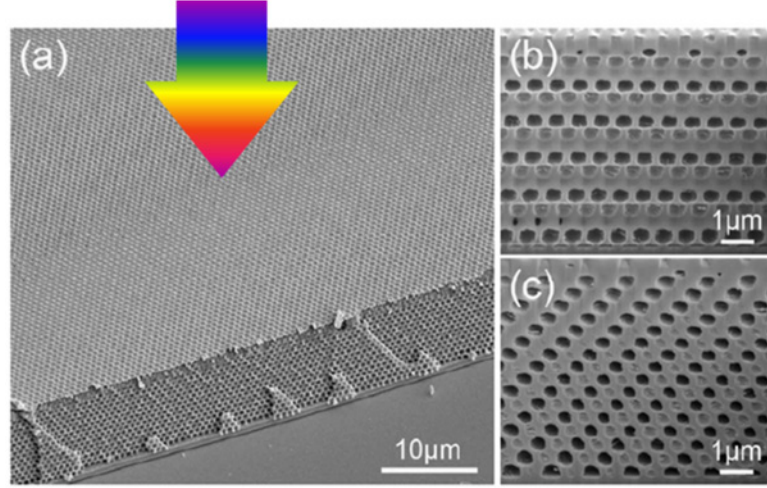


**Figure 3.1** (a) SEM of a holographically fabricated photonic crystal. Spectra is taken at the normal incidence (b)&(c) cross-sectional images obtained from focused ion beam milling. The viewing angle is  $52^\circ$  [1].

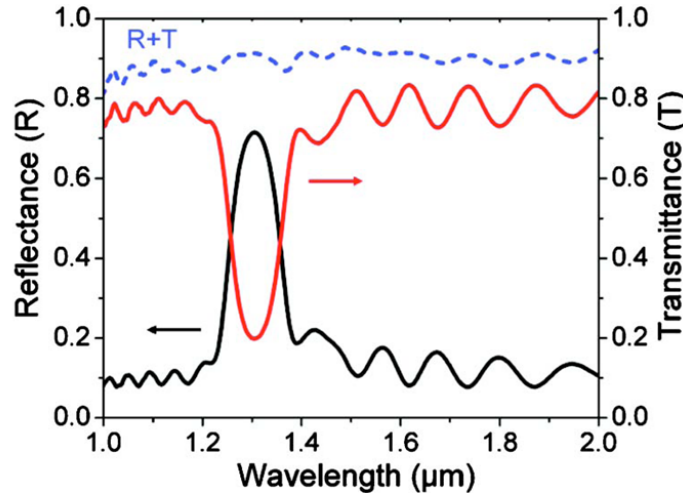


**Figure 3.2** Reflection and transmission spectra of the fabricated photonic crystal in the normal direction [1].

### 3.3 Model Structure Construction

To rationalize the experimental spectra, a model structure should be constructed with accurate measurements taken from the fabricated structures. The in-plane periodicity was first determined by diffraction patterns from the fabricated crystal using the same patterning wavelength (532 nm), as shown in Figure 3.3. The periodicity  $a$  is calculated to be 718 nm.

From this we know that the angle between the central beam and the side beams was  $58.78^\circ$  in air,

corresponding to  $32.15^\circ$  inside the unexposed photoresist with refractive index of 1.607 at 532 nm, as determined by spectroscopic ellipsometry.

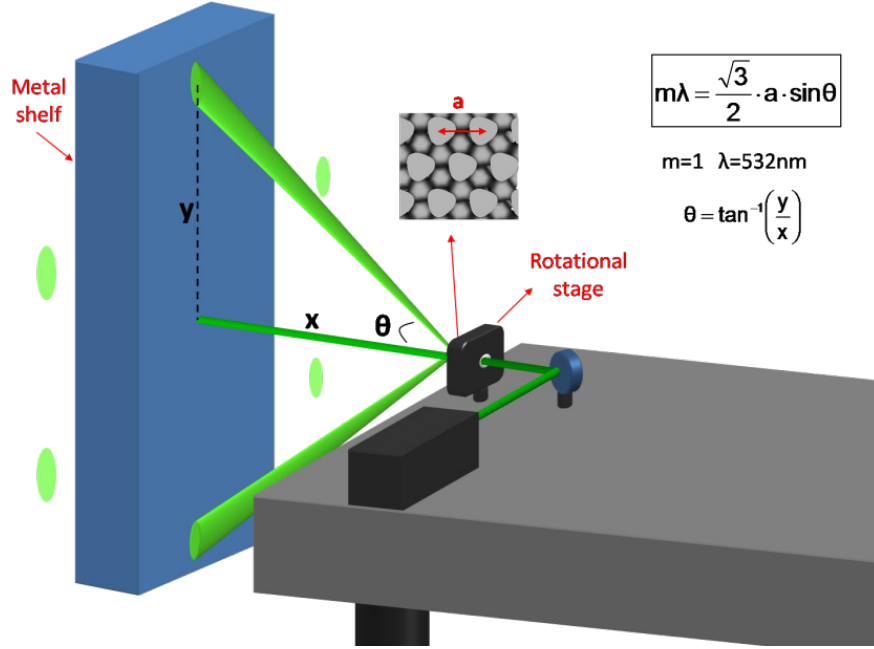


**Figure 3.3** Diffraction measurement setup for in-plane periodicity measurement.

The model structure is constructed following the process shown in Figure 3.4. First, the intensity distribution was calculated from the beam parameters. A 32% shrinkage perpendicular to the substrate resulting in a vertical spacing of 488 nm, as measured by SEM, was incorporated into the intensity profile by resampling the array along the  $[111]$  direction. This modified intensity profile served as a gradient for a binary threshold filter, the cutoff for which was determined by the polymer filling fraction, which in turn depended on the effective refractive index the structure. We found  $n_e$  to be 1.364 from the resonance orders of the Fabry-Pérot fringes which are proportional to wavenumber and film thickness. The relationship is

$$m = \frac{2n_e l}{\lambda_m}$$

where  $m$  is the resonance order,  $l$  is the film thickness, and  $\lambda_m$  is the peak wavelength of the  $m$ th-order fringe. From  $n_e$ , the filling fraction  $f$  of the polymer was computed from an effective medium relationship as

$$n_e = \sqrt{f n_p^2 + (1 - f) n_a^2}$$

where  $n_a=1$  and  $n_p=1.57$ , as obtained by measuring the Fabry-Pérot fringes between 1.1 and 2.1  $\mu\text{m}$  of a cross-linked SU-8 film of known thickness. With  $n_e=1.364$ ,  $f$  was determined to be 0.588 and the binary threshold for the modified intensity gradient was set to match the predicted filling fraction. Intensities greater than the threshold were taken to be polymer, and air filled the remainder.

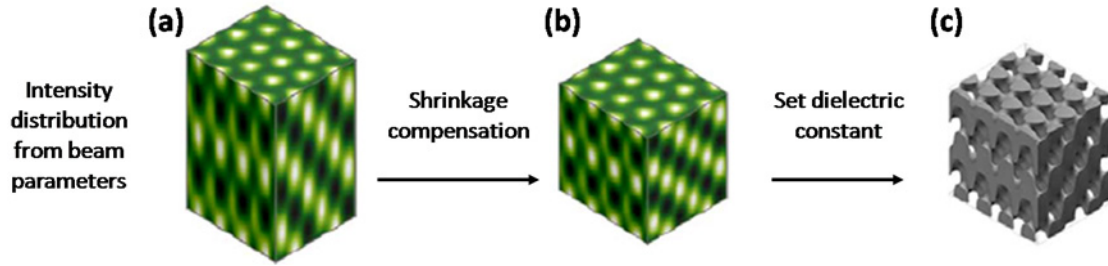


**Figure 3.4** Modeled structure constructed from intensity distribution assuming uniform shrinkage.

### 3.4 Spectra Simulation

For spectra simulation, the crystal geometry is constructed using the model to generate a structure with the correct thickness and number of layers. Both the adhesion layer and the glass substrate (half space) were considered in the simulation. Back reflection of the substrate could be corrected afterwards with the relation:

$$R' = \frac{\alpha + R(1 - 2\alpha)}{1 - \alpha}, \quad \alpha = \left( \frac{n_1 - n_2}{n_1 + n_2} \right)^2$$

where  $R'$  is the corrected reflectance, and  $n_1$  and  $n_2$  are the refractive indices that form the reflecting interface (in this case air and glass).

### 3.4.1 Finite Difference Time Domain (FDTD)

The reflectance and transmittance spectra were computed from the constructed structure using the FDTD method [2], as implemented in a freely available software package (MEEP) that uses subpixel smoothing algorithms to increase accuracy [3]. The theoretical structure was constructed in the software with a 24 nm pixel size resolution; an adhesion layer and a glass half-space substrate were included (Figure 3.5). Periodic boundary conditions were set for the horizontal direction. The calculated spectra were plotted as the solid line in Figure 3.7.

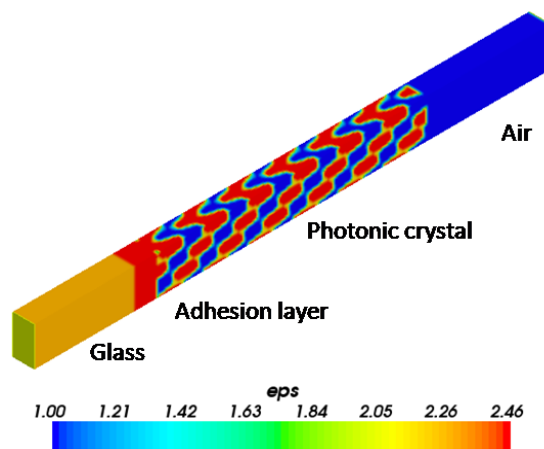


**Figure 3.5** Photonic crystal construction for FDTD spectra calculation.

### 3.4.2 Transfer Matrix Method

For a 3D structure with multiple layers and a unit cell of arbitrary shape, as common for holograms, FDTD requires considerable computational power. For this reason, a 1D transfer matrix method was also investigated for calculating the reflection and transmission spectra from the theoretical structure in the [111] direction [4]. The 3D structure was approximated as a stack of 10 nm thick homogeneous slices in the (111) planes, and the effective refractive index of each slice was calculated with effective medium relation from the filling fraction of polymer within the slice. Both the adhesion layer and the glass substrate halfspace were incorporated into the calculation. Figure 3.6 presents the periodic variation of filling fraction with depth, which results in a periodic variation of effective refractive index. The reflection and transmission spectra were

computed from the thicknesses and refractive indexes of the slices using a common transfer matrix formalism [4-7]. The result is presented as the dotted line in Figure 3.7. It closely matches the FDTD result, indicating that the 1D transfer matrix method is a valid approximation. Moreover, the transfer matrix computation takes minutes to complete while the FDTD computation can takes days.

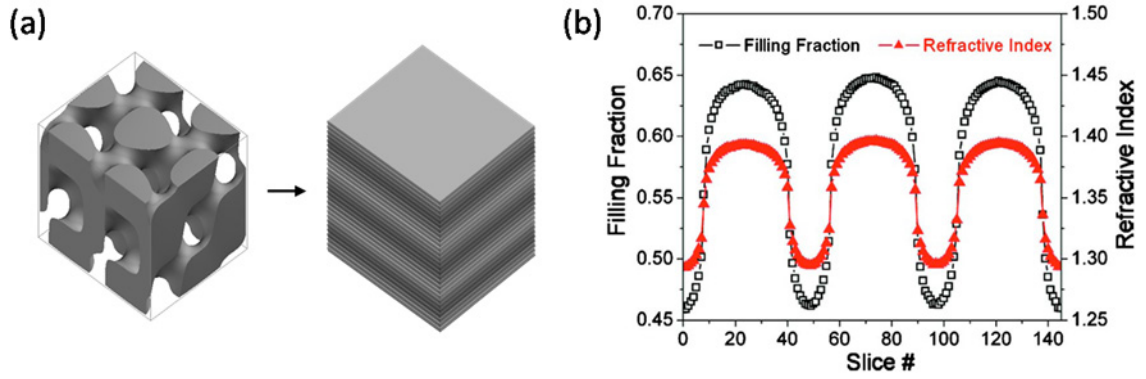


**Figure 3.6** (a) The theoretical 3D structure is approximated as a stack of layers (b) The filling fraction of each layer determines its effective refractive index [1].

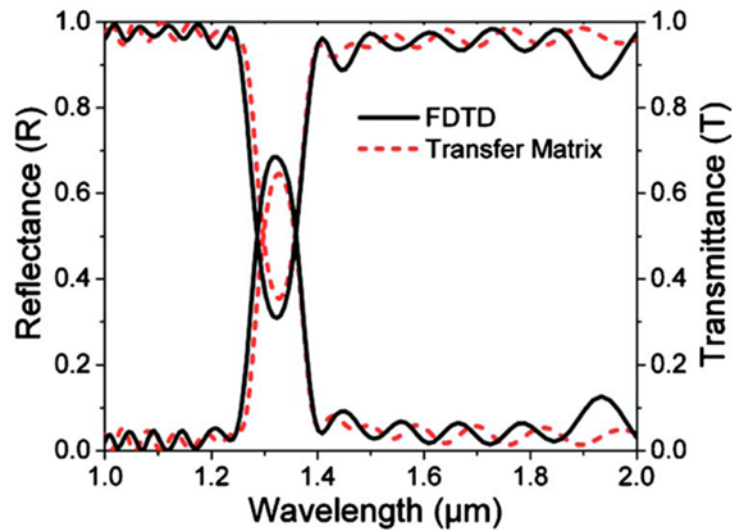


**Figure 3.7** Spectra simulation result from the transfer matrix method (dotted) and FDTD (solid) [1].

### 3.5 Calculation Compare to Measurement

The measured reflectance spectrum was compared with calculated spectra in Figure 3.8. The calculated spectra were corrected for their back reflection. It can be seen that the experimental and calculated spectra match quite well in both peak position and magnitude. The position of the main peak in the experimental spectra is only 2.5% different than the calculated spectra, within the 5% error of film thickness measurement by SEM. It should be noted that the experimental main peak was not used for constructing the theoretical structure. Slight broadening of the experimental peak indicates some variation from perfect periodicity in the structure, which can be expected from any fabrication method. The experimental spectrum has a higher background reflectance because of the slight dispersion and absorption of the objective optics causing variations in the reference measurement. The issue can be fixed by using  $\text{CaF}_2$  objectives, which is a much better optical material in the IR range.

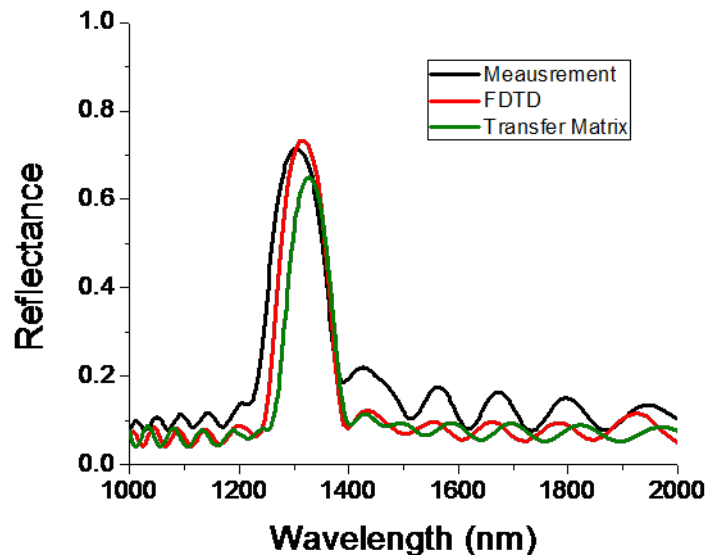


**Figure 3.8** Calculated normal incidence reflectance spectra compared with measurement.

The same spectra simulation procedure has also been used for other photonic crystal structures. Figure 3.9 shows the case with a SU-8 crystal fabricated by two photon phase mask



lithography by Daniel Shir in the Rogers group at the University of Illinois. Simulated spectra also showed excellent agreement for transmittance and reflectance.

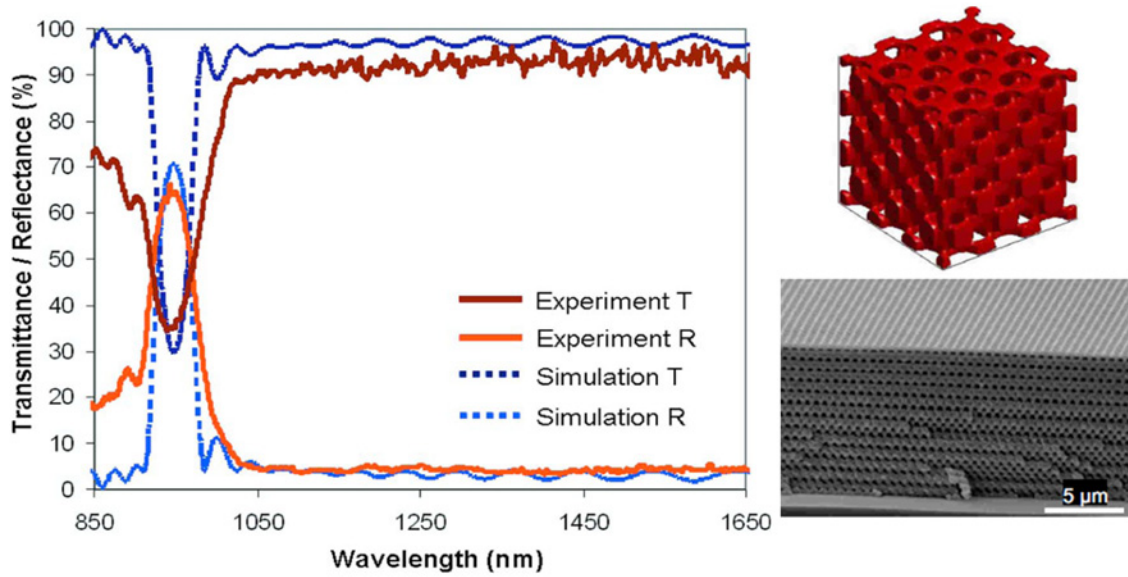


**Figure 3.9** Optical spectra measurement and simulation compare of SU8 photonic crystal fabricated with phase mask two photon lithography [8].

### 3.6 Experimental

A continuous-wave, frequency-doubled Nd:YVO<sub>4</sub> laser (532 nm) was used for holographic exposure. The laser beam was split into four parts of equal intensity and arranged in an “umbrella” geometry [9]. The angle between the central beam and the side beams was 58.78° in air, corresponding to 32.15° inside the unexposed photoresist with refractive index of 1.607 at 532 nm, as determined by spectroscopic ellipsometry. The central beam was circularly polarized, and the side beams were linearly polarized in their incident planes [10]. The photoresist had a 0.3 wt % solid content of photoinitiator benzenecyclopentadienyliron(II) hexafluorophosphate (Aldrich) and the remainder SU-8 monomer. It was spin coated onto a glass substrate which previously had been coated with a 0.75 μm cured SU8 layer for adhesion promotion. The film was exposed with a 60–90 J/cm<sup>2</sup> (2–3 s) dose over a spot size of 4 mm. After exposure, it was

postbaked at 85 °C for 25 min in dry air then developed in propylene glycol methyl ether acetate for 2 hours followed by rinsing in isopropanol and super critically drying with CO<sub>2</sub>.

The developed structure has fcc-like symmetry with the (111) plane parallel to the substrate.

Figure 1(a) presents a cleaved cross section and in Figure 1(b) and 1(c) cross sections were exposed using focused ion beam milling (FIB). To prevent polymer deformation during ion milling, the sample was coated with a 2 nm layer of Al<sub>2</sub>O<sub>3</sub> by atomic layer deposition which serves as a structural support. Two photon phase mask lithography experimental can be found in reference [8].

### 3.7 Conclusions and Future Directions

Optical spectroscopy was performed on fabricated photonic crystals. Spectra simulations using a model structure closely related to experimental result show excellent agreement with the measurement, demonstrating the high quality of the fabricated crystal. One dimensional transfer matrix method shows good agreement with the FDTD simulation result in this system, offering a route to significantly reduce computation requirements. In the future, the transfer matrix method can be expanded to 3D, which would be more suitable for crystals with high refractive index contrast or for analyzing high energy region of the spectra. The fabricated crystals also show distinct high energy peaks which are consistent across different samples (Figure 3.8). It would be interesting to analyze these peaks in addition to the first order peak presented in this chapter to further characterize the fabricated photonic crystals. Full angle characterization for the 3D crystal is also worth examining in the future.

### 3.8 References

- [1] Y. C. Chen, J. B. Geddes, J. T. Lee, P. V. Braun, and P. Wiltzius, "Holographically fabricated photonic crystals with large reflectance," *Applied Physics Letters*, vol. 91, p. 241103, 2007.

- [2] A. Taflove and S. C. Hagness, *Computational Electrodynamics: The Finite-Difference Time-Domain Method*, 3rd ed., 3 ed. Norwood, MA: Artech House, 2005.
- [3] A. Farjadpour, D. Roundy, A. Rodriguez, M. Ibanescu, P. Bermel, J. D. Joannopoulos, S. G. Johnson, and G. W. Burr, "Improving accuracy by subpixel smoothing in the finite-difference time domain," *Optics Letters*, vol. 31, pp. 2972-2974, 2006.
- [4] Y. Ono, "Transmittance analysis of three-dimensional photonic crystals by the effective medium theory," *Applied Optics*, vol. 45, pp. 131-136, 2006.
- [5] J. Lekner, "Light in periodically stratified media " *Journal of the Optical Society of America a-Optics Image Science and Vision*, vol. 11, pp. 2892-2899, 1994.
- [6] A. Yariv and P. Yeh, "Electromagnetic propagation in periodic stratified media. 1. Birefringence, phase matching, and x-ray lasers " *Journal of the Optical Society of America*, vol. 67, pp. 438-448, 1977.
- [7] P. Yeh, A. Yariv, and C. S. Hong, "Electromagnetic propagation in periodic stratified media. 1. General theory " *Journal of the Optical Society of America*, vol. 67, pp. 423-438, 1977.
- [8] D. Shir, E. C. Nelson, Y. C. Chen, A. Brzezinski, H. Liao, P. V. Braun, P. Wiltzius, K. H. A. Bogart, and J. A. Rogers, "Three dimensional silicon photonic crystals fabricated by two photon phase mask lithography," *Applied Physics Letters*, vol. 94, 2009.
- [9] M. Campbell, D. N. Sharp, M. T. Harrison, R. G. Denning, and A. J. Turberfield, "Fabrication of photonic crystals for the visible spectrum by holographic lithography," *Nature*, vol. 404, pp. 53-56, 2000.
- [10] Y. V. Miklyaev, D. C. Meisel, A. Blanco, G. von Freymann, K. Busch, W. Koch, C. Enkrich, M. Deubel, and M. Wegener, "Three-dimensional face-centered-cubic photonic crystal templates by laser holography: fabrication, optical characterization, and band-structure calculations," *Applied Physics Letters*, vol. 82, pp. 1284-1286, 2003.

## CHAPTER 4

### X-RAY COMPUTED TOMOGRAPHY FOR 3D IMAGING

#### 4.1 Introduction

Interference lithography differs from other 3D photonic crystal fabrication methods in that both the geometry and basis of periodic unit are highly tunable, which allows the flexible control of these variables for tuning optical properties [1]. Most theoretical proposed structures assume the basis follows the iso-intensity surface [2, 3]. However practical issues such as shrinkage, photoresist resolution and absorption-generated intensity gradients can invalidate this assumption [4, 5]. Full modeling of the fabrication process has been reported [4], however without appropriate means to inspect the actual fabricated structures on the micro-scale, it is difficult to obtain the necessary information to implement or modify the model. Most comparisons of the fabricated and theoretical structures are limited to scanning electron microscopy (SEM), which can only provide snapshots of two-dimensional information. In other research fields, focused ion beam (FIB) techniques have been applied for 3D reconstruction [6]. However in our attempts, despite the careful and tedious FIB process, the crystals have undergone slight distortion during the ion milling, which could lead to significant error in the 3D reconstruction.

X-ray microscopy is an imaging technique used primarily in the medical field. Recent advancement of the technique has opened up new opportunities in other disciplines, particularly biological and materials science [7-10]. As an imaging light source, X-rays have a short wavelength enabling high resolution and do not interact with matter as strongly as charged particles. Unlike electron microscopy, metal coating and vacuum compatibility are not required for sample preparation. For hard x-ray microscopy, due to the large penetration depth, angular resolved images can be reconstructed to full 3D images through computed tomography (CT) [11]. This is especially useful for nondestructive imaging of the interiors of optically opaque objects.

The resolution of hard x-ray microscopy has been reported to be 40nm and will continue to improve with advances in x-ray optics [12].

In this chapter, we report the 3D imaging of multibeam interference generated SU-8 photonic crystals using a hard x-ray CT with a lab-based microscope system in both with phase contrast and absorption contrast modes. The reconstructed cells were used to calculate reflectance spectra with a finite difference time domain (FDTD) method. This is compared to the experimentally measured spectra and the spectra calculated from a modeled structure assuming threshold intensity and uniform shrinkage. The geometry of the reconstructed crystal is then compared with the uniform shrinkage model to assess the quality of the structure and validity of the model.

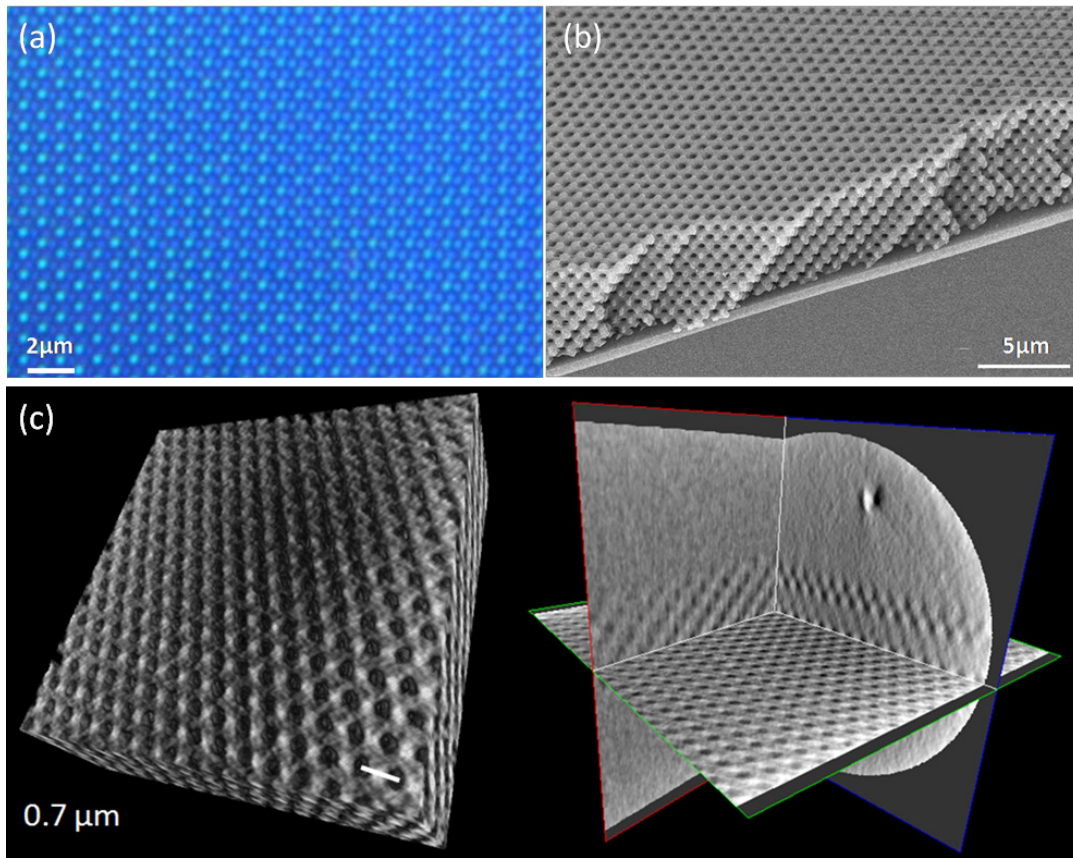


**Figure 4.1** Imaging of 3D holographic photonic crystals (a) Optical transmission microscopy (b) Electron microscopy (c) X-ray CT microscopy

## 4.2 Sample Preparation

### 4.2.1 *SU-8 Photonic Crystal Fabrication*

The photoresist was formulated with chemicals listed in Table 2.1(b). The solvent and photoacid generator are mixed first for 1 hour before SU-8 2025 is added, and the solution is then stirred overnight.

The substrate is number two cover glass, cleaned with soap and water, followed by acetone and isopropanol, and then dried with nitrogen. A fully crosslinked SU-8 layer was made on the substrate, which serves as an adhesion layer and HF etch stop for later steps. This layer was made by spin coating SU-8 2002 on the substrate at 1000rpm for 60 seconds, prebaking at 65°C and 95°C for 10 minutes each, exposure under a UV lamp (long wave) for 20 minutes and a 20 minute postbake at 95°C.

The formulated resist was spin-coated onto the adhesion layer at 500 rpm for 5 seconds with an acceleration of 100rpm/second, then at 2000 rpm for 30 s with acceleration of 300 rpm/second (Microchem suggested procedure). The spin-coated film was pre-baked on the hotplate at 65°C for 10 minutes and 95°C for 25 minutes. After the film was cooled for 10 minutes, it was exposed to the 532 nm multibeam interference setup (Coherent, Verdi V5) for 0.5 seconds with a laser power setting at of 5.4 W. The four-beam umbrella configuration has a side to central beam intensity ratio of 1 to 3.7 and an intercept angle of 43.7° in air, corresponding to 25.6° in the photoresist. Post-bake was performed at 80°C for 20 minutes in dry air at 1 atm in a vacuum oven. The sample was then immersed in propylene glycol methyl ether acetate for one hour, and afterwards transferred to isopropanol for 10 minutes. Critical point drying was then performed to minimize drying surface tension (Tourisimis, Samdri 790).

### 4.2.2 *Atomic Layer Deposition of Hafnium Dioxide*

Atomic layer deposition (ALD) (Cambridge Nanotech) was performed on the SU-8 template with the parameters listed in Table 4.1. The template was first coated with ~10 nm alumina, then ~163

nm hafnium dioxide. The purpose of the aluminum oxide is to protect the template from heat deformation during the coating of hafnium dioxide at 125°C. In ALD process, the precursors are released in alternating pulses, held in the chamber for exposure (if necessary), and pumped away in order to form one atomic layer at a time. The created structures are amorphous.

(a) Aluminum oxide ALD parameters

Precursor	Pulse (sec)	Exposure (s)	Pump (s)
H <sub>2</sub> O (DI)	0.03	2	65
trimethylaluminum	0.03	2	65

Temperature: 85°C Nitrogen flow:20 sccm

(b) Hafnium dioxide ALD parameters

Precursor	Pulse (sec)	Exposure (s)	Pump (s)
H <sub>2</sub> O (DI)	0.06	0	125
Tetrakis(dimethylamido)Hafnium(IV)	0.6	0	75

Temperature: 125°C Nitrogen flow:20 sccm

**Table 4.1** Atomic layer deposition condition for (a) Al<sub>2</sub>O<sub>3</sub> (b) HfO<sub>2</sub>.

#### 4.2.3 Etching Substrate

The substrate of the crystal is removed with procedures illustrated in Figure 4.2. A plastic tube (Tygon) is attached to the back of the substrate with 5-minute-epoxy glue, leaving a ~1.5 mm opening which is aligned with the crystal position. HF solution (10% HF, 10% H<sub>2</sub>O, 80% IPA) is filled in the tube. After etching for ~1day, during which the solution is changed twice, the #2 cover glass is etched through (the adhesion layer acts as HF etch stop). The tube can then removed by squeezing from its side, and the epoxy glue can be cleaned off using razor blade. There may be some residuals of the non silica components of the glass deposited on the film. This etching leaves a free standing film mounted over a hole in the cover glass.

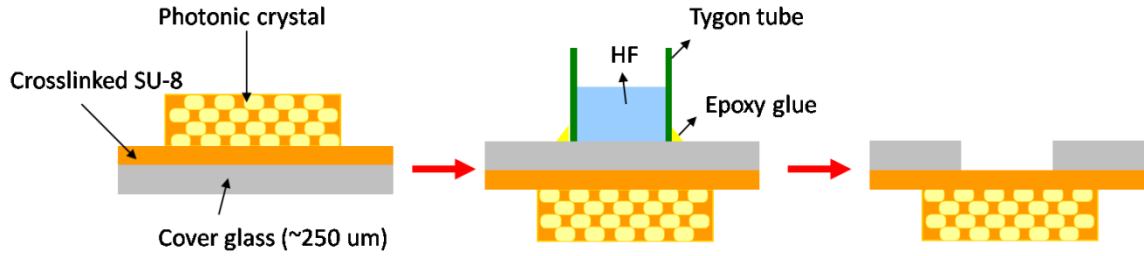


**Figure 4.2** Procedure for etching glass substrate for x-ray microscopy.

#### 4.2.4 Pre-alignment

The mounted film can be scanned from  $-70^\circ$  to  $70^\circ$ , which is enough for identify the crystal features. For full a  $180^\circ$  scan, the film was broken off and a piece of the crystal from the center was glued to a tip sample mount with epoxy. The region of interest was determined using the pre-alignment microscope (Figure 4.2) and a few gold particles were place onto the sample for registration (with a single horse hair). The region of interest was chosen near the corner of the piece, and the nearby gold particle was placed approximately in the middle of the field of view, so that during rotation imaging, the gold particle reference would be in the field of view for all angle projections.

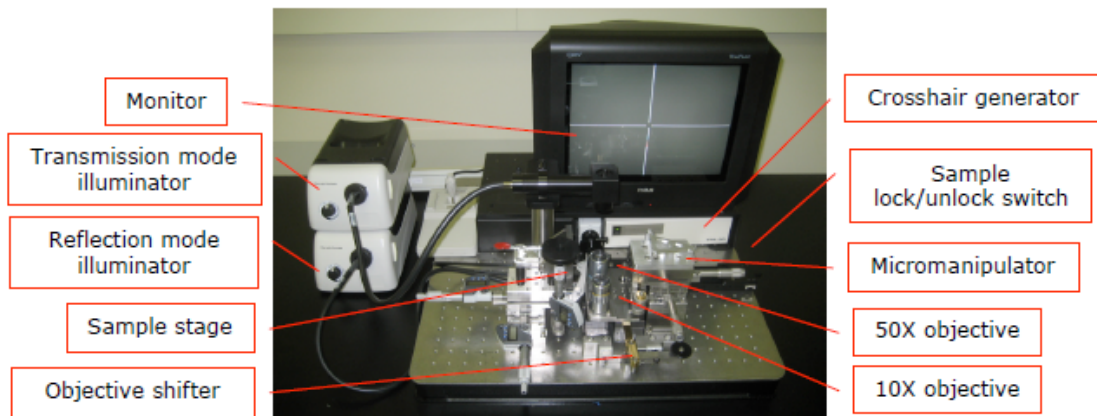


**Figure 4.3** Pre-alignment microscope [13].



### 4.3 Phase Contrast Imaging

For materials composed of low atomic number elements such as polymer and biological samples, phase contrast imaging can provide higher contrast than absorption contrast by as much as three orders of magnitude; especially in the hard x-ray energy range (see Chapter 1.3.4). X-ray phase contrast 3D imaging of the fabricated SU-8 crystal was performed by Xradia Inc. The imaged crystal was 8 microns thick; with a relatively high filling fraction (greater than 60% polymer). Part of the sample's substrate was etched through to the bottom of the crystal to ensure that the contrast comes solely from the crystal. The etched window was around 1.5 mm, large enough to allow imaging from  $-70^\circ$  to  $+70^\circ$ , but small enough to provide mechanical stability and prevent polymer from sagging during HF etching of the substrate. The sample was secured on the rotating sample mount as shown in the picture.

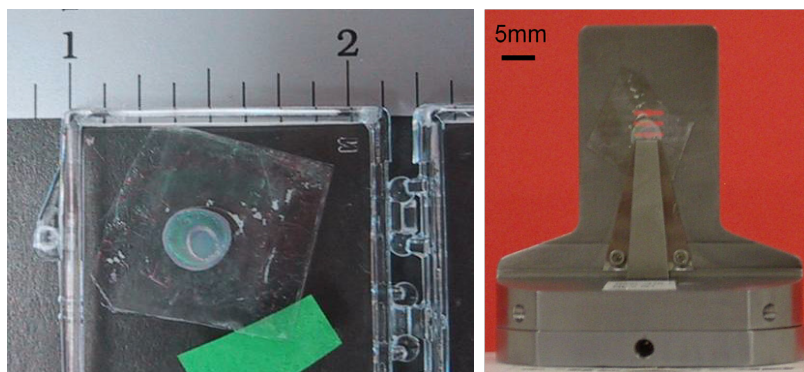


**Figure 4.4** SU-8 photonic crystal with substrate etched for phase contrast imaging.

Phase contrast imaging was conducted using a 8 keV (0.15 nm) Cu rotating anode source. The microscope setup can be seen in Figure 1.3.10 (Chapter 1). Transmission images were taken from  $-70^\circ$  to  $+70^\circ$  with  $0.25^\circ$  intervals. Total imaging time was 62 hours for all 561 images, so mechanical stability of the system is very important. The 3D crystal images reconstructed from the transmission images by computed tomography are shown in Figure 4.1(c) and Figure 4.5. According to Xradia Inc, the resolution of the system is 50x50x80 nm. The regular periodic

pattern of the crystals can be clearly seen with the bright and dark regions in all three dimensions. White means more absorption and black means less absorption in the gray scale spectrum. Due to the nature of phase contrast imaging, however, the gray scale of the density does not directly correspond to any physical quantity such as electron density of the materials. From the images we can observe the “halo” artifacts that cause the intense white spots, which is typical for phase contrast imaging for this microscope system. Features along the vertical direction are less defined than those in the planar direction. This is because the images were not gathered with a full 180° scan, which is required for accurate CT reconstruction.

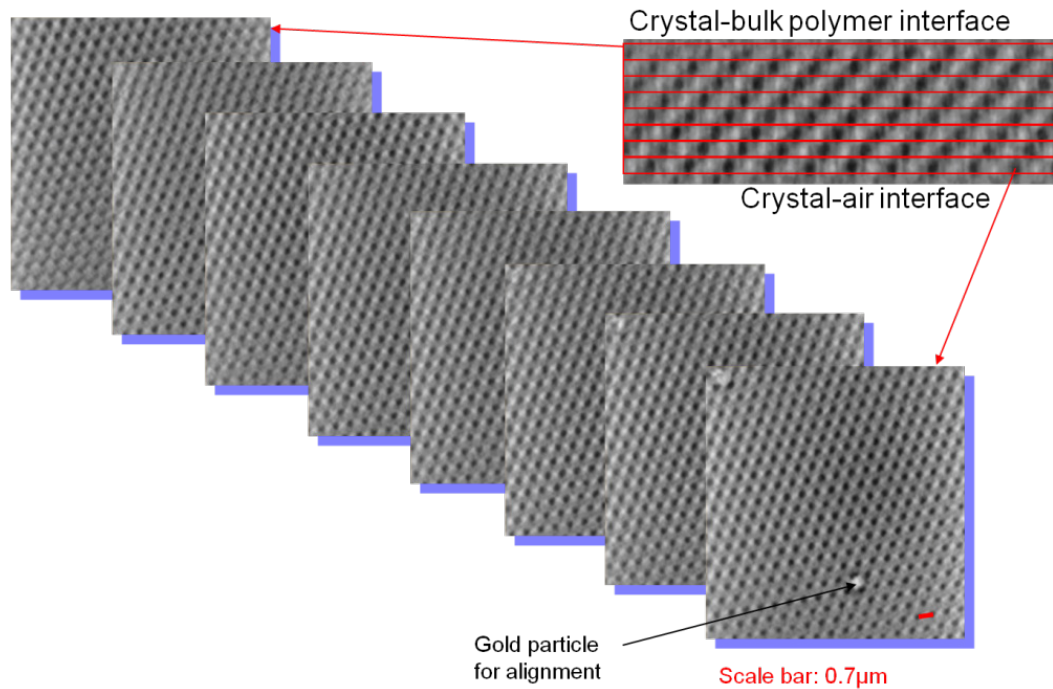


**Figure 4.5** Cross-sectional slices of the CT reconstructed photonic crystal.

As with the nanoXCT system, phase contrast imaging is excellent for qualitative measurement of the photonic crystal with low electron density such as polymer or biological samples. However it is not suitable for quantitative measurement due to the artifacts caused by

non-collimated light source. It is also not possible to perform holotomography due to the fixed optics positions. For more quantitative measurement, absorption contrast is a better choice.

#### 4.4 Absorption Contrast Imaging

The photonic crystals of interest are composed of SU-8 and air. SU-8 is an organic chemical comprised of carbon, oxygen and hydrogen, and air is composed of primarily nitrogen and oxygen. All of these are light elements and do not absorb hard x-rays well. Table 4.2 lists various materials with their transmission values obtained from reference [14]. Elements with higher atomic numbers and higher density absorb x-rays much more effectively.

Materials	Density (g/cm <sup>3</sup> )	Transmission (5μm)
Air	1.225x10 <sup>-3</sup>	1
SU-8	1.19	0.9968
Al <sub>2</sub> O <sub>3</sub>	3.97	0.9411
HfO <sub>2</sub>	13.31	0.4074
RuO <sub>4</sub>	12.41	0.5069
OsO <sub>4</sub>	22.57	0.2127
Si	2.33	0.9307
Cu <sub>2</sub> O	8.96	0.8120
TiO <sub>2</sub>	4.26	0.7599
Au	19.32	0.1339
Ni	8.902	0.8092

**Table 4.2** Transmission values of various materials with 5μm thickness at 8 keV. Values calculated using reference [14].

##### 4.4.1 Contrast Enhancement through Staining

We attempted to use osmium tetroxide and ruthenium tetroxide to stain the polymeric photonic crystal. OsO<sub>4</sub> and RuO<sub>4</sub> have long been used as staining agents for polymer and biological samples to increase contrast for optical and electron microscopy [15-17]. The high atomic number of osmium (76) and ruthenium (44) provides high absorption of x-rays, making them useful for improving contrast in x-ray microscopy as well. Both OsO<sub>4</sub> and RuO<sub>4</sub> are volatile

solids at room temperature, they readily oxidize polymers to a lower oxidation state, which often appears dark. Osmium tetroxide is the more common staining agent of the two; however it is only effective with unsaturated polymers. Ruthenium tetroxide is a stronger oxidizing agent than osmium tetroxide and has ability to stain both unsaturated and saturated polymers, as well as some functional groups that cannot be stained by  $\text{OsO}_4$ .

Both  $\text{OsO}_4$  and  $\text{RuO}_4$  are applied in aqueous solution with concentrations lower than 1 wt%. Small amounts of the staining solution were put in a jar sealed with a cap, and the sample was attached to the inside of the cap to be stained with vapor. For both  $\text{OsO}_4$  and  $\text{RuO}_4$ , several staining conditions were varied, including time, concentration and temperature. The staining results were then examined by SEM without additional metal coating. For  $\text{OsO}_4$ , we found that the crystal was either badly deformed, or was not stained enough to remove the SEM charging effect. It also took several days to completely stain the polymer by this method.  $\text{RuO}_4$  stained the SU-8 much more quickly. However it appears that successful staining is always accompanied by some degree of swelling, which is not acceptable for imaging the original polymer template. Figure 4.6 shows the SEM micrograph of the staining results. Swelling of polymers during staining has been observed and reported previously [18]. By changing the staining condition the swelling may be reduced. However because we do not have the exact specifications of the original geometry to compare against, it is difficult to determine the magnitude and any reduction of the swelling effect.

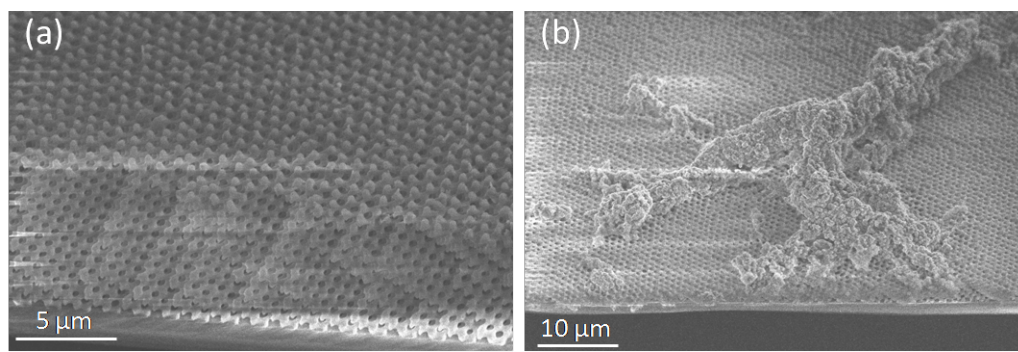


**Figure 4.6** SEM images of  $\text{OsO}_4$  stained SU-8 photonic crystal.

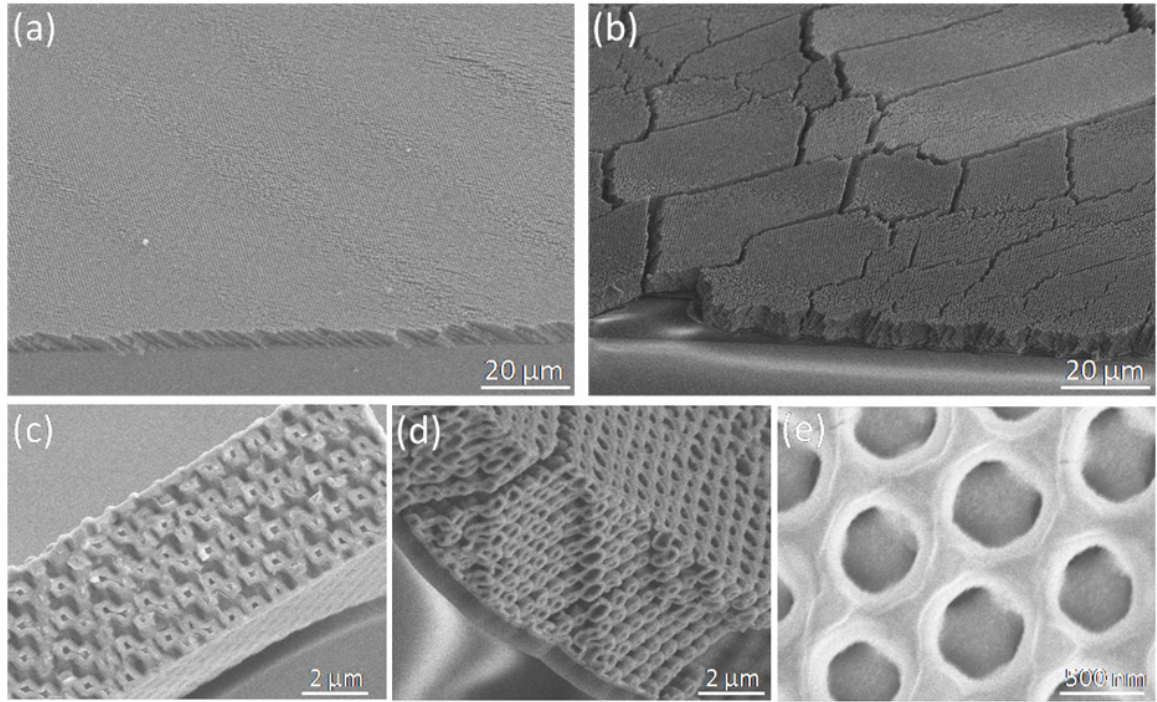


**Figure 4.7** SEM images of  $\text{RuO}_4$  stained SU-8 photonic crystal (a) unstained SU8 crystal (b) stained with  $\text{RuO}_4$  with same magnification (c)-(e) various images of stained crystals.

We also attempted to use salts, such as potassium iodide and sodium polytungstate, to infiltrate the crystal to enhance absorption. Our approach was to mix the salt with a water-soluble polymer to prevent the salt from forming large crystals and phase-separating into the interstitial spacing of the lattices. However, the salt does not dissolve more than 10% into the polymer (PEO, PEG), and when dried and cooled, the salt still tends to crystallize and precipitate.

It is worth considering electrodeposition of heavier materials to enhance the contrast. The complete infiltration of holographic photonic crystals has been demonstrated in our group by Masao Miyake ( $\text{Cu}_2\text{O}$  and Ni) [19] and in literature ( $\text{TiO}_2$ ) [20]. For the purpose of observing template geometry however, we will first need to verify that the crystals do not experience distortion during these deposition processes.

#### 4.4.2 Infiltration of $\text{HfO}_2$ by ALD

Atomic layer deposition (ALD) has been shown as a reliable infiltration technique for SU-8 photonic crystals [21]. Using this technique, an oxide layer can be deposited at close to one angstrom per cycle conformally across the polymer surface. We selected hafnium dioxide as our infiltration material. Hafnium has a high atomic number (72) and the deposition technique is well developed, being used in semiconductor industry as high-K dielectric barrier, and the process can be done at relatively low temperatures (125°C in our case).

To prepare the SU8 photonic crystal for infiltration of  $\text{HfO}_2$ , it is first coated with 10nm  $\text{Al}_2\text{O}_3$  by ALD at 80°C in order to prevent crystal distortion under the higher reaction temperatures of  $\text{HfO}_2$  (125°C). The main reflectance peak position was monitored periodically during the infiltration process. No obvious peak shifts were observed after  $\text{Al}_2\text{O}_3$  deposition, indicating minimal distortion occurred during that conformal coating. When  $\text{HfO}_2$  was deposited by ALD, the first order reflectance peak red-shifted due to the significant increase in the refractive index. This indicates successful infiltration into the three dimensional crystal (Figure 4.8). A total thickness of 163 nm  $\text{HfO}_2$  (measured by ellipsometry) was deposited. Figure 4.9 shows focus ion beam milling images demonstrating the infiltration result.

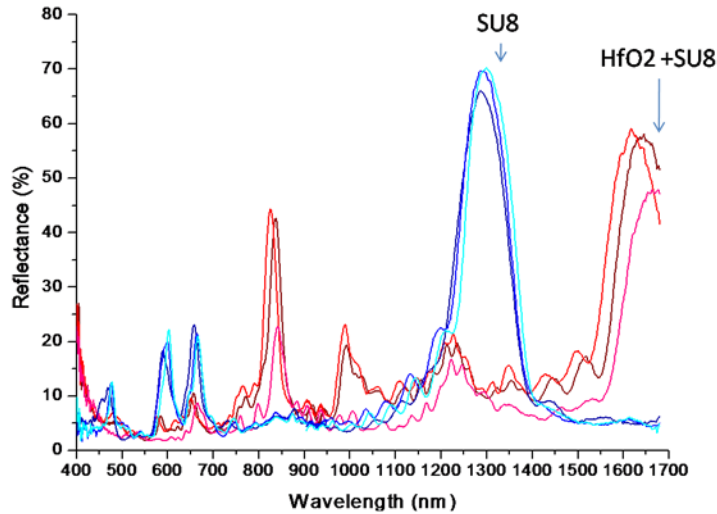


**Figure 4.8** Reflectance spectra of an SU-8 photonic crystal before and after  $\text{HfO}_2$  infiltration by ALD. The different colors represent measurements taken at different spots of the same sample. The detector limit was 1700nm.



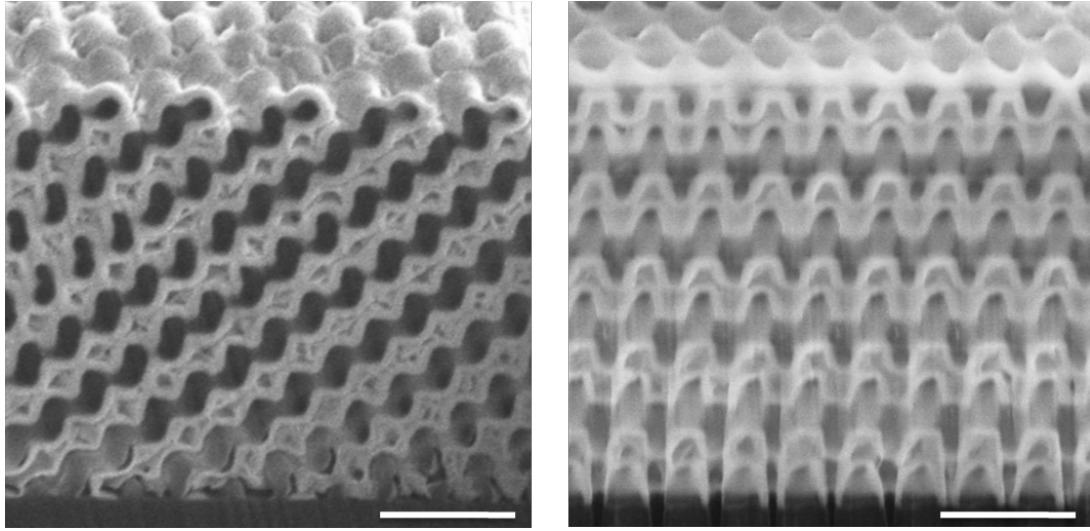


**Figure 4.9** Focused Ion beam cross sectional image of the HfO<sub>2</sub> filled photonic crystal. The scale bars are 2  $\mu\text{m}$ .

#### 4.4.3 X-ray NanoCT Imaging

The transmission images are taken at 0.5° intervals through 180° (361 images in total). Each image takes about 5 minutes to obtain. Selected images are shown in Figure 4.10 with different angle projections. Varying periodic patterns can be seen at different angles. At 0°, the hexagonal patterns correspond to the ABC stacking of FCC lattice in the 111 plane -- the hexagonal periodicity is measured  $a/\sqrt{3}$  (510 nm), where  $a$  is the hexagonal periodicity of the top view of the 111 plane feature (884 nm). At 90° cross-section, we can clearly see the crystal has 14 layers, and the A-B-C stacking can also be identified. The three circular black features are gold particles used for alignment. There was one defect, caused either by dust or bubbles, in the field of view close to the corner, which can be clearly seen in the 0° image.

The image contrast is generated by both the thickness of the crystal and the thickness of the HfO<sub>2</sub> coating. If the crystal was too thin, there would not be enough contrast for the vertical images. If the thickness of HfO<sub>2</sub> was too small, the film would not absorb enough x-ray to highlight the original polymer-air boundary. In our earlier imaging attempt, we were using crystals with 8 layers and a 60 nm HfO<sub>2</sub> coating which yielded a much lower contrast.

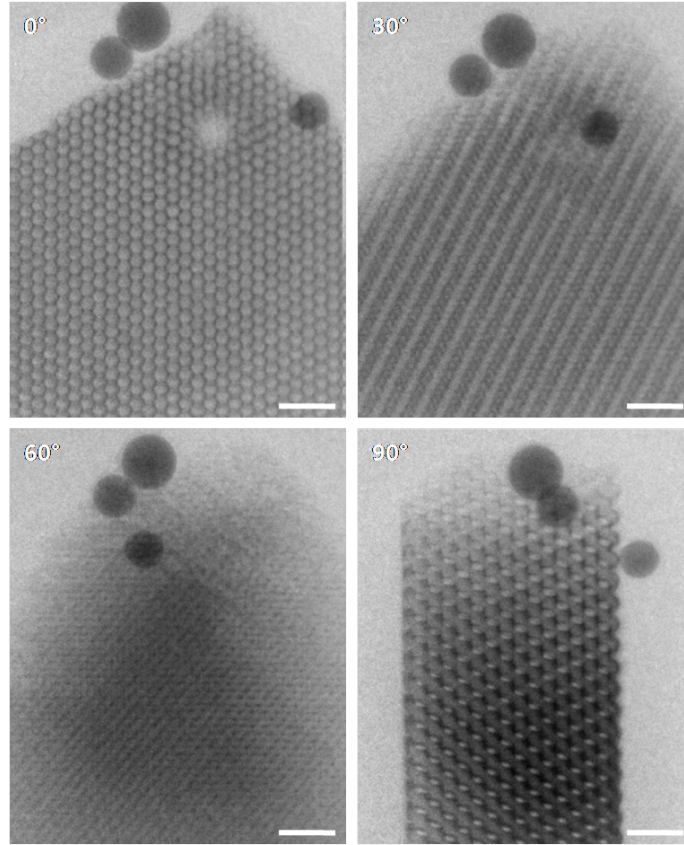


**Figure 4.10** X-ray transmission micrographs of  $\text{HfO}_2$  coated SU-8 photonic crystal. The scale bar is 2  $\mu\text{m}$ .

The transmission images are transformed to absorption images and reconstructed through computed tomography that is built into the nanoXCT software. The reconstructions are shown in Figure 4.11 and Figure 4.12. In the images, brighter regions indicate more absorption and  $\text{HfO}_2$  shells can be clearly observed. There are three regions imaged: air, polymer and hafnium dioxide. However because of the low absorption of both air and polymer to x-ray, the reconstructed image only shows the  $\text{HfO}_2$  shell (bright color). Although both air and polymer appear dark, it is easy to discern the two materials because the polymer phase is outlined by  $\text{HfO}_2$  and the two phases are bicontinuous. The 3D cell was then binarized, separating the polymer region from the hafnium dioxide and air (Figure 4.12 (c)&(d)) using a software program called Amira. This software also allows us to produce arbitrary slices through the real space fabricated structure, in a much more



flexible and non-destructive manner than the FIB method. The progression of the slices through the structure with angle can be observed, as shown in Figure 4.13

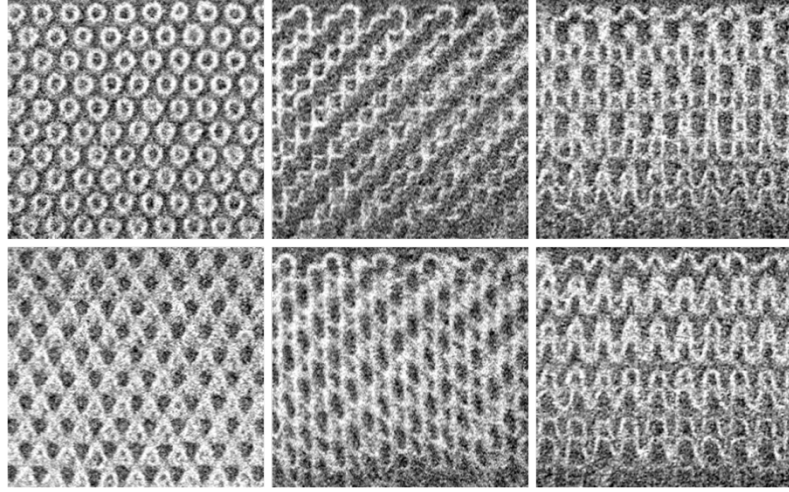


**Figure 4.11** Computed tomographic absorption cross-sectional images of  $\text{HfO}_2$ -SU-8 photonic crystal.

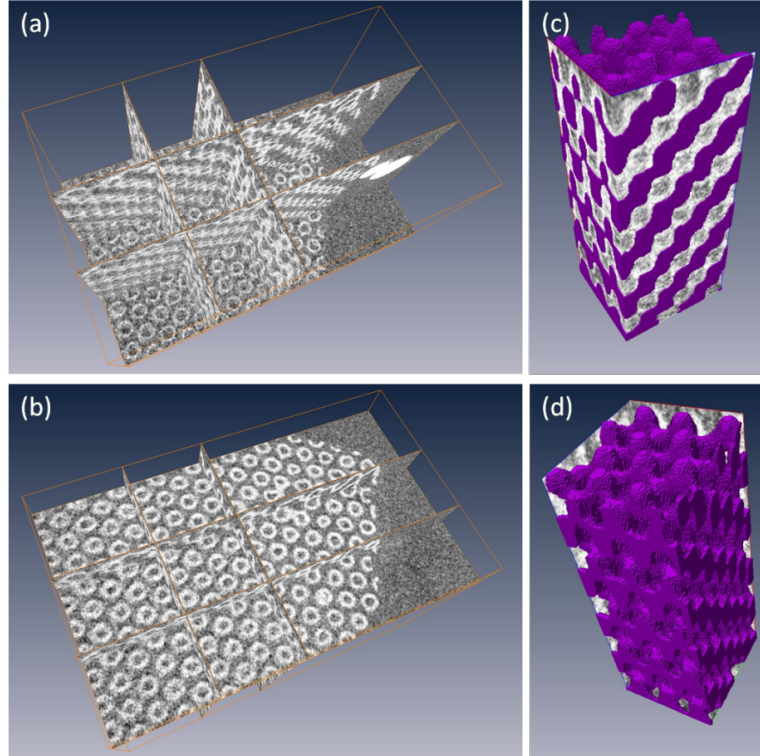


**Figure 4.12** (a)&(b) Selected region for binarization (c)&(d) polymer regions.

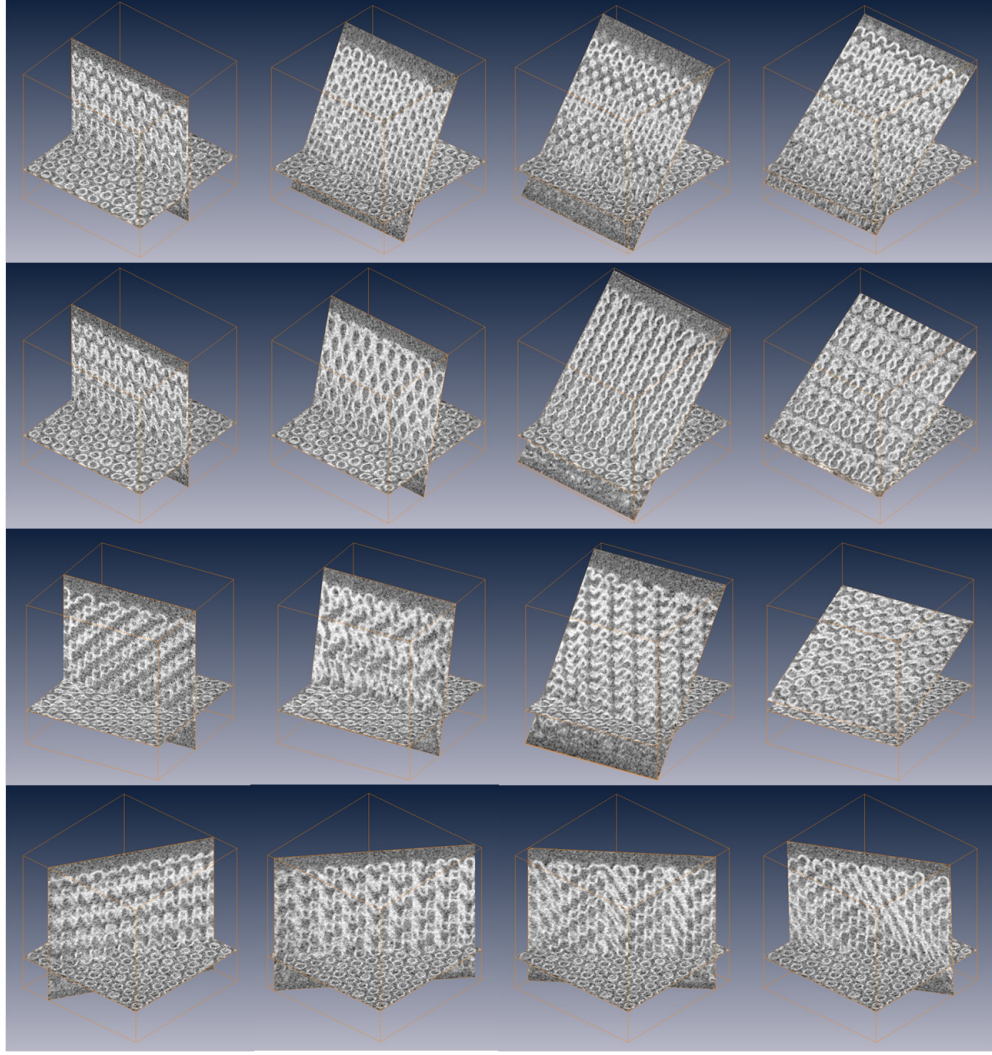


**Figure 4.13** Arbitrary slices of the reconstructed 3D cell from x-ray CT.

The reconstructed crystal has a polymer filling fraction of around 0.4, which agrees quite well with the estimated value obtained from spectra and the SEM measured layer spacing, using Bragg reflection and effective medium calculations for the refractive index.

$$\lambda = 2n_{eff}d$$

$$n_{eff} = \sqrt{f_{air}n_{air}^2 + f_{SU8}n_{SU8}^2}$$

Where  $\lambda$  is the first order reflectance peak wavelength,  $n_{eff}$  is the effective refractive index of the crystal,  $d$  is the layer spacing of the crystal.  $n_{air}$  and  $n_{SU8}$  are the refractive indices of air and SU-8 respectively, and  $f_{air}$  and  $f_{SU8}$  are their filling fractions. Layer spacing was measured

using the constructed cell. SEM top view measurement of in-plane periodicity was used as calibration, each pixel was calculated to average 32.7 nm, and the layer spacing of the scanned crystal was calculated to be 513 nm.

## 4.5 Spectra Analysis

### 4.5.1 Spectra Calculation with Reconstructed Crystal

In the reflectance spectrum of the SU-8 photonic crystal, shown in Figure 4.8, the first order peak is located at around 1.3 $\mu$ m and it has reflectance value close to 70%. The crystal also has distinct high energy peaks at 590nm and 660 nm with reflectance values around 20%, indicating the crystal has high optical quality. This is used as the standard for comparison against the predicted values for spectrum obtained from the reconstructed model. The reconstructed cell was used to calculate the spectra with the 1D Transfer matrix method as described in Chapter 3, which is a fair approximation for low dielectric constant materials because the contribution of diffractions from non-normal incidence is small. The slice number, filling fraction and effective refractive index of the reconstructed cell used in the spectra calculation is presented in Figure 4.14, and the comparison to measurement in Figure 4.15.

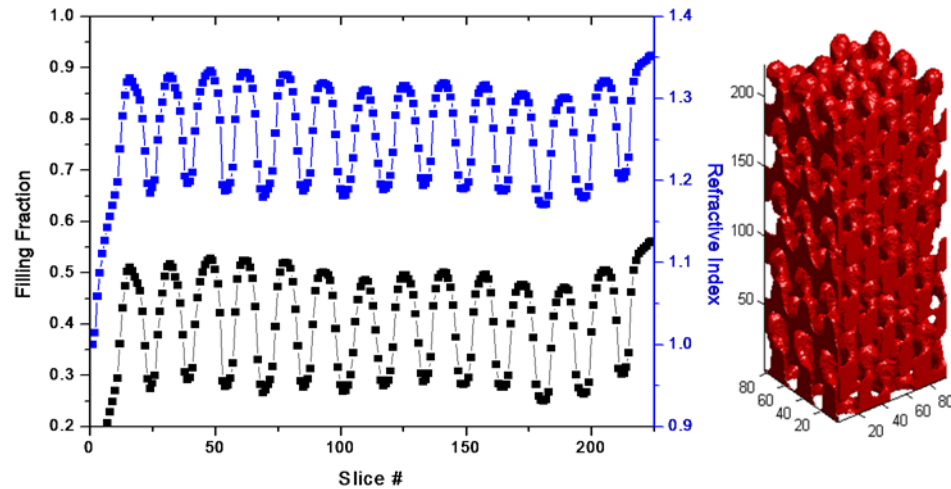


**Figure 4.14** For spectra calculation, the reconstructed cell is approximated as a stack of slices each with uniform refractive index distribution determined by the filling fraction.

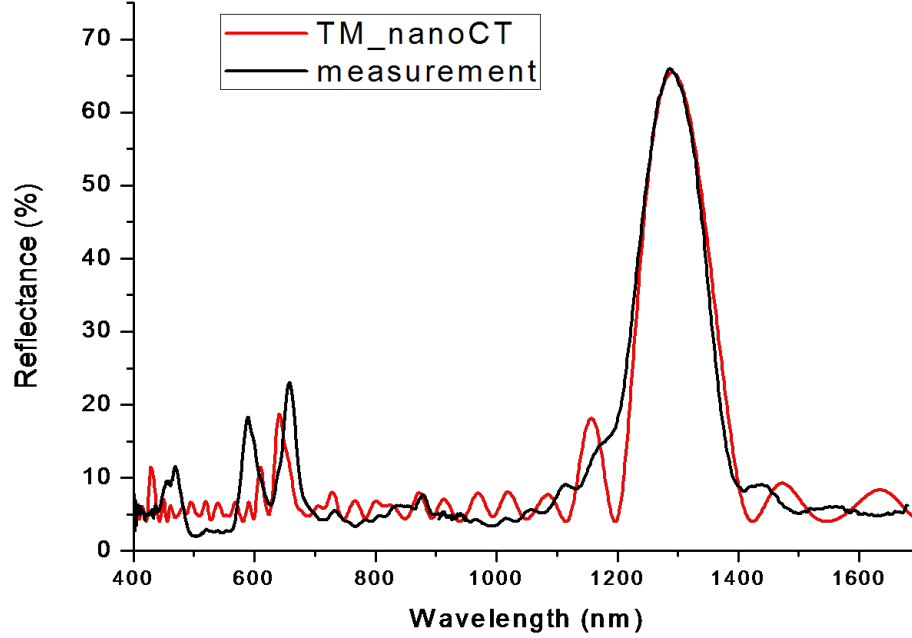


**Figure 4.15** Reflectance spectra plot of the polymer photonic crystal from measurement (black) and transfer matrix calculation with the CT cell (red).

The measured and calculated spectra have excellent matching of their first order peaks in position, height and width. Both spectra show other high energy peaks at similar locations. The difference between the two spectra is mostly likely due to the fact that the direct measurement and the CT scan were not taken at the exact same spot on the sample. Small differences in surface termination, thickness and filling fraction contribute to the variation of background fringes and high order peaks. However, the high energy peaks are consistent and reproducible across different samples of the same crystal structures measuring at different spots, meaning the crystals have good qualities. In order to accurately characterize and compare the high energy peaks, FDTD spectrum simulation of the CT structure should be performed.

#### 4.5.2 Comparison with Uniform Shrinkage Model

We compared the CT reconstructed cell with the uniform shrinkage calculated model, as presented in Chapter 3 to assess the similarity and accuracy of the two methods. Figure 4.16 shows the model structure, the CT extracted cell and their comparison overlay. The calculated



cell is constructed to match pixel dimensions and filling fraction (0.4) of the reconstructed cell. In the comparison, grey represents areas where both cells have air, green represents both having polymer, and unmatched are presented in their original colors. As the figure shows, the two cells are highly correlated overall. Taking the number of the matching pixels (green and gray) and divided it by the total number of pixels, the fitness of the two cells is calculated to be 89%. Observing the difference by slicing through the comparison cell (Figure 4.17), we can see the model has more polymer (yellow) connects with along the vertical directions, while the CT polymer (blue) tends to have more connectivity along the horizontal direction. It also appears that the CT cell does not have as sharp features as the model cells.

Due to shrinkage the model has shifted about 45% from its original interference pattern. So the vertical features were considerably longer and skinnier before the shrinkage and may not be resolved correctly by the polymer photoresist. The matching of the CT cell to the model suggests that most of the shrinkage comes from material loss during development. One suspect is that the system experiences some vibration during exposure, which causes the features smear out. Another possible cause is that there was not enough photoinitiator to provide sufficient crosslinking. While the limiting resolution of the x-ray microscopy technique may be at fault, SEM observations agree with the CT cell better than the model.

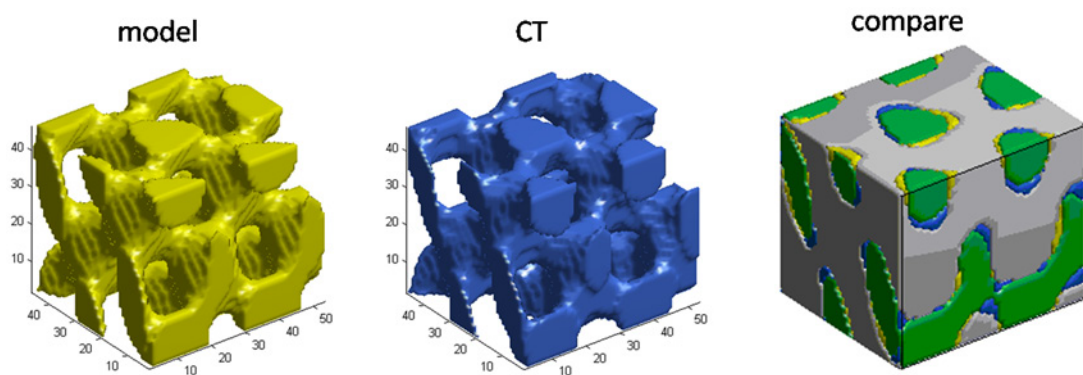


**Figure 4.16** Comparison between modeled cell and the CT cell overlay. Yellow represents polymer from model, blue represents polymer from the CT cell. In the comparison, green is shown where both cells are polymer, and grey is shown where both cells are air.

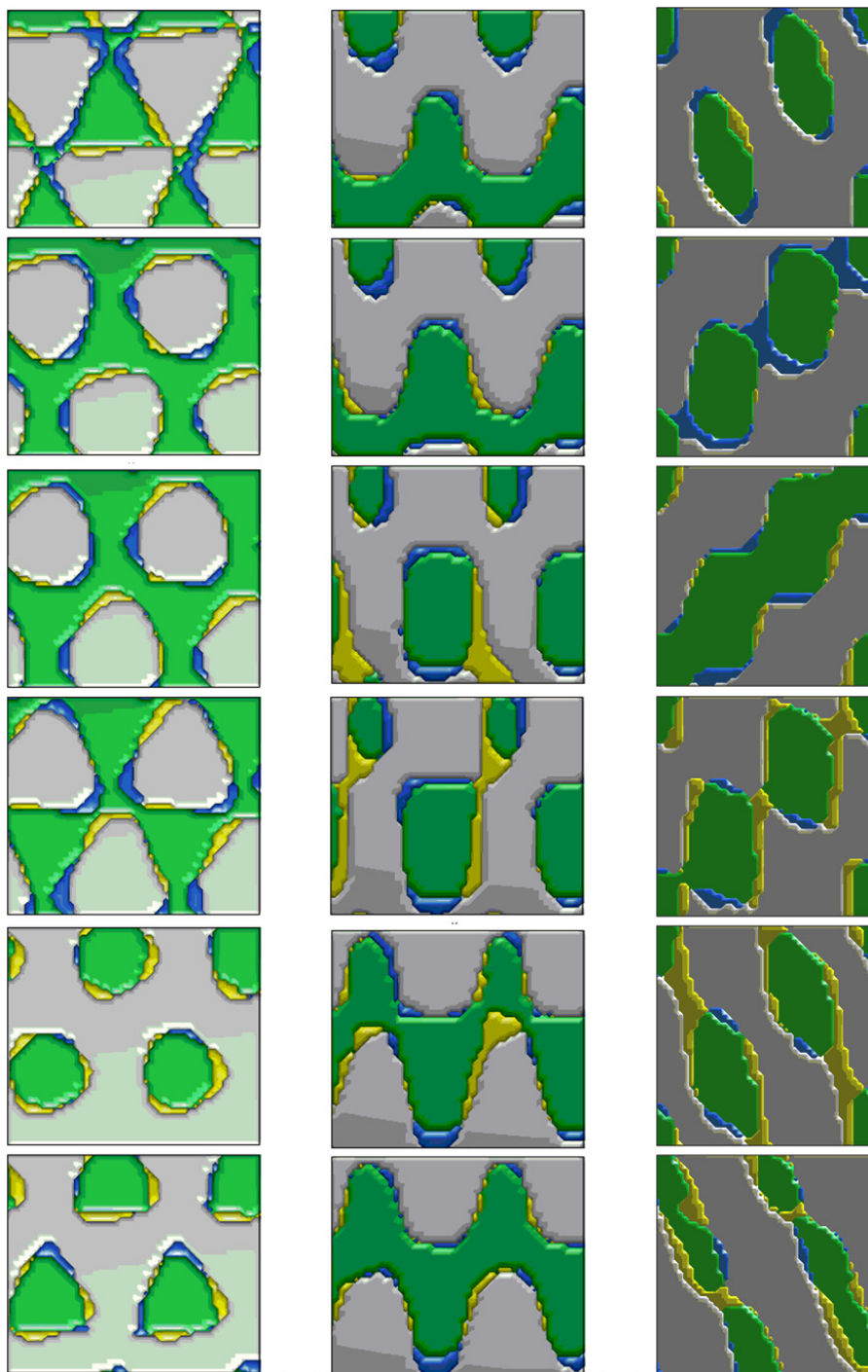


**Figure 4.17** Slices of the comparison cell, showing the matches (green & grey) and the mismatch, for yellow being the excess modeled polymer and blue being the excess CT reconstructed polymer.

Spectra calculation of the modeled cell was performed and compared to the result from the CT reconstructed cell, as shown in Figure 4.18. The main reflectance peak height from the calculation was lower than CT predicted spectra, despite the model cell having perfect regularity. Plotting the effective refractive index slices perpendicular to the normal direction for each cell, we can see that the CT cell has larger variation than the model cell. This explains why the reflectance of the reconstructed structure is higher than the modeled structure. The difference in the two spectra reflects the differences that exist between the model and the fabricated structure. While the CT structure is measured directly from the fabricated crystal, the thresholded and uniform shrinkage model may not be totally representative of the fabricated crystal optically, and the optical spectroscopy is sensitive to this slight difference in geometry. This sensitivity shows that the ability to probe the fabricated structure in real space is important.

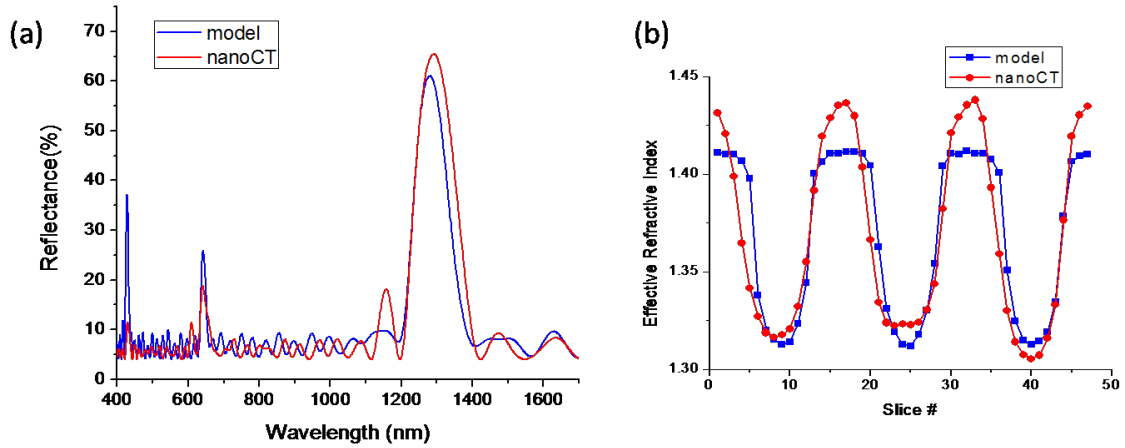


**Figure 4.18** (a) Comparison of the calculated spectra from the model structure and CT reconstruction using the 1D transfer matrix method (b) Effective refractive index variation with 1D slices for modeled cell and CT reconstructed cell.

#### 4.6 Conclusions and Future Directions

Real-space 3D imaging of fabricated holographic photonic crystals was demonstrated through ALD conformal growth of  $\text{HfO}_2$  on a SU-8 template. The three-dimensionally reconstructed cell was used for calculation of reflectance spectrum. The end result of which showed an excellent match with the measured spectra. The geometry of the reconstructed cell

was compared with the previously reported modeled cell. The two cells exhibited ~90% fitness between their structures, and the observable differences explained the relatively higher reflectance spectra displayed by the CT reconstructed cell over the modeled cell. By using x-ray tomography to measure the fabricated crystal, it is now possible to investigate the deformation process from an as-made crystal through processing and shrinkage. Several factors were considered to account for this, and may include each processing step [4], as well as the crosslink density variation (possibly leading to different shrinkage) and material loss to developer. This improved understanding of the correlation between the interference pattern and final fabricated crystal structure will greatly facilitate the design of optimum structures for photonic applications.

#### 4.7 References

- [1] M. Campbell, D. N. Sharp, M. T. Harrison, R. G. Denning, and A. J. Turberfield, "Fabrication of photonic crystals for the visible spectrum by holographic lithography," *Nature*, vol. 404, pp. 53-56, 2000.
- [2] M. Maldovan, C. K. Ullal, W. C. Carter, and E. L. Thomas, "Exploring for 3D photonic bandgap structures in the 11 fcc space groups," *Nature Materials*, vol. 2, pp. 664-667, 2003.
- [3] J. H. Moon, S. Yang, W. Dong, J. W. Perry, A. Adibi, and S. M. Yang, "Core-shell diamond-like silicon photonic crystals from 3D polymer templates created by holographic lithography," *Optics Express*, vol. 14, pp. 6297-6302, 2006.
- [4] R. C. Rumpf and E. G. Johnson, "Fully three-dimensional modeling of the fabrication and behavior of photonic crystals formed by holographic lithography," *Journal of the Optical Society of America a-Optics Image Science and Vision*, vol. 21, pp. 1703-1713, 2004.
- [5] X. L. Zhu, Y. G. Xu, and S. Yang, "Distortion of 3D SU8 photonic structures fabricated by four-beam holographic lithography with umbrella configuration," *Optics Express*, vol. 15, pp. 16546-16560, 2007.
- [6] J. R. Wilson, W. Kobsiriphat, R. Mendoza, H. Y. Chen, J. M. Hiller, D. J. Miller, K. Thornton, P. W. Voorhees, S. B. Adler, and S. A. Barnett, "Three-dimensional reconstruction of a solid-oxide fuel-cell anode," *Nature Materials*, vol. 5, pp. 541-544, 2006.
- [7] D. Attwood, "Microscopy - Nanotomography comes of age," *Nature*, vol. 442, pp. 642-643, 2006.



- [8] B. C. Larson and B. Lengeler, "High-resolution three-dimensional x-ray microscopy," *MRS Bulletin*, vol. 29, pp. 152-154, 2004.
- [9] A. Momose, "Recent advances in x-ray phase imaging," *Japanese Journal of Applied Physics Part 1-Regular Papers Brief Communications & Review Papers*, vol. 44, pp. 6355-6367, 2005.
- [10] S. A. Zhou and A. Brahme, "Development of phase-contrast X-ray imaging techniques and potential medical applications," *Physica Medica*, vol. 24, pp. 129-148, 2008.
- [11] C. G. Schroer, P. Cloetens, M. Rivers, A. Snigirev, A. Takeuchi, and W. B. Yun, "High-resolution 3D imaging microscopy using hard x-rays," *MRS Bulletin*, vol. 29, pp. 157-165, 2004.
- [12] Y. S. Chu, J. M. Yi, F. De Carlo, Q. Shen, W. K. Lee, H. J. Wu, C. L. Wang, J. Y. Wang, C. J. Liu, C. H. Wang, S. R. Wu, C. C. Chien, Y. Hwu, A. Tkachuk, W. Yun, M. Feser, K. S. Liang, C. S. Yang, J. H. Je, and G. Margaritondo, "Hard-x-ray microscopy with Fresnel zone plates reaches 40 nm Rayleigh resolution," *Applied Physics Letters*, vol. 92, p. 103119, 2008.
- [13] *Xradia nanoXCT laboratory user tool manual*, 2008.
- [14] [http://henke.lbl.gov/optical\\_constants/](http://henke.lbl.gov/optical_constants/).
- [15] G. F. Bahr, "Osmiums tetroxide and ruthenium tetroxide and their reactions with biologically important substances," *Experimental Cell Research*, vol. 7, pp. 457-479, 1954.
- [16] K. Kato, "The osmium tetroxide procedure for light and electron microscopy of ABS plastics," *Polymer Engineering and Science*, vol. 7, pp. 38-39, 1967.
- [17] J. S. Trent, J. I. Scheinbeim, and P. R. Couchman, "Ruthenium tetroxide staining of polymers for electron microscopy," *Macromolecules*, vol. 16, pp. 589-598, 1983.
- [18] M. A. Hayat, *Principles and Techniques of electron microscopy*, 4 ed.: Cambridge University Press, 2000.
- [19] M. Miyake, Y. C. Chen, P. V. Braun, and P. Wiltzius, "Fabrication of Three-Dimensional Photonic Crystals Using Multibeam Interference Lithography and Electrodeposition," *Advanced Materials*, vol. 21, pp. 3012-3015, 2009.
- [20] Y. Xu, X. Zhu, Y. Dan, J. H. Moon, V. W. Chen, A. T. Johnson, J. W. Perry, and S. Yang, "Electrodeposition of three-dimensional titania photonic crystals from holographically patterned microporous polymer templates," *Chemistry of Materials*, vol. 20, pp. 1816-1823, 2008.
- [21] J. S. King, E. Graugnard, O. M. Roche, D. N. Sharp, J. Scrimgeour, R. G. Denning, A. J. Turberfield, and C. J. Summers, "Infiltration and inversion of holographically defined polymer photonic crystal templates by atomic layer deposition," *Advanced Materials*, vol. 18, pp. 1561-1565, 2006.

## CHAPTER 5

### INFILTRATION OF 3D HOLOGRAPHIC PHOTONIC CRYSTAL TEMPLATES

#### 5.1 Introduction

Many theoretical predictions have been made for large photonic band gap structures with geometries that can be achieved by holographic lithography [1-6]. All of these designs and predictions assume direct replacement of the template with high refractive index material. However, many materials of interest such as silicon [7-11], germanium [12], and titanium dioxide [13] are infiltrated by a chemical vapor deposition technique, which has difficulty filling in the structure completely due to neck point pinch off. This phenomenon has been observed previously in literature [11, 13]. The change in geometry due to incomplete infiltration can alter the optical properties greatly from prediction. Efforts have been made to study the pinch off problem in the past; however there was no direct comparison to experimental results, and the method was not generalized for any arbitrary structures [14].

The first part of this chapter covers conformal growth simulation of holographic photonic crystals and experimental comparisons with atomic layer deposition of  $\text{Al}_2\text{O}_3$ , examined by scanning electron microscopy and optical spectroscopy. The second part of the chapter describes electrodeposition of  $\text{Cu}_2\text{O}$  into holographically defined photonic crystal templates, a method which can provide complete infiltration of the structure.

#### 5.2 Conformal Surfaces Formed by Atomic Layer Deposition

\* Significant portion of content are taken from manuscript “Complex three-dimensional conformal surfaces formed by atomic layer deposition: Computation and experimental verification” Andrew Brzezinski, Ying-Chieh Chen, Pierre Wiltzius, and Paul V. Braun. *Journal of Materials Chemistry* (Accepted) [15]

Y. C. Chen performed experimental design, crystal fabrication, atomic layer deposition and sample characterization with ellipsometry, FIB and optical spectroscopy.

### 5.2.1 Introduction

A photonic crystal's optical characteristics are directly dependent upon the material distribution within the structure. Studies of optical features as a function of the conformal deposition have been undertaken in colloidal crystal templates [13, 16] and woodpile templates [9, 12]. Such calculations are straightforward for templates described by the union of regular geometric shapes but not for more complex structures. The conformal surface problem is a challenge in the high-refractive-index infilling of photonic crystals because it is necessary to account for both the geometry of the original structure and the subsequent evolution of the conformally deposited material. It is not straightforward to calculate the evolving shape of the surface when conformal deposition occurs in topographically complex 3D templates such as those made using interference lithography.

Moon [14] required an elaborate method to study the infilling of templates fabricated by multibeam interference lithography. The intensity pattern from multiple overlapped coherent laser beams is calculated as the squared sum of the electric field vectors [6].

$$I(\vec{r}) = \left| \sum_{i \in \{beams\}} \vec{E}_i(\vec{r}) \right|^2$$

Moon starts with the common practice [11, 17, 18] of describing the photoresist template with an iso-intensity surface, assuming regions below some threshold intensity are dissolved away while regions above the threshold remain. A gross approximation of a conformally deposited material distribution is obtained by using two iso-intensity surfaces [11]. This approximation was then significantly improved by adding correcting terms to minimize the thickness variation between the two surfaces. However, the applicability to arbitrary 3D structures is limited by the trial and error method used to find enough appropriate adjustable parameters to achieve an acceptable error tolerance.

Here we introduce a universal conformal surface calculation method to determine the material distribution. First the conformal surface calculation method is presented. Next, the

fabrication and characterization of a conformally infilled photonic crystal template is described. Finally, experimental data are compared with predictions based on the conformal surface calculation.

### *5.2.2 Conformal Growth Calculation*

Our conformal surface calculation relies on the discretization of space into a large number of identically shaped parallelepipeds that occupy the sites of a lattice. These volume elements, or voxels, are initialized to contain either void space or the initial structure material. This permits the method to handle any arbitrarily complex 3D structure with the only limitation being that the error is proportional to the fineness of the discretization. Further discussion of the error is presented below after the description of our algorithm's two major components, determining if a path exists between an interior surface and an external deposition source, and depositing conformal layers of material on the existing surface. Path testing and surface propagation are iteratively applied in a series of finely discretized steps that evolve the surface. First, path testing, then surface propagation, again path testing, and so on. Each iteration is limited to propagating the surface by no more than a third the distance of the voxel diagonal, which is equivalent to the Courant–Friedrichs–Lewy condition [19] that applies to grid-based methods for solving equations.

Testing for a path between the deposition source and a surface is done with a “flood-fill” algorithm which is a common method for finding similarly colored adjacent pixels in a drawing program [20]. This algorithm starts at a voxel and recursively checks its nearest neighbors, and their nearest neighbors, and so on, until it ultimately finds a connected cluster of empty voxels through which deposition gases can flow. Deposition only occurs on surfaces that have a path to the deposition source. “Pinch-off” is said to occur when all paths between an interior surface and the external source have been closed due to conformal deposition. Pinch-off is depicted in Figure

5.1 where a path existed prior to the deposition of the shaded voxels, which now prevent gas flow into the pinched-off region.

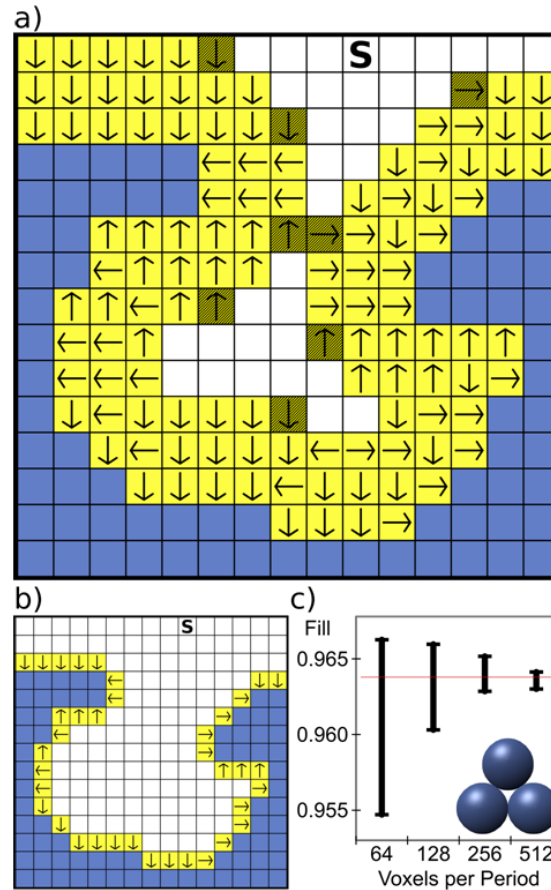


**Figure 5.1** (a) Two dimensional schematic of conformal deposition (yellow). The initial structure (blue) is more clearly seen in (b) where a continuous path exists between the source (S) and all the initial surface voxels. A one-voxel thick deposition occurred on the third iteration because each iteration increases the deposition thickness by one third the voxel length. Every deposited voxel points (arrows) to the path providing the nearest initial surface. In each iteration, voids (white) adjacent to filled voxels have the minimum distance to the initial surface (blue) tested and if the distance is less than or equal to the current deposition thickness then the void is filled. Only a void's nearest neighbors are probed (in the order: north, east, south, west) to find the minimum distance, following the path along the arrows until an initial surface (blue) is reached and then the Euclidean distance is calculated. Ties for minimum distance go to the first probed path. Voxels deposited in iteration 10 (shaded yellow) pinched-off the path between the source and central region in (a), but deposition can continue outside the pinched-off region. (c) Range of calculated total fill fractions (black) after conformal deposition to the pinch-off point versus the analytical result of 0.9641 for a face centered cubic lattice of spheres (red line); (inset) pinch-off occurs when the pore, centered on three touching spheres, is closed. [15]

Propagating the surface along the local normal is done in an implicit manner, avoiding the problematic calculation of the surface normal. The shortest distance between a point (a voxel) and a continuous surface (many voxels that lie on the interface between solid and void) is along a line that is normal to that surface. One may simply calculate the distance between every empty voxel and every surface voxel, depositing material into empty voxels wherever the deposition thickness exceeds the shortest distance to a surface. An algorithmic improvement ( $N^4$  versus  $N^5$  complexity) is obtained by assuming that the shortest distance to the template surface lies along a connected path of deposited voxels that necessarily originates at one of the voxel's nearest neighbors. These connected paths are dynamically constructed by having every deposited voxel point towards the nearest neighbor through which its shortest path was found (Figure 5.1). This algorithmic improvement has a slightly worse error bound for a given grid size because the central assumption is occasionally false. But, the benefits are a drastically reduced computation time. Furthermore, the memory requirement is reduced to only a portion of one byte per voxel, which permits the assignment of voxel attributes, such as several different material types, while only using one byte per voxel.

The space discretization sets the magnitude of the error because the calculated position of any surface cannot be resolved to less than the voxel size. The error in surface thickness is multiplied by the surface area of the structure to obtain the volumetric error. This error is typically the most important because the dielectric volume fraction strongly affects the spectral position of photonic features. For the case of a computational cell that has  $N^3$  voxels, the surface area and absolute error will be proportional to  $N^2$ , which gives a relative volumetric error proportional to  $N^{-1}$ .

Our method was validated using the analytical result of 3.59% total void fraction remaining for conformal deposition until pinch-off on an idealized colloidal crystal. Three mutually touching spheres (Figure 5.1 c) define the pore that was closed upon pinch-off. Periodic boundary conditions were applied to the parallelepiped computation volume, forming a face-

centered-cubic primitive unit-cell with angles of  $60^\circ$ ,  $60^\circ$ , and  $90^\circ$  between the edges. For each value of  $N$ , the number of voxels per edge, 1000 different origin positions (small shifts within one voxel) were employed and the result (Fig. 5.1 c) is consistent with the  $N^{-1}$  dependence of the volumetric error. A maximum error of 0.11% is obtained for  $N = 512$ , or about 56% of  $N^{-1}$ , which demonstrates the accuracy of our method. Using a contemporary personal computer, a single calculation for  $N = 512$  completes in about two minutes. Thus, it is practical to incorporate our method when performing design optimization, such as maximizing the photonic bandgap. Since the error, storage, and run-time are respectively proportional to  $N^{-1}$ ,  $N^3$ , and  $N^4$ , halving the error requires 8 times the storage and 16 times longer to compute.

### 5.2.3 Experimental Comparison

Comparison of the conformal surface calculation was performed with procedure outlined in Figure 5.2.

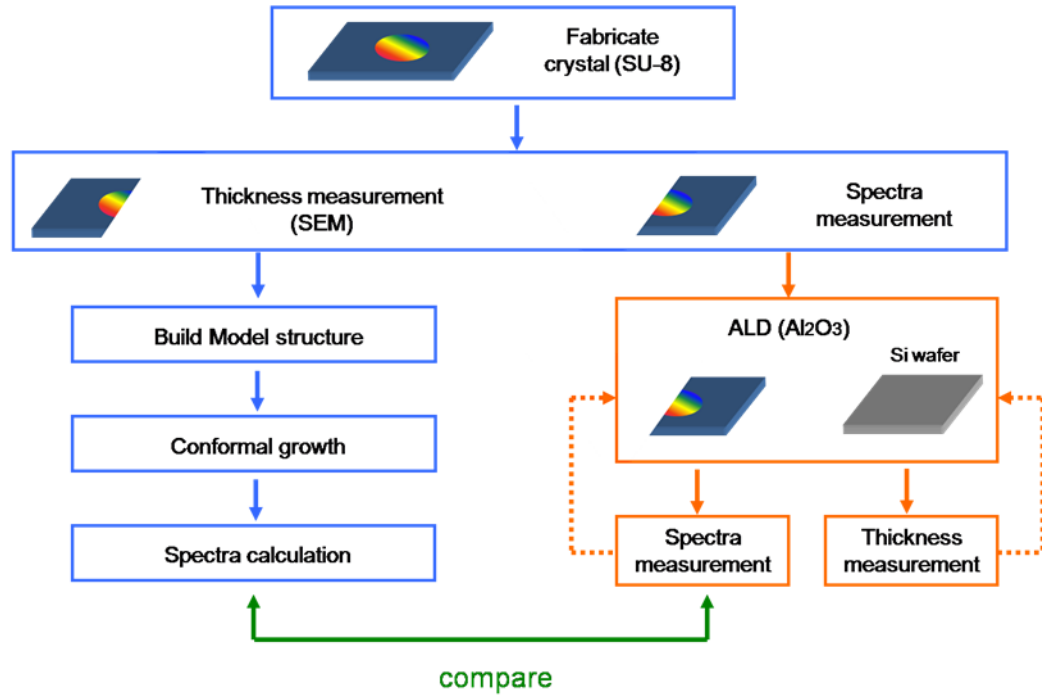


**Figure 5.2** Experimental comparison scheme for conformal growth study.

The experiment started with the use of multi-beam interference lithography to make five SU-8 photo polymer templates with differing parameters following our published procedure [18]. Each template (Figure 5.3) was conformally infilled by atomic layer deposition (ALD) of alumina. ALD [21] is a deposition technique that iterates between two self-limiting reactions to conformally deposit a monolayer of material per cycle, thus allowing a high degree of control over the deposition thickness. The SU-8 withstands the 85 °C ALD temperature and permits the use of an exposure intensity iso-surface to analytically describe the template surface. As alumina is deposited, the average refractive index of the structure increases, and thus the reflectance peak red shifts. The modest refractive index of 1.6 for alumina, however, avoids overlapping the reflectance peak with the SU-8 absorption at wavelengths longer than 2.4  $\mu\text{m}$  enabling accurate comparison of theory and experiment.

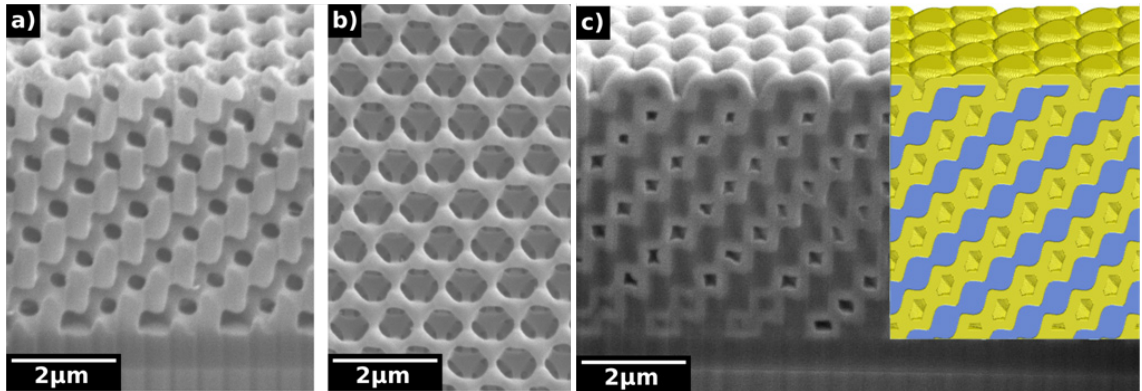


**Figure 5.3** (a) Focused-ion beam milled (FIB) cross-section of SU-8 photonic crystal template and the (b) top view. (c) FIB cross-section of template after 228 nm ALD shown beside the calculated structure (at right) showing polymer (blue) and alumina (yellow); in the micrograph, alumina is brighter than SU-8. The alumina thickness inside the structure is limited to  $\sim 177$  nm due to pinch-off of the pores. [15]

The reflectance spectrum was measured starting with the SU-8 polymer template, and then after every 100 cycles (150 cycles for the first iteration) or 12.7 nm of alumina ALD, ultimately ending after 1850 cycles (Figure 5.3 c). A silicon wafer was also present in the ALD chamber and the thickness of deposited alumina was measured by ellipsometry after every



iteration. Reflectance spectra were carefully measured from several specific locations on each template. The discussion that follows focuses on the data from one specific location on one template because this is representative of all measurement spots and all five templates. Spectra obtained from different locations on a single template only show minor variance and all spectra follow a similar trend.

The structure of the initial SU-8 template was determined by fracturing the starting sample into two pieces, one of which was examined by focused-ion-beam milling and scanning electron microscopy (Figure 5.3), the other of which was infilled with alumina. The spacing between the (111)-layers parallel to the substrate in the fcc-like structure was measured as 520 nm. The shrinkage to 44% of the original 1178 nm (111)-spacing in the interference lithography setup is typical for 3D SU-8 structures [22, 23]. In-plane shrinkage is suppressed because the template adheres to the substrate. The total thickness of the template is 10.5 (111)-layers and it sits on a substrate consisting of an adhesion promoting 700 nm SU-8 layer on top of a microscope cover glass slide. The material distribution was obtained by the conformal surface calculation method and subsequently used as input for a finite difference time domain calculation [24]. The starting point for the calculations is the iso-intensity surface that corresponds with the polymer filling fraction consistent with the Bragg approximation of the reflectance peak (see experimental).

The position and magnitude of experimental spectral features in Figure 5.4 are well matched by the FDTD calculation. As the alumina content increases, the positions and magnitudes of the reflectance peaks and Fabry-Perot fringes evolve in unison. The slightly lower measured versus calculated reflectance is expected because of the small imperfections due to surface micro-roughness, residual stress, resist resolution limits, and imperfect laser beam profiles. At 129 nm deposited alumina, the FDTD and experimental reflectance simultaneously vanish due to the negligible variation in the average refractive index in the normal direction. At 177 nm of alumina the calculated structure becomes pinched off with the void space occupying

5.9% of the total volume, or 10.3% of the original void space. Subsequent deposition only occurs on the topmost surface and this explains the lack of evolution for the spectra between 166 nm and 203 nm of alumina. All this indicates that the calculated structure is an accurate description of the experimental structure.

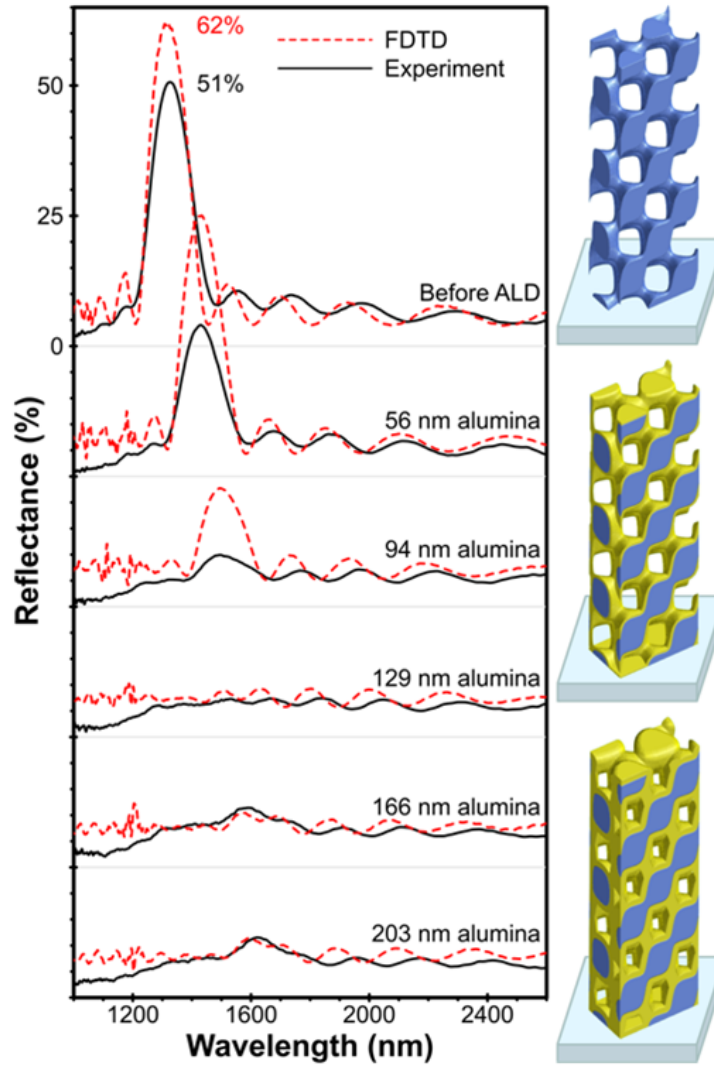


**Figure 5.4** Comparison of experimental (solid black) and FDTD calculated (dashed red) reflectance; each curve is offset by 25% for clarity. The calculation unit cell showing the original template (top right), after 56 nm ALD (middle right), and after 129 nm (bottom right), showing the polymer (blue) and conformally deposited material (yellow). [15]

Additional verification of the conformal surface calculation is obtained by showing that a small perturbation in the input (111)-spacing yields measurable differences in the FDTD spectra. The calculation was repeated with 500 nm and 540 nm (111)-spacing. Figure 5.5 compares the reflectance peak position and magnitude for all 3 calculated spacings and the experimental structure. The 520 nm spacing curve follows the experimental curve closely. On the other hand, both the 500 nm and 540 nm spacing peak-positions diverge from the experiment and they show different plateaus due to pinch-off at 151 nm and 198 nm of alumina, respectively. This demonstrates that a small  $\pm 4\%$  change to the (111)-spacing input into the calculation leads to significantly different distributions of conformally deposited material.

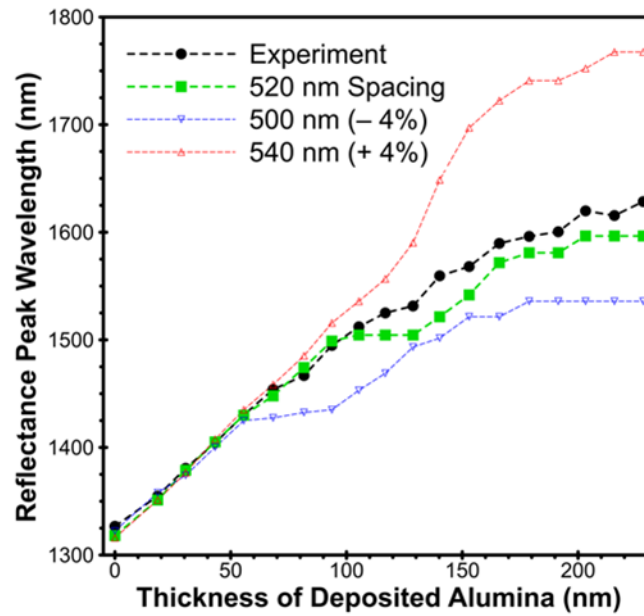


**Figure 5.5** Evolution of experimental and FDTD calculated reflectance peak position during ALD of alumina on a SU-8 polymer template. [15]

After 228 nm of alumina deposition, the structure was milled by a focused ion beam to reveal an excellent match (Fig. 5.3 c) with the calculated structure. Both the calculated and experimental structures have similar polymer cross-sections, similar thicknesses of deposited alumina, and similarly sized pinched-off voids. Based on Figure 5.3 c and considering the

demonstrated correspondence between our calculated and observed spectra, it appears that conformal deposition techniques can achieve close to the theoretical maximum thickness before pinch-off in complicated 3D structures. Furthermore, the resulting deposition appears to have a uniform thickness throughout the depth of the structure.

#### 5.2.4 Conclusions

To summarize, an accurate and universal method to calculate the material distribution by conformal deposition processes within arbitrary 3D structures was developed. Photonic crystal polymer templates were fabricated and subjected to ALD. The conformal surface calculation was verified by scanning electron microscopy, comparisons between measured and FDTD spectra. This establishes the conformal surface calculation method as being a useful tool for the design and analysis of photonic crystals and other complex 3D structures in which conformal deposition or etching occurs.

#### 5.2.5 Experimental

*Template Fabrication:* The photoresist was formulated by mixing cyclopentadienyl(fluorene)-iron(II) hexafluorophosphate (Aldrich), in a SU-8 2000 resin (MicroChem). The resist was spun at 1000 rpm for 30 s, baked for one hour at 65°C to 95°C, then exposed with  $\sim 6 \text{ J/cm}^2$  from a 532 nm laser (Coherent, Verdi V5) split into a four-beam umbrella configuration with the polarizations defined in reference [25]. The side beam to central beams intensity ratio is 1:3 and they make a 25° angle in the resist. An 80°C bake was performed for 15 minutes in dry air and the sample was immersed in propylene glycol methyl ether acetate for one hour, and transferred to isopropanol. Critical point drying was then performed (Tourisimis, Samdri 790).

*Atomic Layer Deposition:* ALD (Cambridge Nanotech) of alumina was performed at 85 °C. Prior to characterization or deposition, the templates were allowed to relax for 6 hours at 85 °C in the ALD chamber. One ALD cycle consists of 0.03 s pulse of water vapor with 2 s hold, 65 s

nitrogen at 20 sccm nitrogen flow, then trimethylaluminum was released and pumped using the same parameters.

*Ellipsometry:* The alumina thickness on the silicon wafer was measured using spectroscopic ellipsometry (J. A. Woollam VASE) from 800 nm to 1700 nm. Data fitting was performed using the Cauchy model. Also, refractive indexes for SU8 and alumina were measured as 1.57 and 1.60, respectively.

*Focused Ion Beam Milling:* Cross-sections of polymer and alumina-filled templates were generated (FEI DB-235). Etching was performed at 3000 pA, and cleaning at 300 pA. Images were obtained after Au-Pt coating of the milled surface. *Spectroscopy:* Reflectance spectra were taken with a Fourier Transform Infrared spectrometer (Vertex 70, Bruker) coupled with an optical microscope (Bruker Hyperion 2000) with a liquid-nitrogen-cooled InSb detector. A 4x objective with 0.1 NA was used with a 150  $\mu\text{m}$  spot size. The reflectance was normalized to a silver mirror. *Conformal surface calculation and FDTD:* The parameters of the experimental structure were used to construct a computational cell with cubic  $(1.6 \text{ nm})^3$  voxels. This rectangular unit cell is periodic in the plane of the structure, finite in the normal direction, and consists of a substrate, 10.5 (111)-layers of photonic crystal, and air above that. The 43% polymer filling fraction was obtained using

$$\lambda_{\text{Bragg}} = 2d_{111}\sqrt{(1 - f_{\text{SU-8}}) \cdot n_{\text{air}}^2 + f_{\text{SU-8}} \cdot n_{\text{SU-8}}^2}$$

where  $d_{111}$ ,  $f_{\text{SU-8}}$ , and  $n$  are respectively the (111)-layer spacing, filling fraction, and refractive index. The iso-surface produced with this filling fraction was uniformly shrunk in the normal direction to 44% its original size. The material distribution was calculated for various deposition thicknesses and used as input for FDTD (MEEP [24]) calculations using  $(35 \text{ nm})^3$  voxels. A  $\sim 0.7^\circ$  misorientation of the experimental (111)-surface was taken into account by averaging eight FDTD spectra with differing (111)-surface terminations to produce each presented spectra. The entire procedure was repeated assuming 500 nm and 540 nm (111)-spacings.

### 5.3 Complete Infiltration with Electrodeposition

\* Content taken from manuscript “Fabrication of Three-Dimensional Photonic Crystal Using Multibeam Interference Lithography and Electrodeposition” Masao Miyake, Ying-Chieh Chen, Paul V. Braun, and Pierre Wiltzius, *Advanced Materials*, vol. 21, pp. 3012-3015, 2009 [26]

Y. C. Chen assisted with SU-8 template fabrication procedure and performed band diagram calculation.

#### 5.3.1 Introduction

Electrodeposition is capable of growing a variety of metals and semiconductors into complex 3D geometries, as demonstrated by successful electrodeposition of inverse opal structures [27-30]. The combination of interference lithography and electrodeposition, therefore, has a great potential to produce a variety of photonic crystals with unique properties. Recently, a TiO<sub>2</sub> replica of an interference-lithographically defined template was fabricated using electrodeposition of titania sol-gel [31]. However, as is the case in conventional sol-gel processes [32], this technique requires calcination of infilling precursor to form TiO<sub>2</sub>, resulting in volume shrinkage and a loss of long-range order of the structure. Here, we selected Cu<sub>2</sub>O as an infilling material because of its high index of 2.6 and transparency at wavelengths greater than ~600 nm [33-35]. Since crystalline Cu<sub>2</sub>O is directly electrodeposited from an aqueous solution, high-temperature processes are not required, helping to maintain structural integrity.

We demonstrate the fabrication of a high-quality 3D photonic crystal through electrodeposition into a polymer template created by multibeam interference lithography, followed by removal of the template. Complete infilling of the template is achieved through bottom-up electrodeposition.

#### 5.3.2 Template Fabrication

The 3D polymer template was fabricated on a conductive, transparent indium tin oxide (ITO)-glass substrate by exposing a negative-tone photoresist, SU-8, to superimposed

interference beams over a spot size of  $\sim 3\text{mm}$ . The template is required to stay in contact with the substrate for reproducible infiltration. However, swelling of SU-8 in developer solution (propylene glycol methyl ether acetate, PGMEA) often induces delamination from the substrate. In addition, the high surface tensions of the aqueous solution and electrodeposited  $\text{Cu}_2\text{O}$  cause the template film to lift off during electrodeposition. To avoid these problems, the ITO substrate was treated by  $\text{O}_2$  reactive-ion etching (RIE) before coating with SU-8. Additionally, the developed template was hard-baked at  $90^\circ\text{C}$ . These treatments improved the adhesion between the template and ITO, and prevented delamination during processing. Figure 5.6 presents scanning electron microscopy (SEM) images of the polymer template formed via the interference lithography. The 3D pattern has an fcc-like symmetry with shrinkage in the  $\langle 111 \rangle$  direction, which is orientated perpendicular to the substrate. The distance between nearest neighbors in a (111) plane was measured by SEM to be  $\sim 900\text{nm}$  and the spacing of (111) planes to be  $\sim 520\text{ nm}$ , corresponding to 30% shrinkage in the  $\langle 111 \rangle$  direction from the true fcc lattice. The thickness of the 3D film was  $\sim 7\text{ }\mu\text{m}$ .

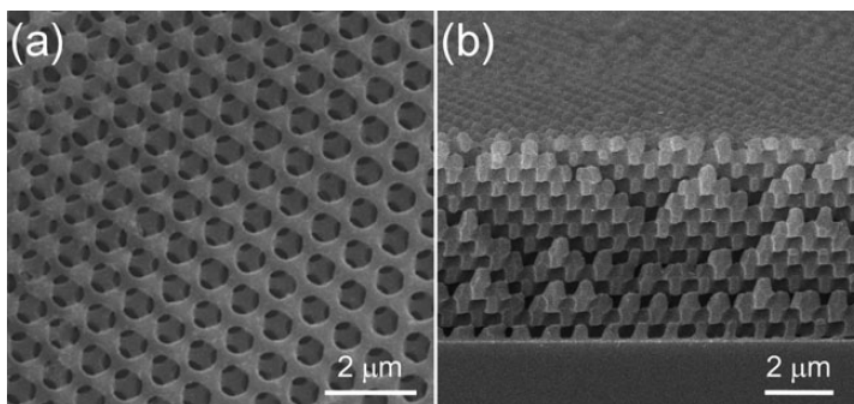


**Figure 5.6** SEM images of polymer template with fcc-like lattice symmetry fabricated by holographic lithography. a) Top surface and b) fractured cross-section. [26]

### 5.3.3 Electrodeposition

The cathodic electrodeposition of  $\text{Cu}_2\text{O}$  [34] was potentiostatically performed at  $65^\circ\text{C}$  using the ITO substrate with the polymer template as a working electrode. The electrolyte was an

aqueous solution containing copper sulfate and lactic acid at pH 9. Although  $\text{Cu}_2\text{O}$  could be electrodeposited over a pH range between 9 and 12, the smoothest films were deposited at pH 9. A cross-sectional SEM image of the sample after electrodeposition (Fig. 5.7) shows that  $\text{Cu}_2\text{O}$  grew inside the template starting from the substrate. The absence of both air voids in the  $\text{Cu}_2\text{O}$  layer and obvious gaps between the deposited  $\text{Cu}_2\text{O}$  and the template indicate that the cavity of the template was filled with  $\text{Cu}_2\text{O}$  completely. The thickness of the  $\text{Cu}_2\text{O}$  layer can be controlled by electrodeposition time. Using our deposition parameters,  $\text{Cu}_2\text{O}$  layers with a thickness of about  $6\text{ }\mu\text{m}$  were electrodeposited in 1 h.

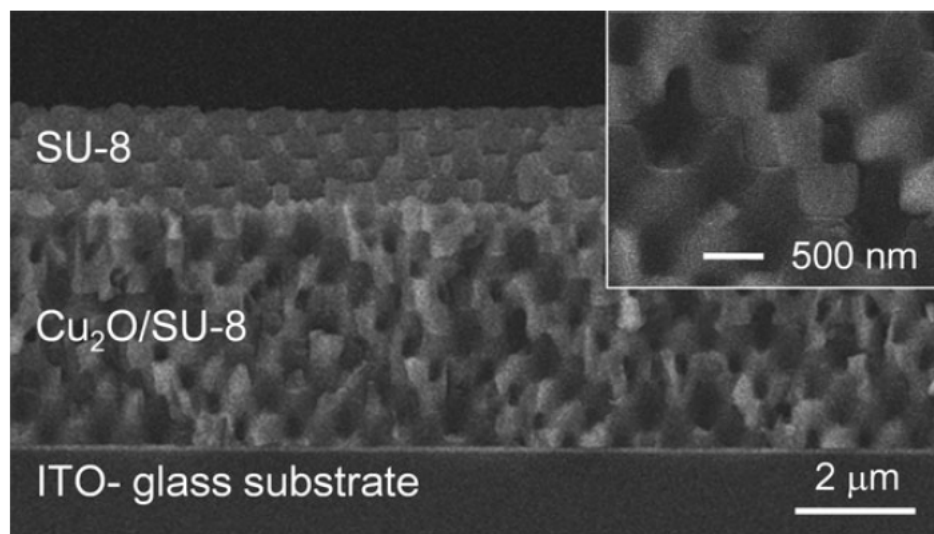


**Figure 5.7** Cross-sectional SEM image of  $\text{Cu}_2\text{O}$  electrodeposited part way through a 3D SU-8 template. The inset shows  $\text{Cu}_2\text{O}/\text{SU-8}$  composite region at a higher magnification. [26]

#### 5.3.4 Template Removal

After electrodeposition, to maximize the contrast of refractive index in the 3D structure, the polymer template was removed by isotropic RIE using a mixture of  $\text{O}_2$  and  $\text{CF}_4$  for 15 min. SEM images of the resultant structure show that the template was completely removed from the 3D composite, and that a highly ordered 3D porous structure of  $\text{Cu}_2\text{O}$  was successfully formed (Fig. 5.8 a and b). These SEM images also reveal that the  $\text{Cu}_2\text{O}$  structure has well-defined,



smooth surfaces in the bulk of the structure; however, the top surface is relatively rough. The rough surface is not desirable because it causes diffuse scattering, which reduces the optical strength of the photonic crystal. We eliminated the rough surface using simple mechanical polishing.  $\text{Cu}_2\text{O}$  was electrodeposited all through the template. Then, the overlayer of  $\text{Cu}_2\text{O}$  was polished off using 50nm alumina abrasive, exposing a flat, smooth section of  $\text{Cu}_2\text{O}$ /polymer composite. Finally, the polymer template was removed using RIE. The polished photonic crystal exhibited stronger iridescence than the nonpolished one, suggesting that the rough top surface that scatters light was removed and a flatter surface with a uniformly ordered structure was created. SEM images of the polished photonic crystal clearly show the formation of a smoother top surface (Figure 5.8 c and d).

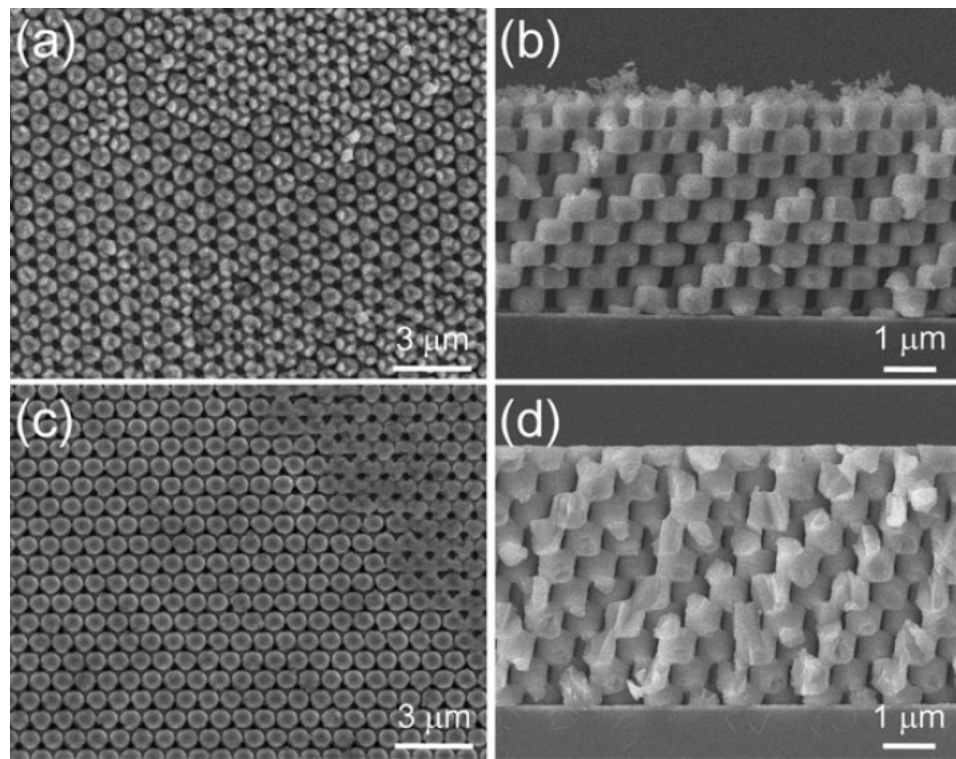


**Figure 5.8** SEM images of inverse 3D  $\text{Cu}_2\text{O}$  photonic crystals after removal of polymer template by RIE. (a) Top surface and (b) fractured cross-section of a  $\text{Cu}_2\text{O}$  photonic crystal electrodeposited within the template followed by RIE of the template. (c) Top surface and d) fractured cross section of a polished  $\text{Cu}_2\text{O}$  photonic crystal. [26]

### 5.3.5 X-ray Diffraction Characterization

Copper can have two oxidation states,  $\text{Cu}_2\text{O}$  and  $\text{CuO}$ . To confirm that the resultant photonic crystal was composed of  $\text{Cu}_2\text{O}$ , the sample after RIE of the template was characterized using X-ray diffraction (XRD). The XRD pattern of the photonic crystal showed only the  $\text{Cu}_2\text{O}$  200 diffraction peak, except for reflections from the ITO-glass substrate (Figure 5.9). It is known that  $\text{Cu}_2\text{O}$  bulk films electrodeposited under the same conditions without 3D template have a  $\langle 100 \rangle$  preferred orientation to the substrate [34]. Similar to the bulk film, the XRD of the photonic crystal indicated that crystalline  $\text{Cu}_2\text{O}$  with the  $\langle 100 \rangle$  orientation was grown inside the complicated 3D structure. The XRD also suggests that there is no obvious second phase in the  $\text{Cu}_2\text{O}$  photonic crystal. This indicates successful electrodeposition of  $\text{Cu}_2\text{O}$  into the 3D template as well as successful removal of the template without conversion of  $\text{Cu}_2\text{O}$  to  $\text{CuO}$ .

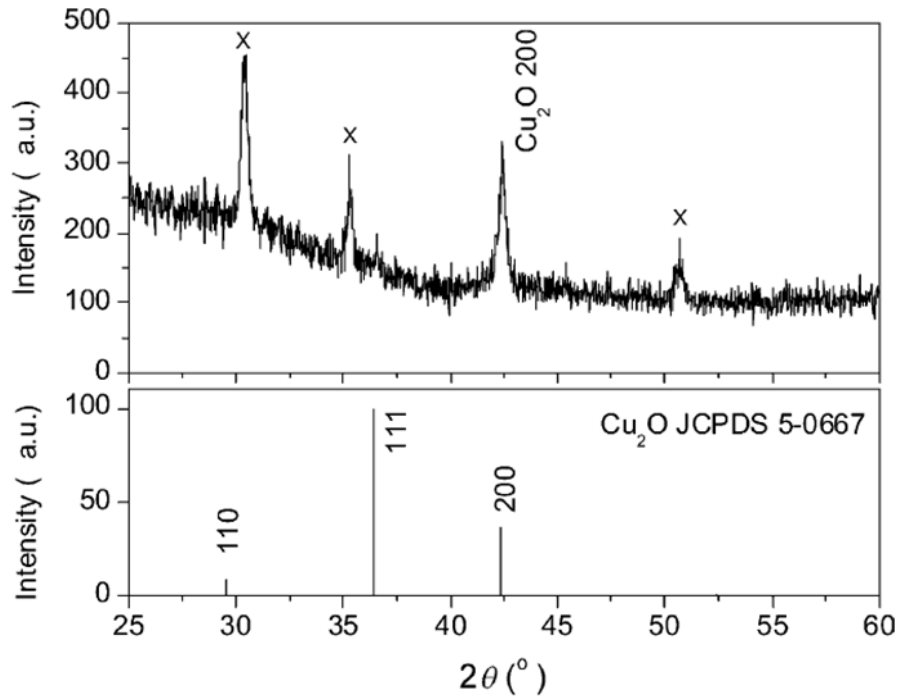


**Figure 5.9** XRD pattern of electrodeposited  $\text{Cu}_2\text{O}$  photonic crystal after removal of the SU-8 template by RIE. (x) Reflections from ITO-glass substrate. [26]

### 5.3.6 Optical Spectroscopy

Figure 5.10 presents normal-incidence reflectance spectra of the polymer template before electrodeposition and the Cu<sub>2</sub>O/air photonic crystal, and compares them with calculated photonic band structures in the <111> direction. In the reflection spectra of the template (Fig. 5.10 a), a peak was observed at ~1.3 μm, which is in agreement with the calculated position of the (111) stop band for the template with polymer-filling fraction of 45%. This filling fraction is consistent with the estimation from the Fabry–Perot fringes, the template thickness, and the refractive index of bulk SU-8 film, 1.57 [18]. The increase in the spectra background with increasing wavelength is due to the reflection off the ITO-glass substrate. The inversion of the polymer template by Cu<sub>2</sub>O increases the effective refractive index, resulting in a red shift of the reflection peak to 2.0 μm (Figure 5.10 b). The peak position matches well with the band structure, assuming the exact inverse structure of the template. The peak reflectance increased from ~50% for the template to nearly 100% for the inverse Cu<sub>2</sub>O photonic crystal. The nearly 100% peak reflectance, which includes a background of ~15%, at the theoretically predicted position provides evidence for complete inversion with void-free Cu<sub>2</sub>O, and the high quality of the resultant photonic crystal. The peak reflectance is remarkably high compared with those reported for 3D photonic crystals fabricated through inversion of polymeric templates. The high reflectance is due to both the high degree of structural order within the photonic crystal and the smooth surface. We note that a similarly ordered photonic crystal with a rough surface has a much lower reflectivity. One important reason for the high quality of the structure is the low temperature of the electrodeposition-based inversion process, which enables preservation of the structure of the polymer template.

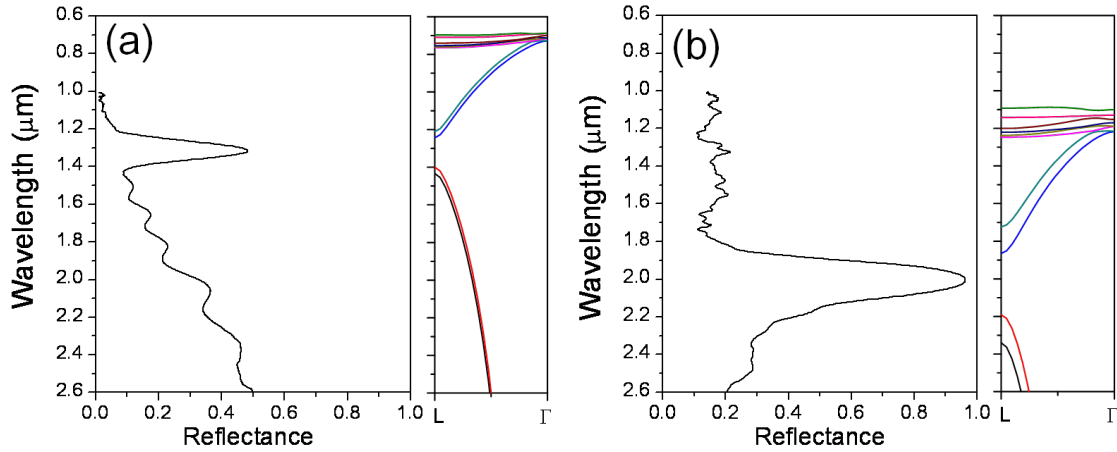


**Figure 5.10** Reflection spectra and calculated photonic band structure in  $\langle 111 \rangle$  direction for (a) polymer template and (b) inverse  $\text{Cu}_2\text{O}$  photonic crystal. [26]

### 5.3.7 Conclusions

In conclusion, we have demonstrated that high-quality 3D photonic crystals can be created through electrodeposition into a polymer template fabricated by interference lithography followed by RIE of the template. The contiguous internal space of the polymer template was completely filled with crystalline  $\text{Cu}_2\text{O}$  through bottom-up growth by electrodeposition, and thus, etching of the template after electrodeposition resulted in the  $\text{Cu}_2\text{O}$ /air photonic crystal with the exact inverse structure of the template. The top surface of the as-electrodeposited photonic crystal was effectively smoothed by polishing. The resultant  $\text{Cu}_2\text{O}$  photonic crystal showed a peak reflectance of almost 100% at the theoretically predicted wavelength. The fabrication process established here is applicable to other polymeric templates, such as those fabricated by phase mask lithography [36] and direct laser-writing [37]. The complete infiltration and precise replication through our process offer further flexibility in designing photonic-crystal devices.

### 5.3.8 Experimental

*Fabrication of Template:* The photoresist solution was prepared by mixing 0.5 wt% solid content of a photoinitiator, cyclopentadienyl(fluorene)iron(II) hexafluorophosphate (Aldrich), in an SU-8 solution (MicroChem, SU-8 2000 series). ITO glass with a sheet resistance of 15–30V was

cleaned in acetone and isopropanol, followed by RIE with  $O_2$  flow (10 sccm, 10 mTorr, 1 Torr=133.32 Pa) under applying field power of 150W for 3 min. Immediately after RIE, the SU-8 film was spin-coated (1000 rpm, 30 s) on the ITO substrate. It was exposed to four visible laser beams split from one coherent laser source (laser output of 5.4 W, frequency-doubled Nd: YVO<sub>4</sub> laser, 532 nm) and arranged in an umbrella geometry [18] for 0.5 s. The angle between the central beam and side beams was 42.58° in air, corresponding to 258 inside the unexposed photoresist. The central beam was circularly polarized, and the side beams were linearly polarized in their incident planes. After exposure, the film was post-baked at 80 °C for 15 min in dry air and developed in PGMEA for 1 h, followed by rinse in isopropanol. The sample was supercritically dried with CO<sub>2</sub> from isopropanol, and then hard-baked at 90 °C for 15 min.

*Electrodeposition:* Electrodeposition of Cu<sub>2</sub>O [34] was performed using a conventional three-electrode setup. A platinum plate and a Ag/AgCl in saturated potassium chloride aqueous solution (SSE) were used as counter and reference electrodes, respectively. The electrolyte was an aqueous solution containing cupric sulfate (0.2 M) and lactic acid (1.6 M). The pH of the solution was adjusted to 9 by addition of sodium hydroxide. The solution temperature was kept constant at 65 °C during deposition. The Cu<sub>2</sub>O layer was grown under potentiostatic conditions at -0.55 V versus SSE. To facilitate infilling of the hydrophobic SU-8 template with the cupric sulfate aqueous solution, the 3D template was first wetted by ethanol before electrodeposition.

*Removal of Template:* After electrodeposition, the polymer template was removed by RIE under O<sub>2</sub> and CF<sub>4</sub> flows at 20 and 2 sccm, respectively, with a base pressure of 500 mTorr and a power of 200W for 15 min. The sample was washed in ethanol briefly after RIE.

*Characterization:* XRD was performed using a Rigaku D-Max diffractometer with a Cu X-ray tube. Before measurement, Cu<sub>2</sub>O solid film deposited outside the template was shaved off from the sample so that detected signals were only from the photonic crystal and the substrate.

Reflectance spectra were measured using a Bruker vertex 70 FTIR system coupled with a Hyperion 1000 microscope. A 10X objective with a numerical aperture of 0.25 was used for

measurement. The collection area was limited to a 75 mm diameter spot using an aperture in the image plane of the optical path. Spectra were normalized to a silver mirror. For photonic-band-structure calculations, a model structure of the polymer template was constructed as follows [18] : the intensity distribution in the original interference pattern was calculated from the beam parameters. It was shrunk perpendicularly to the substrate to account for shrinkage during development and to match the  $\langle 111 \rangle$  spacing, 520 nm, observed by SEM. In the modified intensity distribution, the region with higher intensity than a threshold was taken to be polymer and air-filled the remainder. The threshold was chosen to match the polymer filling fraction of 45%. The inverse structure of the template was taken as the model of the  $\text{Cu}_2\text{O}$  photonic crystal. Photonic-band structures were calculated using the MIT Photonic Bands Package [38], where the refractive indices of 1.57 [18] and 2.6 [33-35] were used for SU-8 and  $\text{Cu}_2\text{O}$ , respectively.

#### 5.4 References

- [1] C. K. Ullal, M. Maldovan, M. Wohlgemuth, and E. L. Thomas, "Triply periodic bicontinuous structures through interference lithography: a level-set approach," *Journal of the Optical Society of America a-Optics Image Science and Vision*, vol. 20, pp. 948-954, 2003.
- [2] D. C. Meisel, M. Wegener, and K. Busch, "Three-dimensional photonic crystals by holographic lithography using the umbrella configuration: Symmetries and complete photonic band gaps," *Physical Review B*, vol. 70, p. 165104, 2004.
- [3] C. K. Ullal, M. Maldovan, E. L. Thomas, G. Chen, Y. J. Han, and S. Yang, "Photonic crystals through holographic lithography: Simple cubic, diamond-like, and gyroid-like structures," *Applied Physics Letters*, vol. 84, pp. 5434-5436, 2004.
- [4] O. Toader, T. Y. M. Chan, and S. John, "Photonic band gap architectures for holographic lithography," *Physical Review Letters*, vol. 92, p. 043905, 2004.
- [5] D. N. Sharp, A. J. Turberfield, and R. G. Denning, "Holographic photonic crystals with diamond symmetry," *Physical Review B*, vol. 68, p. 205102, 2003.
- [6] J. W. Rinne and P. Wiltzius, "Design of holographic structures using genetic algorithms," *Optics Express*, vol. 14, pp. 9909-9916, 2006.
- [7] S. A. Rinne, F. Garcia-Santamaria, and P. V. Braun, "Embedded cavities and waveguides in three-dimensional silicon photonic crystals," *Nature Photonics* vol. 2, pp. 52-56, 2008.

- [8] G. M. Gratson, F. Garcia-Santamaria, V. Lousse, M. J. Xu, S. H. Fan, J. A. Lewis, and P. V. Braun, "Direct-write assembly of three-dimensional photonic crystals: Conversion of polymer scaffolds to silicon hollow-woodpile structures," *Advanced Materials*, vol. 18, pp. 461-465, 2006.
- [9] F. Pérez-Willard, S. John, M. Wegener, and G. A. Ozin, "New Route to Three-Dimensional Photonic Bandgap Materials: Silicon Double Inversion of Polymer Templates\*," *Advanced Matererials*, vol. 18, pp. 457-460, 2006.
- [10] V. Ramanan, E. Nelson, A. Brzezinski, P. V. Braun, and P. Wiltzius, "Three dimensional silicon-air photonic crystals with controlled defects using interference lithography," *Applied Physics Letters*, vol. 92, p. 173304, 2008.
- [11] J. H. Moon, S. Yang, W. Dong, J. W. Perry, A. Adibi, and S. M. Yang, "Core-shell diamond-like silicon photonic crystals from 3D polymer templates created by holographic lithography," *Optics Express*, vol. 14, pp. 6297-6302, 2006.
- [12] F. García-Santamaría, M. Xu, V. Lousse, S. Fan, P. V. Braun, and J. A. Lewis, "A Germanium Inverse Woodpile Structure with a Large Photonic Band Gap," *Advanced Matererials*, vol. 19, pp. 1567-1570, 2007.
- [13] J. S. King, E. Graugnard, O. M. Roche, D. N. Sharp, J. Scrimgeour, R. G. Denning, A. J. Turberfield, and C. J. Summers, "Infiltration and inversion of holographically defined polymer photonic crystal templates by atomic layer deposition," *Advanced Materials*, vol. 18, pp. 1561-1565, 2006.
- [14] J. H. Moon, Y. G. Xu, Y. P. Dan, S. M. Yang, A. T. Johnson, and S. Yang, "Triply periodic bicontinuous structures as templates for photonic crystals: A pinch-off problem," *Advanced Materials*, vol. 19, pp. 1510-1514, 2007.
- [15] A. Brzezinski, Y. C. Chen, P. Wiltzius, and P. V. Braun, "Complex three-dimensional conformal surfaces formed by atomic layer deposition: Computation and experimental verification," *Journal of Materials Chemistry*, *accepted*.
- [16] D. Gaillot, T. Yamashita, and C. J. Summers, "Photonic band gaps in highly conformal inverse-opal based photonic crystals," *Physical Review B*, vol. 72, p. 205109, 2005.
- [17] M. Maldovan, C. K. Ullal, W. C. Carter, and E. L. Thomas, "Exploring for 3D photonic bandgap structures in the 11 fcc space groups," *Nature Materials*, vol. 2, pp. 664-667, 2003.
- [18] Y. C. Chen, J. B. Geddes Iii, J. T. Lee, P. V. Braun, and P. Wiltzius, "Holographically fabricated photonic crystals with large reflectance," *Applied Physics Letters*, vol. 91, p. 241103, 2007.
- [19] R. Courant, K. Friedrichs, H. Lewy, and A. California Univ Los, *On the Partial Difference Equations of Mathematical Physics*: New York University, Institute of Mathematical Sciences, 1956.

- [20] W. G. M. Geraets, A. N. van Daatselaar, and J. G. C. Verheij, "An efficient filling algorithm for counting regions," *Computer Methods and Programs in Biomedicine*, vol. 76, pp. 1-11, 2004.
- [21] M. Ritala and M. Leskelae, "Atomic layer epitaxy-a valuable tool for nanotechnology?," *Nanotechnology*, vol. 10, pp. 19-24, 1999.
- [22] M. Campbell, D. N. Sharp, M. T. Harrison, R. G. Denning, and A. J. Turberfield, "Fabrication of photonic crystals for the visible spectrum by holographic lithography," *Nature*, vol. 404, pp. 53-56, 2000.
- [23] D. Gerthsen, K. Busch, and M. Wegener, "Shrinkage Precompensation of Holographic Three-Dimensional Photonic-Crystal Templates," *Advanced Matererials*, vol. 18, pp. 2964-2968, 2006.
- [24] A. Farjadpour, D. Roundy, A. Rodriguez, M. Ibanescu, P. Bermel, J. D. Joannopoulos, S. G. Johnson, and G. W. Burr, "Improving accuracy by subpixel smoothing in the finite-difference time domain," *Optics Letters*, vol. 31, pp. 2972-2974, 2006.
- [25] Y. V. Miklyaev, D. C. Meisel, A. Blanco, G. von Freymann, K. Busch, W. Koch, C. Enkrich, M. Deubel, and M. Wegener, "Three-dimensional face-centered-cubic photonic crystal templates by laser holography: fabrication, optical characterization, and band-structure calculations," *Applied Physics Letters*, vol. 82, pp. 1284-1286, 2003.
- [26] M. Miyake, Y. C. Chen, P. V. Braun, and P. Wiltzius, "Fabrication of Three-Dimensional Photonic Crystals Using Multibeam Interference Lithography and Electrodeposition," *Advanced Materials*, vol. 21, pp. 3012-3015, 2009.
- [27] P. V. Braun and P. Wiltzius, "Microporous materials - Electrochemically grown photonic crystals," *Nature*, vol. 402, pp. 603-604, 1999.
- [28] Y. C. Lee, T. J. Kuo, C. J. Hsu, Y. W. Su, and C. C. Chen, "Fabrication of 3D macroporous structures of II-VI and III-V semiconductors using electrochemical deposition," *Langmuir*, vol. 18, pp. 9942-9946, 2002.
- [29] X. D. Yu, Y. J. Lee, R. Furstenberg, J. O. White, and P. V. Braun, "Filling fraction dependent properties of inverse opal metallic photonic crystals," *Advanced Materials*, vol. 19, pp. 1689-1692, 2007.
- [30] A. A. Zhukov, A. V. Goncharov, P. A. J. de Groot, M. A. Ghanem, P. N. Bartlett, R. Boardman, H. Fangohr, V. Novosad, and G. Karapetrov, "Oscillatory thickness dependence of the coercive field in magnetic three-dimensional antidot arrays," *Applied Physics Letters*, vol. 88, p. 062511, 2006.
- [31] Y. Xu, X. Zhu, Y. Dan, J. H. Moon, V. W. Chen, A. T. Johnson, J. W. Perry, and S. Yang, "Electrodeposition of three-dimensional titania photonic crystals from holographically patterned microporous polymer templates," *Chemistry of Materials*, vol. 20, pp. 1816-1823, 2008.



- [32] J. H. Jang, C. K. Ullal, M. Maldovan, T. Gorishnyy, S. Kooi, C. Y. Koh, and E. L. Thomas, "3D micro- and nanostructures via interference lithography," *Advanced Functional Materials*, vol. 17, pp. 3027-3041, 2007.
- [33] M. E. Abuzeid, A. E. Rakhshani, A. A. Aljassar, and Y. A. Youssef, "Determination of the thickness and refractive-index of Cu<sub>2</sub>O Thin-film using thermal and optical interferometry " *Physica Status Solidi a-Applied Research*, vol. 93, pp. 613-620, 1986.
- [34] T. D. Golden, M. G. Shumsky, Y. C. Zhou, R. A. VanderWerf, R. A. VanLeeuwen, and J. A. Switzer, "Electrochemical deposition of copper(I) oxide films," *Chemistry of Materials*, vol. 8, pp. 2499-2504, 1996.
- [35] A. E. Rakhshani and J. Varghese, "Optical-absorption coefficient and thickness measurement of electrodeposited films of Cu<sub>2</sub>O," *Physica Status Solidi a-Applied Research*, vol. 101, pp. 479-486, 1987.
- [36] S. Jeon, V. Malyarchuk, J. A. Rogers, and G. P. Wiederrecht, "Fabricating three dimensional nanostructures using two photon lithography in a single exposure step," *Optics Express*, vol. 14, pp. 2300-2308, 2006.
- [37] M. Deubel, G. Von Freymann, M. Wegener, S. Pereira, K. Busch, and C. M. Soukoulis, "Direct laser writing of three-dimensional photonic-crystal templates for telecommunications," *Nature Materials*, vol. 3, pp. 444-447, 2004.
- [38] S. G. Johnson and J. D. Joannopoulos, "Block-iterative frequency-domain methods for Maxwell's equations in a planewave basis," *Optics Express*, vol. 8, pp. 173-190, 2001.

## CHAPTER 6

### FABRICATION WITH CHEMICALLY AMPLIFIED POSITIVE PHOTORESIST

\* In collaboration with Jyh-Tsung Lee in the Department of Chemistry at National Sun Yat-Sen University, Kaohsiung, Taiwan.

#### 6.1 Introduction

The use of a positive resist system has been previously suggested and demonstrated for multibeam interference lithography [1-3]. Compared to negative resist, it has the advantage of easy template removal, no shrinkage from polymerization or crosslinking, and no swelling during the development process that could hamper resolution.

Swelling of the photoresist during development is a serious issue in holographic lithography. Due to the continuous variation of the intensity profile, photoresist response is not purely binary. When intensity contrast is only moderate, incomplete crosslinking may dominate the structure. In negative resists, while the developer is a good solvent for the monomer, it is also a good solvent for the incompletely crosslinked polymer so undesirable swelling occurs. This can cause delamination during development, oligomer leaching leading to volume loss, and distortion during drying. Positive resist patterning, however, operates by solubility change of the polymer. While the developer is a good solvent for the photo-switched region, it is a bad solvent for the non-switched region. This prevention of swelling eliminates the delamination and shrinkage problems that occur with typical SU-8 holographic patterning, and allows recording of interference patterns with high fidelity. Figure 6.1 illustrates the difference between the two photoresists during development.

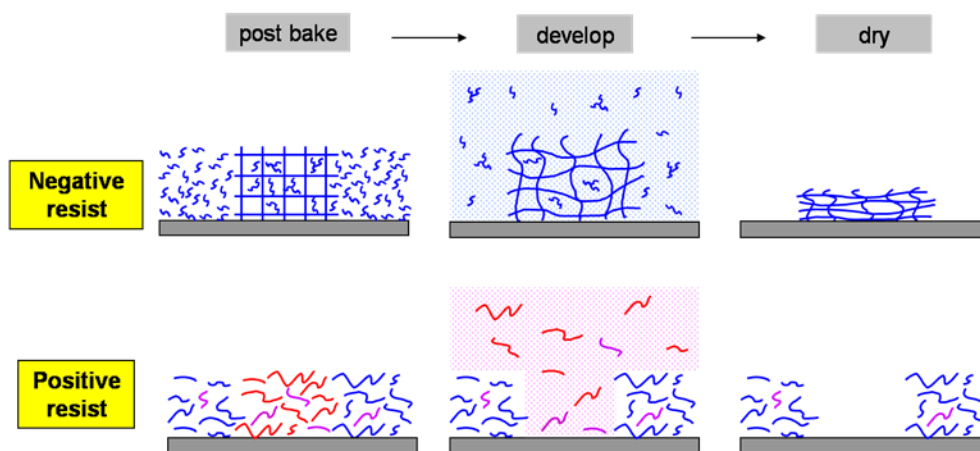


**Figure 6.1** Schematic of development process for negative resist and positive resist. For negative resist, the partially crosslinked polymers may be developed away when the structure is swelled by developer; for positive resist, the partially reacted will be trapped in the structure because the developer is a poor solvent for the un-switched polymer.

As discussed in Chapter 1, the chemically amplified positive photoresist system is more advantageous than the typical DNQ system for generating thick 3D patterns. Such a positive photoresist system has been reported for 3D fabrication using two-photon excitation with feature sizes of several microns [4, 5]. We modified the reported chemically amplified positive photoresist systems to achieve sub-micron photonic crystal fabrication with both single and two photon patterning.

## 6.2 Positive Photoresist Design

The bulk of the positive resist is a co-polymer with methyl methacrylate (MMA) and deprotecting group, tetrahydropyranyl methacrylate (THPMA) that will transform from hydrophobic to hydrophilic under acidic conditions (Figure 6.2(a)). As with SU-8, a photoacid generator is included for photopatterning. When exposed to light of appropriate wavelengths, the acid is generated and catalyzes the hydrophobic-hydrophilic switch reaction. The protecting group becomes methacrylic acid (MAA), and the polymer becomes soluble in aqueous base solutions (Figure 6.2(b)).

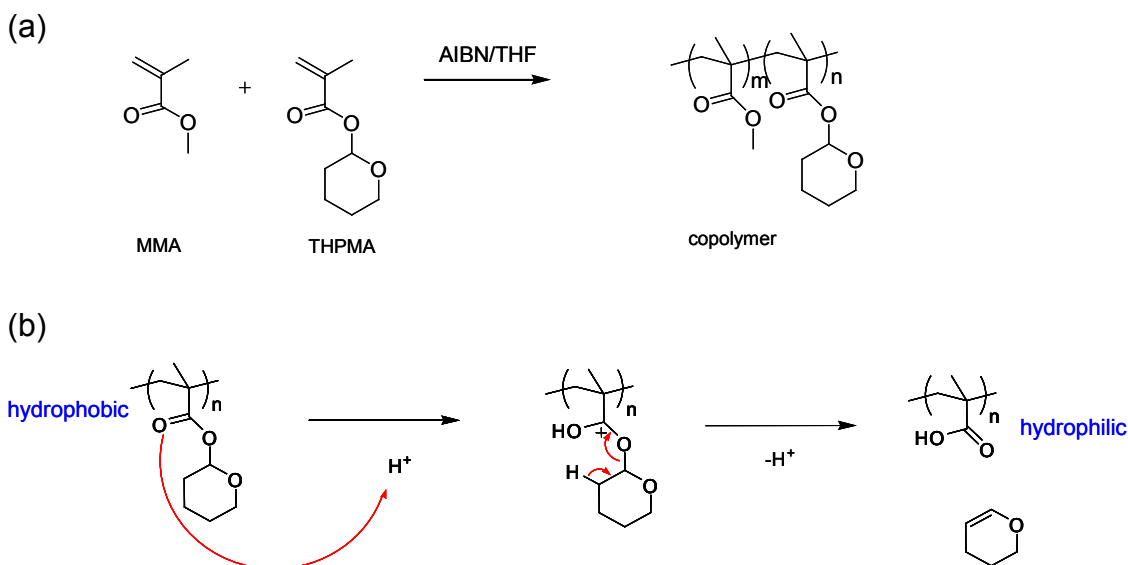


**Figure 6.2** Chemically amplified positive photoresist design. (a) Copolymer composition (b) Hydrophobic-hydrophilic switch mechanism of de-protecting group THPMA.

In order to form a photoresist for 3D nano-scale patterning, the following factors must be considered for the copolymer. As in the negative photoresist system, the polymer should be able to form a flat thick film by spin coating, so it needs to be soluble in a proper solvent. The polymer should have low absorption at the patterning wavelength, so exposure dose is not attenuated through the thickness of the film. It should also be compatible with the photo acid generator used for patterning – they need to dissolve into each other well and not cause scattering.

An additional concern for 3D patterning with the chemically amplified positive resist is that the protecting group residual should not be significantly volatile below the de-protecting temperature, to avoid deformation from by-product boiling. This is not an issue with 2D patterning because there is a direct pathway for the vapor to escape. For 3D patterning, however, foaming phenomena have been observed which cause deformation of the patterns. For example, a commonly used de-protecting group, tert-butyl methacrylate (tBOC) would not be suitable because the de-protection temperature is around 130-150°C and its acid catalyzed reaction by-product, isobutylene, is vapor at room temperature. Figure 6.3 shows a foamy patterning result from a MMA-tBOC co-polymer. On the other hand, the de-protection of THPMA occurs around

70-90°C, and the by-product, 3,4-dihydro-2H-pyran, has a boiling temperature of 86°C. So with proper postbaking temperature controls it is possible to keep the by-product in the resist or evaporating very slowly without distorting the 3D pattern [5].

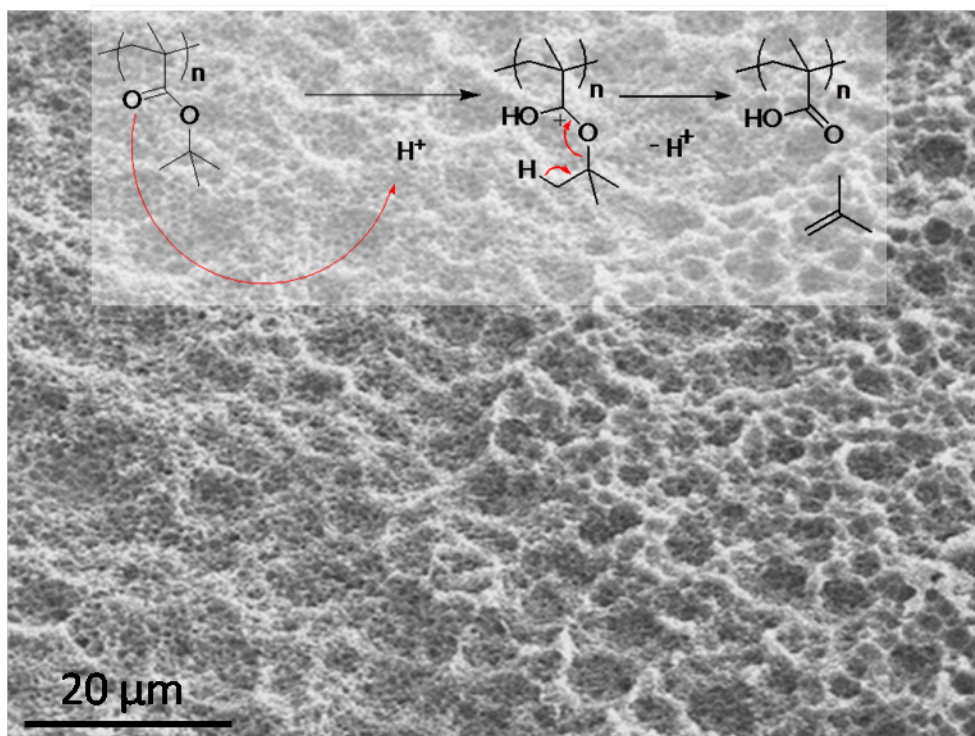


**Figure 6.3** SEM of a porous film resulting from de-protecting by-product of MMA-tBOC co-polymer.

In the THPMA-MMA co-polymer, MMA provides mechanical strength and hydrophilicity for development while THPMA provides the polarity switching. We also explored adding isobornyl methacrylate (IBMA), a commercially available monomer, shown in Figure 6.4, to increase the stiffness of the film. However IBMA is very hydrophobic and too much of it prevents the co-polymer from dissolving in aqueous developer even when all of the THPMA has switched. The patterning potential of the polymer can be tested in a simple manner: a small amount of polymer is immersed in diluted sulfuric acid aqueous solution (de-protection), and add in sodium hydroxide until the solution turns basic (development). If the polymer dissolves, then

it can be patterned. If not, then the polymer cannot be used for our purposes. In our tests, we found that we can dissolve MMA(70%)-THPMA(30%) and IBMA(10%)-MMA(60%)-THPMA(30%), but not IBMA(30%)-MMA(40%)-THPMA(30%).

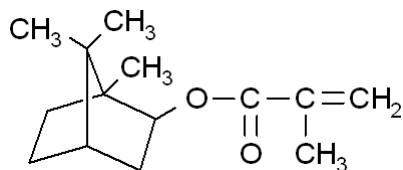


**Figure 6.4** Isobornyl methacrylate (IBMA),

### 6.3 3D Patterning

To pattern the polymer optically, an efficient and soluble photoacid generating system needed to be found for the patterning wavelength. Photoresists modified with various PAG were tested by one beam interference. Unfortunately all the initiator systems for 532 nm were unsuccessful. The exposed spots did not undergo the hydrophobic-hydrophilic switch even with prolonged exposures and high temperature postbaking steps with a reasonable initiator concentration (~5%). However, we found that triarylsulfonium/ hexafluoroantimonate salt, the PAG in commercialized SU-8, can effectively activate the de-protonation reaction at the 351 nm wavelength (I-90 Ar-Ion laser, Coherent Inc.). A combination of Isopropyl thioxanthone (ITX) sensitizer and Uvacure1600 PAG also works well. The patterning procedure consists of all the same steps as SU-8 patterning: spin coating the film, prebaking to remove solvent, exposure, postbake, development and drying.

#### 6.3.1 Multibeam Interference Lithography

The optimum co-polymer in reference [5] was first tested with four-beam interference lithography at 351 nm. The four beams were arranged in an umbrella geometry but with the polarization projected the same direction, as in Figure 2.18(a). The photoresist consists of 5 wt%

triarylsulfonium/ hexafluoroantimonate salt in MMA : THPMA = 60:40 with copolymer and cyclopentanone as solvent for spin coating. Patterning was first tested with a relatively thin film. A very promising patterning result was obtained as shown in Figure 6.5. The submicron periodicity is clearly visible in this sample. The superior sensitivity of the resist even recorded the standing wave caused by interference between the incident and reflected light from the substrates and air, as highlighted in Figure 6.5(c). The fringes here are measured to be 114 nm. From this we can calculate the refractive index of the polymer 1.54 at 351 nm, which corresponds to the expected value.

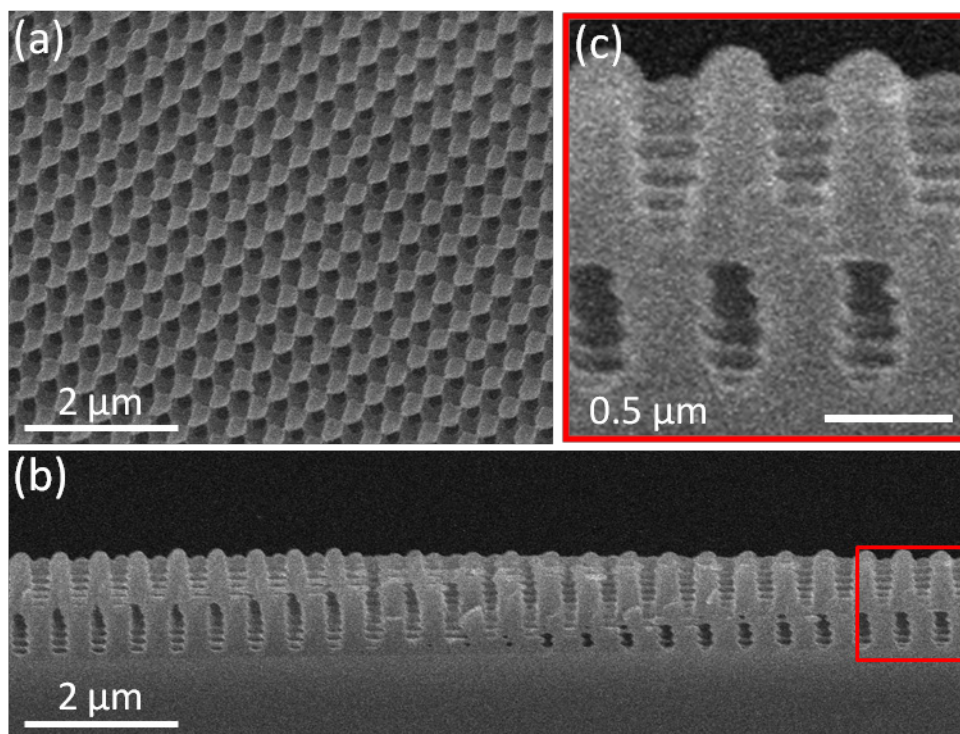


**Figure 6.5** SEM of patterning result of co-polymer (MMA:THPMA=60:40). (a) Top surface view at an angle (b) Cross-sectional image (c) Zoomed-in section showing the recorded standing wave

We next attempted to pattern a thicker film with the same polymer. However we observed significant structural collapse probably due to insufficient mechanical strength. To counter this we increased the MMA fraction, making the co-polymer ratio MMA:THPMA =

70:30. Significant improvement was observed allowing thick films to be patterned, as seen in Figure 6.6(a)&(b). The thickness of the patterned film is the same as the unpatterned regions, indicating there is no shrinkage during the fabrication process. To further confirm this, the layer spacing was calculated and compared to SEM measurements (558nm). Judging by the SEM picture, the in-plane periodicity  $a$  is 522 nm which would indicate that the central – side beam angle is  $30.28^\circ$  inside the photoresist, with refractive index of the film being 1.54. The calculated vertical layer spacing of 557 nm, agreeing with the SEM measurement. This also confirms the refractive index value 1.54 obtained with the standing wave spacing estimation is accurate.

Although a large region of a crystal can be resolved with a 70/30 molar ratio of MMA/THPMA, the structure still has significant collapsed areas, resulting in poor optical quality. The deformation of the film can be observed during the development step, before drying. To verify that this collapse is due to poor mechanical properties of the film, phase mask lithography was performed using the 351 nm laser. The resulting 3D structures also show collapsed regions. We further increased the molar ratio to 80/20, but during development the patterned regions were not soluble enough to dissolve in developer but would only swell instead. Addition of the isobornyl methacrylate (IBMA) was also tested for improving the mechanical strength, but there was no significant improvement from that either. For reasons that were unclear, the results of our 70/30 MMA/THPMA tests could not be reproduced. Several factors, including exposure, baking and development conditions, were tuned, but no significant improvements were observed. Nor were any trends observed when testing each factor. In order to better understand the underlying problem, we attempted two-photon phase mask lithography to fabricate micron-sized patterns.



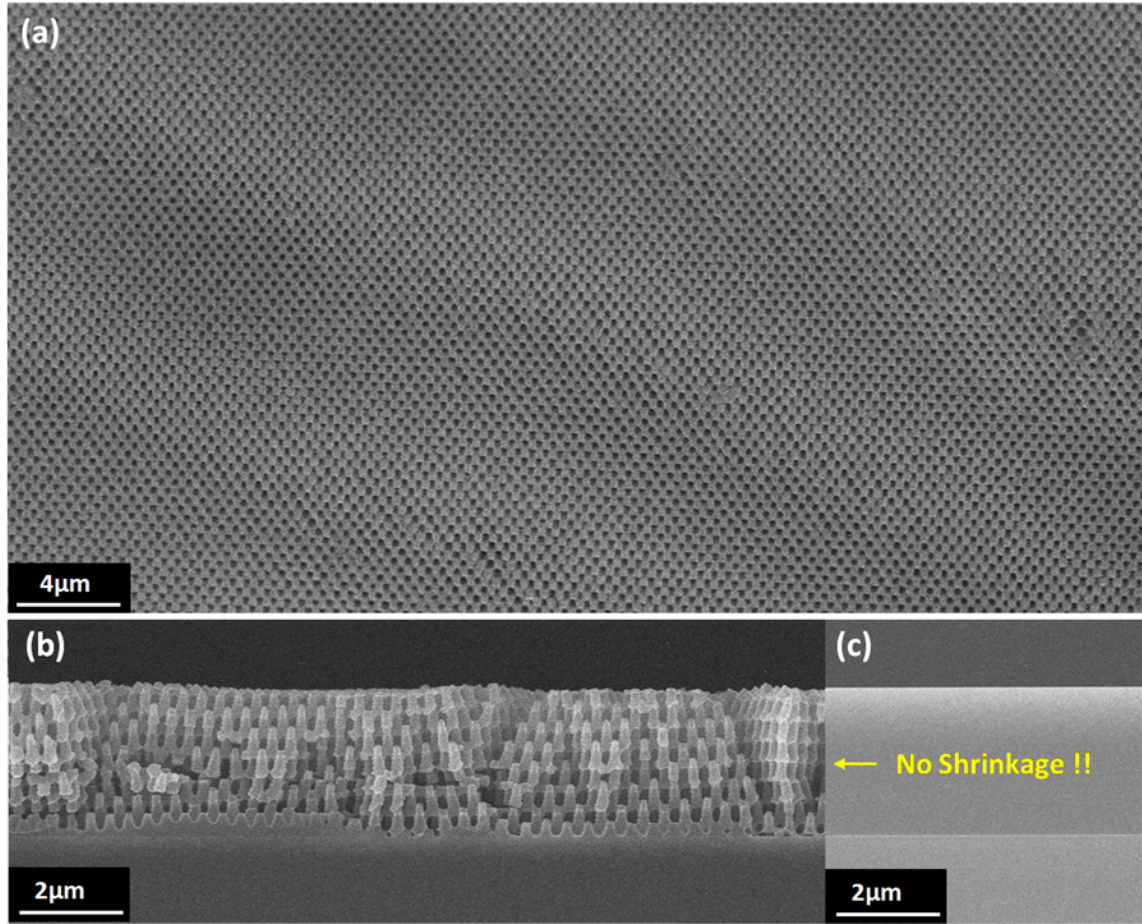


**Figure 6.6** SEM micrographs of positive resist (a) top view, tilted at an angle  $\sim 45^\circ$  (b) cross-sectional view (c) un-patterned region show same thickness as patterned region, indicating no shrinkage

### 6.3.2 Phase Mask lithography

Our two photon phase mask lithography system follows the setup reported in reference [6] with a Ti-Sapphire pulse laser tuned at 800nm. ITX and PAG were added to the photoresist as the two-photon photoinitiator. Solvent assisted molding was an option with both acetone and ethanol; However, most tests were done without an imprinting step. At first the result was non-uniform and unpredictable, but it was soon observed that in most cases if there was an “explosion” site present, the structure at the site would usually look good. Later it became clear that an overlayer was present on the structure. Once the developer had passed the overlayer, well-formed structures could be obtained. This skin effect is caused by base contamination from atmosphere,

as described in chapter 1.2. This is the reason that no visible trends were observed when testing the parameter space in previous experiments, because the skin layer prevented proper development.

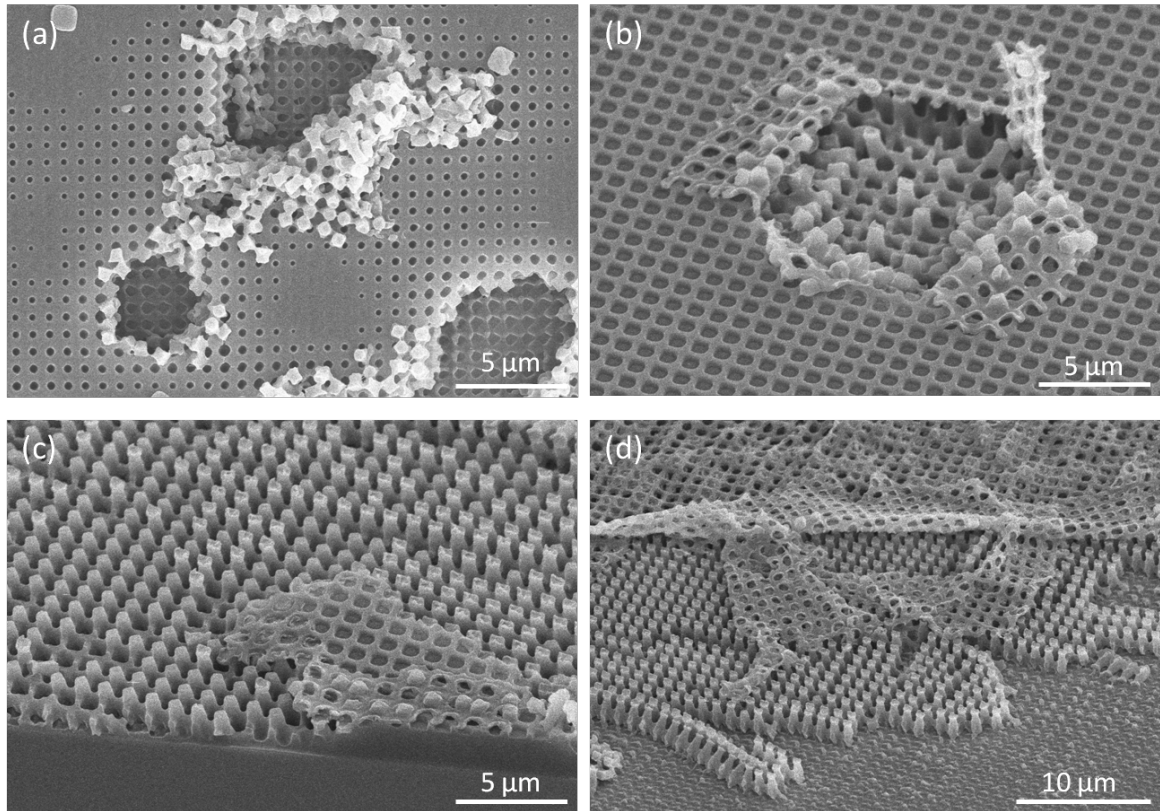


**Figure 6.6** Effect of base contamination on the patterning of chemically amplified positive photoresist. (a) Where the developer can get through is over-developed, while the rest is under developed. (b) Showing the skin is broke off and the structure under can be developed. (c) Regions that still has the skin cannot develop through (d) Good structures showing under the skin

After identifying the main issue of the over layer caused by base contamination, efforts were made to resolve it. Unlike an industry environment where air is often flowed through activated carbon filters (Figure 1.2.16), in the lab we needed to find alternative method to prevent contamination. First, the time between exposure and post bake was minimized to shorten the potential photoacid neutralization time. Although this did make the skin thinner, the problem still remained. This was because neutralization happens once the exposure starts (when the photoacid

is generated), and the required exposure dose takes several minutes. This method would have more potential for the single photon system, with exposure times of several seconds. If a more efficient two-photon initiation system is used, like those reported in ref [4], exposure time (also contamination time) can be reduced.

Other attempts include coating the resist with a layer of water soluble polymer before exposure to protect the resist from contacting atmosphere. Polyacrylic acid has been tested for this method. Despite the fact that a solution of 50wt% PAA in water spin coats well on the unpatterned positive photoresist, this method did not work because the PAA and the resist are slightly miscible, resulting in an uneven surface causing a local lens refraction effect smearing of the diffraction patterns. Another attempt to apply acid on to the surface of the film, using diluted acetic acid vapor, involved spin coating the acid and stamping an acid-treated flat PDMS stamp to the resist before post baking. Both vapor and spin coating treatments were not suitable because they tend to affect the entire film thickness. This was the case even when using the less volatile propionic acid. PDMS stamping seemed the most promising. An improvement in development can be clearly seen as the untreated spot takes several seconds to show iridescence from the periodic pattern, while the acid stamped ones can be seen immediately. However the result is also inconsistent due to the varying level of contamination.

A consistent solution was found by using reactive ion etching (RIE) to remove the top layer of polymer followed by immediate development. The RIE condition is carefully tuned so that the film remains smooth. Because the contaminated layer is removed, the development is much more uniform throughout the film as confirmed by cross-sectional imaging of fractured surface. Different phase mask periodicities were used to fabricate patterns, as shown in Figure 6.7. All of the films have large 3D structures with regions extending to the substrate. This indicates that upon removal of contaminated skin the developer is no longer restricted or blocked from penetrating through the film. The result shows excellent patterning capability for 1.6 micron



horizontal periodicity, but as the periodicity decreases the mechanical strength becomes poorer, even though the resist is sensitive enough to resolve fine details.

Large uniform areas with periodic patterns make consistent optical characterization possible. Figure 6.8 shows an optical reflection spectrum from a sample with 1  $\mu\text{m}$  horizontal spacing from normal incidence. The polymer's refractive index is 1.52 at 800nm, as measured by ellipsometry, and the vertical periodicity is calculated to be 3.5  $\mu\text{m}$  (double of layer spacing). The reflectance peak shown at  $\sim 2.3 \mu\text{m}$  is expected to be one of the high energy peaks of the structure.

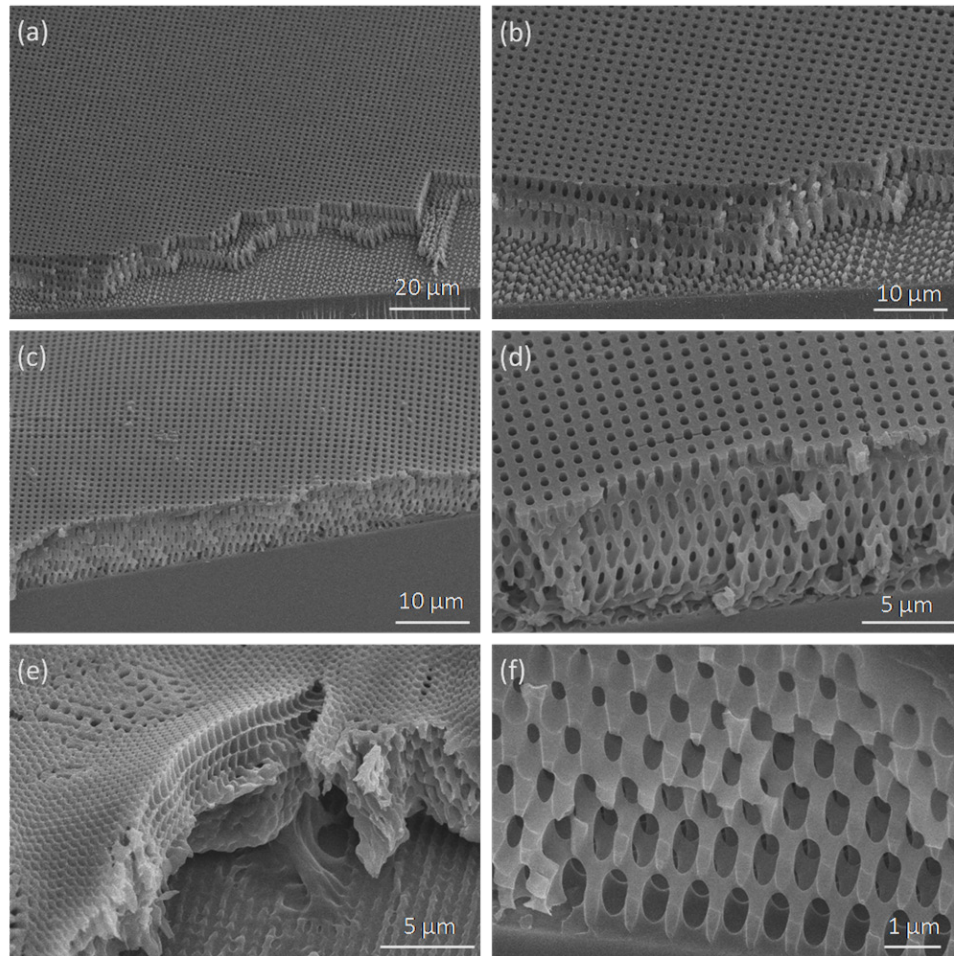


**Figure 6.7** Positive resist patterning result with RIE with different phase mask dimension periodicities (a)&(b) 1.6  $\mu\text{m}$ , (c)&(d) 1  $\mu\text{m}$ , (e)&(f) 0.76  $\mu\text{m}$ .

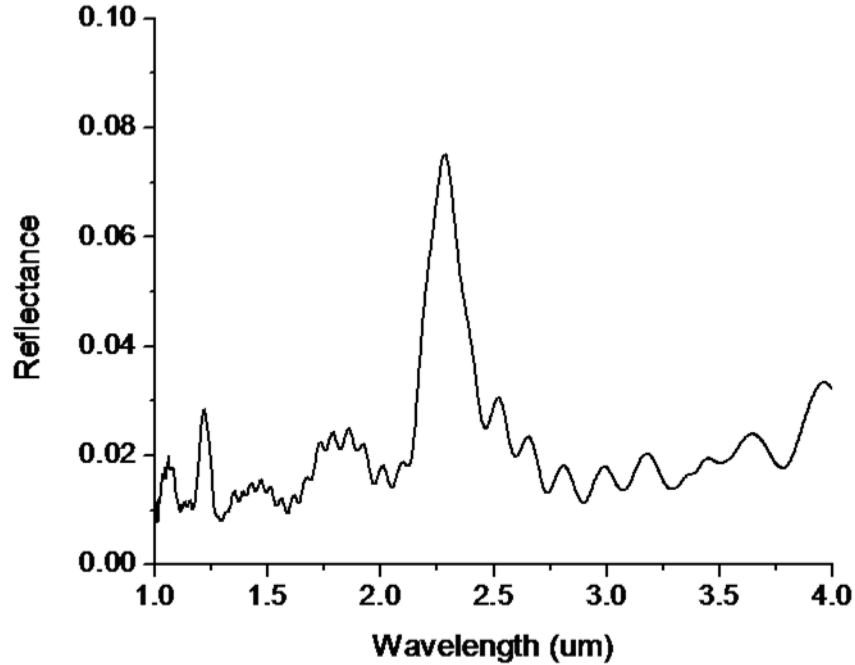


**Figure 6.8** Reflectance spectrum of the fabricated crystal with 1  $\mu\text{m}$  horizontal periodicity.

#### 6.4 Conclusions and Future Directions

We have fabricated sub-micron periodic 3D structures using a customized chemically amplified positive photoresist by both single-photon and two-photon patterning. The resist has high sensitivity and the resulting pattern experiences no shrinkage. Although the over-layer problem prevented the resist from functioning reliably, it was resolved by reducing post exposure delay and reactive ion etching. Mechanical strength was less than desired for submicron structures. However it can be improved by adjusting the co-polymer composition and fine tuning processing factors.

There is great potential for positive photoresist to improve the field of photonic crystal fabrication by multibeam interference lithography. The resulting structures display high fidelity to the target, which means the theoretically proposed photonic band gap geometry for multi-beam interference lithography may be fabricated without distortion. For photonic band gap applications, high refractive index material can be infiltrated directly into the crystal with electrodeposition. The shrinkage-resistant and high resolution properties of the resist template

coupled with complete infiltration by electrodeposition can achieve highly optimized and designed photonic band gap structures. For materials that require high temperature processing, a double-inversion technique can be used by first inverting the crystal to alumina or silica. As a template, the positive photoresist is easily removed by organic solvent. Thus, materials that are not compatible with processes required to remove SU-8 and other crosslinked polymer such as high-temperature pyrolysis, strong acid oxidation or reactive ion etching, may be inverted directly from the positive resist template. Furthermore, surface modification may be possible by functionalizing the exposed MAA groups of the crystal for designated surface properties [5].

In addition, using the positive photoresist system, we were able to adapt and employ previous work on SU-8 [7]. This includes holographically generating periodic patterns and adding multi-photon writing to generate aperiodic features, all within one photoresist film. In addition to the holographic crystal fabrication steps, only one TPP writing step is needed before post baking, which is a much simplified process over introducing a second photoresist for feature patterning [8]. A large holographic photonic crystal with the designed geometry and the ability to incorporate random defects would provide an platform for the study of a wide variety of photonic phenomena.

## 6.5 Experimental

### 6.5.1 Synthesis of tetrahydropyranyl methacrylate (THPMA)

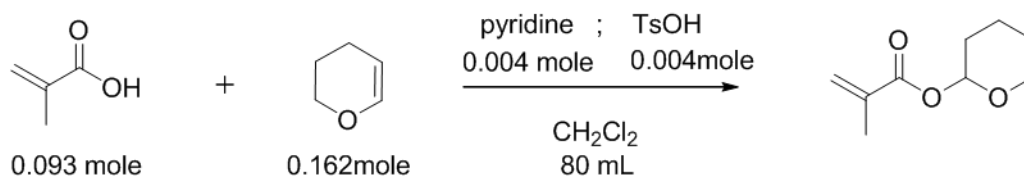


**Figure 6.9** Chemical reaction of THPMA synthesis.

Toluenesulfonic acid (0.004 mole, 0.71 g), pyridine (0.004 mole, 0.32 ml) and methacrylic acid (MAA, 0.093 mole, 8.00 g) were mixed into dichloromethane (80 ml) in sequence followed by slowly adding in 3,4-dihydro-2H-pyran (0.162 mole). The solution was mixed under nitrogen at room temperature for 24 hours. The salt from the mixture was extracted using silica gel column. Excess MAA was extracted out by adding H<sub>2</sub>O as extracting solution to the solution with a 1:1 ratio and extract using a separatory funnel. Excess water was extracted from the solution with brine purification process. Magnesium sulfate anhydrous was added into the solution and stir for 30 minutes in order to further de-hydrate the solution. The mixture was filtered with filter paper, and the filtered solution was vacuumed to take away solvent (dichloromethane). The weight of the solution is monitored, and vacuum process is complete when weight change rate became slow.

#### 6.5.2 Synthesis of copolymer poly(tetrahydropyranyl methacrylate)

Methyl methacrylate (MMA , 10.00 g) and THPMA(8.82 g) were mixed in THF (200 ml). The solution went through three times of freeze-pump-thaw degas process (10 min each). It was added in a readily degassed container with AIBN (0.0941g) and refluxed at 70 °C for 20 hours. After concentration, the polymer is extracted from the solution in methanol and dried by vacuum overnight.

#### 6.5.3 Positive Photoresist Formulation

Function	Ingredient	Weight Ratio	Molar ratio
Sensitizer	ITX	0.027	9
photoacid generator (PAG)	Uvacure1600	0.0447	6
Copolymer	Poly-MMA-THPMA	0.7248	--
Thresholding agent	2,6-di-tert-butylpyridine	0.002346	1
Solvent	Cyclopentanone	1.5*	--

Cover glass was cleaned with soap, water, acetone, isopropanol and dried by nitrogen. The substrate was immersed in 50% chlorotrimethylsilane in acetone for 1 minute in order to obtain a

hydrophobic surface for adhesion purpose. The photoresist was spin-coated onto the substrate at 500rpm for 2 minutes, and the substrate was baked in an oven at 50 °C for one hour.

#### 6.5.4 Two-photon Phase Mask Lithography

Circularly polarized light source was generated from a regeneratively amplified Ti:sapphire laser (Spectra-Physics, Spitfire-Pro) operating at a wavelength of 800nm with average power ~2W, repetition rate 1 kHz and the pulse width ~160 fs with beam diameter ~5mm. The photoresist film was brought to conformal contact with the PDMS phase mask [6] and exposed to the laser beam through the phase mask for 4 minutes. The film was immediately post-baked on a hotplate at 60°C for 3 minutes. Reactive ion etching (RIE) was then performed with 20 sccm O<sub>2</sub> and 2 sccm CF<sub>4</sub> at 150 W for 30 sec. The film was immersed in developer AF 300MIF (2.38 wt% tetramethylammonium hydroxide in H<sub>2</sub>O) for 1 min, rinsed with DI water and immersing in perfluorohaptane finally dried gently with nitrogen.

## 6.6 References

- [1] J. H. Jang, C. K. Ullal, T. Gorishnyy, V. V. Tsukruk, and E. L. Thomas, "Mechanically tunable three-dimensional elastomeric network/air structures via interference lithography," *Nano Letters*, vol. 6, pp. 740-743, 2006.
- [2] J. H. Jang, C. K. Ullal, M. Maldovan, T. Gorishnyy, S. Kooi, C. Y. Koh, and E. L. Thomas, "3D micro- and nanostructures via interference lithography," *Advanced Functional Materials*, vol. 17, pp. 3027-3041, 2007.
- [3] J. H. Moon, J. Ford, and S. Yang, "Fabricating three-dimensional polymeric photonic structures by multi-beam interference lithography," *Polymers for Advanced Technologies*, vol. 17, pp. 83-93, 2006.
- [4] W. H. Zhou, S. M. Kuebler, K. L. Braun, T. Y. Yu, J. K. Cammack, C. K. Ober, J. W. Perry, and S. R. Marder, "An efficient two-photon-generated photoacid applied to positive-tone 3D microfabrication," *Science*, vol. 296, pp. 1106-1109, 2002.
- [5] T. Y. Yu, C. K. Ober, S. M. Kuebler, W. H. Zhou, S. R. Marder, and J. W. Perry, "Chemically amplified positive resists for two-photon three-dimensional microfabrication," *Advanced Materials*, vol. 15, pp. 517-521, 2003.



- [6] S. Jeon, V. Malyarchuk, J. A. Rogers, and G. P. Wiederrecht, "Fabricating three dimensional nanostructures using two photon lithography in a single exposure step," *Optics Express*, vol. 14, pp. 2300-2308, 2006.
- [7] S. A. Pruzinsky, "Two-photon Polymerization of Defects in Photonic Crystals," in *Materials Science and Engineering*. vol. PhD: University of Illinois at Urbana Champaign, 2006, p. Chapter 5.
- [8] V. Ramanan, E. Nelson, A. Brzezinski, P. V. Braun, and P. Wiltzius, "Three dimensional silicon-air photonic crystals with controlled defects using interference lithography," *Applied Physics Letters*, vol. 92, p. 173304, 2008.

## CHAPTER 7

### CONCLUSIONS

Multibeam interference lithography has been projected as a promising candidate for large scale three dimensional photonic crystal template fabrications. In this work we investigate several aspects of the technique including fabrication, optical characterization, 3D imaging, template infiltration and high fidelity recording media.

Optimization of the photoresist initiation system and optical setup led to a significant improvement of the optical quality of the crystal, as characterized by normal incidence optical spectroscopy. Using the optical spectra and SEM measurements, a 3D model of the crystal was constructed and used to calculate theoretical spectra with both FDTD and 1D transfer matrix methods. The experimental spectra showed close agreement with these calculated spectra, indicating that excellent optical quality was achieved.

X-ray microscopy with computed tomography provided nano-scale resolution real-space imaging for our fabricated crystal. Both phase contrast and absorption contrast imaging were performed. The absorption contrast sample was coated with  $\text{HfO}_2$  to provide contrast enhancement for quantitative analysis. The geometry of the polymer template was reconstructed from the CT data and compared to the geometry obtained by assuming a uniform shrinkage model. The predicted structure had good agreement, with only 10% pixel mismatch from the CT reconstruction. This method allows us to understand processing shrinkage behavior, which provides a great tool to address the practical issues involved in the fabrication process. The modeling result shows potential incorporation into the structural design for optimized photonic crystal structures.

SU-8 3D photonic crystal templates were completely infiltrated with  $\text{Cu}_2\text{O}$  ( $n=2.6$ ) by electrodeposition. After etching away the SU-8, the crystal showed the exact inverse of the template and exhibited a high peak reflectance at the predicted wavelength. However, the

common CVD/ALD deposition process for high index materials such as silicon did not provide complete infiltration. A conformal algorithm was developed and carefully verified by experiment using a holographically fabricated SU-8 crystal and atomic layer deposition. This provides further insight into designing infilled optical structures, since the result is unique for each starting surface.

Chemically amplified positive photoresist was developed for no-shrinkage, high fidelity and easy-to-remove photonic crystal template fabrication. The photoacid generation causes a de-protecting reaction and enables development in aqueous base solution. Successful patterning was achieved with both single -photon and two-photon exposure systems. Minimizing or removing surface contamination was found to be crucial for obtaining a three dimensional structure. The preliminary result showed high resolution and no shrinkage. Further optimization of the copolymer composition is needed for better mechanical properties for 3D structures. The resist has great potential for generating structures matching the current theoretical design, as well as enabling direct combination of feature writing with two-photon excitation and broadening the types of materials that can be used for direct inversion.

Although this dissertation focuses on multibeam interference lithography, many aspects of the research are shared with phase mask lithography. Both techniques have great potential for defect-free, large scale photonic crystals. As the fabrication and characterization processes advance and with matured optical lithography techniques developed in industry, perhaps one day wide spread application of 3D photonic crystals will become a reality.

## **AUTHOR'S BIOGRAPHY**

Ying-Chieh (Christy) Chen [REDACTED]. She grew up in Hsinchu, Taiwan, attending National Experimental High School at Hsinchu Science Park from kindergarten through high school. Christy graduated from National Tsing Hua University, Hsinchu in 2002 with a B.S. in Materials Science and Engineering. During college, she spent her junior year at the University of Sheffield, UK. as an exchange student. She came to University of Illinois at Urbana Champaign to study for her Ph.D. in Materials Science and Engineering, under the supervision of Prof. Pierre Wiltzius and Prof. Paul Braun for her research in fabrication and characterization of 3D photonic crystals. Christy now resides in Hillsboro, Oregon with her husband.